DISS. ETH No. 13916

Super-Resolution Fluorescence Microscopy by Structured Light Illumination

Dissertation submitted to the
SWISS FEDERAL INSTITUTE OF TECHNOLOGY
ZURICH

for the degree of
Doctor of Technical Sciences

presented by
Jan Tillman Frohn
Dipl. Phys.
born February 28, 1971
citizen of Germany

accepted on recommendation of
Prof. Dr. A. Stemmer, examiner
Prof. Dr. H. J. Tiziani, co-examiner

Zurich, 2000

Acknowledgments

The research work presented in this thesis has been carried out in the period from fall 1997 to fall 2000 in the Nanotechnology Group at the Institute of Robotics. It was embedded in the poly project NANO-II at the "Eidgenössische Technische Hochschule Zürich".

Firstly, I wish to thank my advisor Prof. Dr. Andreas Stemmer who introduced me to the idea of increasing the resolution of light microscopy by structured light illumination. The inspiring atmosphere of his young and dynamic group was essential for the success of my work.

Furthermore, I am very grateful to Prof. Dr. H. J. Tiziani for taking the role of co-advisor of my thesis and for enlightening discussions.

Special thanks are due to Jakob Zbaeren who showed me an esthetic aspect of fluorescence microscopy which goes beyond the pure scientific one.

I very much appreciate the support of Helmut Knapp who gave me thousands of useful hints and tips.

Last but not least, I want to thank my likeable colleagues in the Nanotechnology Group for sharing joys and struggles with me.

Contents

Abstract

Optical far-field microscopes are essential tools for investigations in many disciplines in science and engineering. They combine convenient sample preparation with high imaging speed. Furthermore, the underlying physics of image formation in light microscopes are deeply understood. Therefore, image interpretation is much more evident than particularly in scanning probe techniques. Fluorescence microscopy additionally takes advantage of very specifically staining individual components of the object. Today, fluorescence microscopy has a large number of applications in biology and medicine.

Unfortunately, the resolution of optical far-field instruments is limited by the well known Rayleigh criterion. It predicts that two points cannot be distinguished if their lateral distance falls below approximately 240 nm in case of green light and oil-immersion objectives. During the last decade, various efforts have been undertaken to enhance the resolution of optical microscopes. The most common advancement in light microscopy is the confocal scanning microscope. By scanning a diffraction limited light spot through the specimen, the confocal microscope increases the lateral resolution by a factor of 1.5 under ideal conditions and, in addition, drastically enhances the optical sectioning capability.

In this thesis, a method called harmonic excitation light microscopy (HELM) is described which allows one to more than double the lateral resolution in fluorescence microscopy by illuminating the spec-

imen with a mesh-like interference pattern and electronic postprocessing of the images. The employed interference pattern covers the full field of view and can be shifted in two dimensions relative to the specimen by piezo actuators. Five images for different positions of the pattern are recorded by a camera. From these five images, additional information not accessible in conventional fluorescence microscopy can be extracted by an algebraic approach.

A setup producing harmonic excitation patterns in the object plane of a microscope by interference of laser beams has been realized. Images of artificial as well as biological samples show that HELM achieves a true optical resolution of approx. 100 nm. Therefore, HELM even outperforms the lateral resolving power of CFM by a factor of more than 1.5 and, additionally, avoids disadvantages of scanning methods.

A further part of the thesis deals with a three-dimensional extension of HELM. Basically, three-dimensional imaging is possible by stepping the focus through the object and acquiring a stack of two-dimensional images. However, the axial resolving power of conventional as well as confocal microscopes is far below the lateral one. By numeric simulations, a three-dimensional HELM device is shown to achieve an unrivaled resolution of approx. 100 nm laterally as well as axially. Since the system requirements for three-dimensional HELM are similar to those of confocal devices, it is expected that such systems could become a superior alternative to confocal ones, even from a commercial point of view.

Kurzfassung

Optische Fernfeldmikroskope sind unerlässliche Werkzeuge für Untersuchungen in vielen Gebieten von Forschung und Technik. Sie kombinieren einfache Probenpräparation mit hoher Abbildungsgeschwindigkeit. Außerdem sind die physikalischen Grundlagen der Bildentstehung in Fernfeldmikroskopen gut verstanden. Das macht die Bildinterpretation wesentlich einfacher als beispielsweise bei Rastersondenverfahren. Darüberhinaus ermöglicht die Fluoreszenzmikroskopie, einzelne Komponenten der Probe mit hoher Spezifität anzufärben. Auf Grund dieser Eigenschaft besitzt sie ein breites Anwendungsspektrum in Biologie und Medizin.

Leider ist das Auflösungsvermögen von optischen Fernfeldmikroskopen durch das bekannte Rayleighkriterium begrenzt. Es besagt, daß im Fall von grünem Licht und Ölimmersionsobjektiven zwei Punkte nicht unterschieden werden können, wenn ihr seitlicher Abstand kleiner als ungefähr 240 nm wird. Während des letzten Jahrzehnts sind viele Anstrengungen unternommen worden, um das Auflösungsvermögen von optischen Mikroskopen zu erhöhen. Die bekannteste Weiterentwicklung ist das konfokale Mikroskop. Indem beim konfokalen Mikroskop die Probe mit einem beugungsbegrenzt kleinen Lichtfleck abgerastert wird, kann einerseits die seitliche Auflösung um einen Faktor von maximal 1.5 erhöht und andererseits die Tiefenauflösung drastisch verbessert werden.

In dieser Arbeit wird eine Methode, genannt “harmonic excita-

tion light microscopy" (HELM), beschrieben, die es ermöglicht, die seitliche Auflösung von Fluoreszenzmikroskopen mehr als zu verdoppeln, indem die Probe mit einem gitterartigen Interferenzmuster beleuchtet wird und die aufgenommenen Bilder anschließend digital weiterverarbeitet werden. Das Interferenzmuster deckt das volle Gesichtsfeld ab und kann mittels Piezostellgliedern relativ zur Probe zweidimensional verschoben werden. Fünf Bilder für verschiedene Stellungen des Musters werden mit einer CCD-Kamera aufgenommen. Aus diesen Bildern können zusätzliche Objektinformationen, welche mit normaler Fluoreszenzmikroskopie nicht zugänglich wären, mit einem algebraischen Ansatz rekonstruiert werden.

Im Rahmen dieser Arbeit wurde ein System aufgebaut, welches ortsharmonische Beleuchtungsmuster mittels Interferenz von Laserstrahlen erzeugt. Bilder von sowohl künstlichen als auch biologischen Proben beweisen, daß HELM eine optische Auflösung von ungefähr 100 nm erreicht. Folglich übertrifft HELM das seitliche Auflösungsvermögen des konfokalen Mikroskops immer noch um einen Faktor von mehr als 1.5 und vermeidet außerdem die Nachteile von rasternden Verfahren.

Ein weiterer Teil der Arbeit beschäftigt sich mit einer dreidimensionalen Erweiterung von HELM. Grundsätzlich ist dreidimensionale Mikroskopie möglich, indem man einen Stapel von zweidimensionalen Bildern aufnimmt, während man den Fokus axial durch die Probe wandern lässt. Allerdings bleibt die axiale Auflösung sowohl des konventionellen als auch des konfokalen Mikroskops deutlich hinter der seitlichen Auflösung zurück. Numerische Simulationen zeigen, daß das Auflösungsvermögen eines dreidimensionalen HELM-Aufbaus sowohl seitlich als auch axial ungefähr 100 nm beträgt. Da die Systemanforderungen für ein solches Gerät denjenigen für konfokale Mikroskope ähneln, wird erwartet, daß ein dreidimensionales HELM-System eine überlegene Alternative zum konfokalen Mikroskop sein könnte, auch unter kommerziellen Gesichtspunkten.

Definition of terms

Mathematical conventions

A boldface variable $\mathbf{r}$ denotes a n-dimensional vector $(r_1, \ldots, r_n)$. The scalar product of two vectors is defined by

$$\mathbf{rs} = \sum_{i=1}^{n} r_i s_i. \tag{1}$$

The modulus of a (generally complex) vector is denoted by vertical strokes and is given by

$$|\mathbf{v}| = \sqrt{\sum_{i=1}^{n} v_i v_i^*}, \tag{2}$$

where the asterix denotes the complex conjugate.

The n-dimensional Fourier transform of a function $f : \mathbb{R}^n \to \mathbb{C}$ is denoted by the fraktur letter $\mathfrak{F}$ and is defined by

$$\mathfrak{F}(f)(\mathbf{k}) = \int_{\mathbb{R}^n} f(\mathbf{r})\, e^{i\mathbf{kr}}\, dr_1 \ldots dr_n. \tag{3}$$

The inverse transform is given by

$$\mathfrak{F}^{-1}(f)(\mathbf{r}) = \frac{1}{(2\pi)^n} \int_{\mathbb{R}^n} f(\mathbf{k})\, e^{-i\mathbf{rk}}\, dk_1 \ldots dk_n. \tag{4}$$

The two- and three-dimensional space is of particular interest in the context of this work. The letters x, y or x, y, z denote the Cartesian coordinates in two- or three-dimensional real space, respectively. The letters k_x, k_y or k_x, k_y, k_z denote the coordinates in two- or three-dimensional reciprocal space, respectively . As a notation for the two- and three-dimensional Fourier transform, the tilde $\tilde{}$ is used as well:

$$\tilde{f}(k_x, k_y) := \mathfrak{F}(f)(k_x, k_y) = \int_{-\infty}^{\infty}\int_{-\infty}^{\infty} f(x, y)\, e^{i(k_x x + k_y y)}\, dxdy. \qquad (5)$$

The n-dimensional convolution (denoted by the symbol $\ll\gg$) is defined by

$$\ll f, g \gg (\mathbf{r}) = \int_{\mathbb{R}^n} f(\mathbf{s})\, g(\mathbf{r} - \mathbf{s})\, ds_1 \ldots ds_n. \qquad (6)$$

The n-dimensional correlation (denoted by the symbol $<>$) is defined by

$$< f, g > (\mathbf{r}) = \int_{\mathbb{R}^n} f(\mathbf{s})\, g^*(\mathbf{s} - \mathbf{r})\, ds_1 \ldots ds_n. \qquad (7)$$

With these definitions, the following basic Fourier theorems are obtained:

Convolution theorem:

$$\mathfrak{F}(\ll f, g \gg) = \mathfrak{F}(f)\, \mathfrak{F}(g) \qquad (8)$$

Autocorrelation theorem:

$$\mathfrak{F}(ff^*) = \frac{1}{(2\pi)^n} < \mathfrak{F}(f),\ \mathfrak{F}(f) > . \qquad (9)$$

Scaling Theorem:

For $g(\mathbf{r}) = f(a\,\mathbf{r})$ the following relation holds:

$$\mathfrak{F}(g)(\mathbf{k}) = \frac{1}{a}\,\mathfrak{F}(f)\left(\frac{\mathbf{k}}{a}\right) \tag{10}$$

Translation theorem:

For $g(\mathbf{r}) = f(\mathbf{r} - \mathbf{a})$ the following relation holds:

$$\mathfrak{F}(g)(\mathbf{k}) = \mathfrak{F}(f)(\mathbf{k})\,e^{i\mathbf{a}\mathbf{k}} \tag{11}$$

Dirac's delta distribution representation:

$$\delta(\mathbf{r} - \mathbf{z}) := \frac{1}{(2\pi)^n} \int\limits_{\mathbb{R}^n} e^{i\mathbf{k}(\mathbf{r}-\mathbf{z})}\,dk_1 \ldots dk_n \tag{12}$$

fulfills

$$f(\mathbf{r}) = \int\limits_{\mathbb{R}^n} f(\mathbf{s})\delta(\mathbf{r} - \mathbf{s})\,ds_1 \ldots ds_n \tag{13}$$

for any continuous function f.

Abbreviations

2D	two-dimensional
3D	three-dimensional
AFM	Atomic force microscope
ASWFM	Axial standing wave fluorescence microscope
CFM	Confocal fluorescence microscope
DNA	Deoxyribonucleic acid
DOF	Degree of freedom
EM	Electron microscope
FM	Fluorescence microscopy
HELM	Harmonic excitation light microscopy
HRP	Horseradish peroxidase
I^2M	Image interference microscopy
I^5M	Image interference microscopy with incoherent interference illumination
LSI	Linear shift invariant
LSWFM	Lateral standing wave fluorescence microscope
NA	Numerical aperture
OSM	Optical sectioning microscopy
OTF	Optical transfer function
PSF	Point spread function
SNOM	Scanning near-field optical microscope
SNR	Signal-to-noise ratio
TIR	Total internal reflection

Chapter 1

Introduction

1.1 Historical outline

Today's human knowledge in natural sciences could only be achieved by employing technical instruments to extend the human perceptivity. One important class of such instruments are microscopes. Originally, the word microscope was used for optical magnifiers but, today, it denotes instruments which visualize a variety of physical properties on a length scale not directly accessible to the human eye. The history of microscopy is characterized by a close interweavement between scientific advancements in the underlying physical principles and manufacturing progresses.

A first milestone for the understanding of image formation in optical microscopes was achieved in 1840 by Carl Friedrich Gauß who established fundamentals of geometric optics. These geometric optics formed the basis for instrument development, however, imaging properties of microscopes were not satisfactorily understood as diffraction effects were out of scope of Gauß's ray-optical treatment. In 1872, Ernst Abbe investigated the imaging process in a microscope in the framework of wave description of light and found a simple relationship

between achievable resolution and wavelength of the employed light. His investigations together with advancements in lens grinding and glass manufacturing permitted the realization of optical microscopes whose resolution approximates the limit imposed by the wave nature of light.

In 1924, De Broglie studied the properties of electron beams and found out that these can be described as waves with very short wavelength. From that point, the idea of building an electron microscope (EM) was evident. In fact, eight years later E. Ruska (Nobel Price 1986) and M. Knoll realized the first EM using magnetic lenses. In 1936, F. Krause could demonstrate an EM with a resolution of better than 100 nm and, thus, outperform the resolving power of optical microscopes. Technical advancements in EM design made it possible to achieve atomic resolution (T. Komoda, 1966) and to observe single deoxyribonucleic acid (DNA) molecules (J. Dubochet, 1970). In the sixties, the scanning electron microscope became technically feasible and could extend the applicability of EMs to surface imaging of three-dimensional objects.

Optical microscopes, however, were still essential due to several inherent drawbacks of electron microscopy: First, the majority of EMs is incompatible with living specimens as the object under observation must be dehydrated. Secondly, a relatively complicated sample preparation is required and, thirdly, the radiation dose sometimes destroys the specimen. The first restriction, however, can be overcome by the new environmental scanning electron microscopes at the expense of a lower resolution.

In the eighties, a variety of microscopes using short range interactions between a scanning probe and the sample emerged. The first one was the scanning tunneling microscope which measures the tunneling current between a metallic tip and the surface of the specimen [10]. In the following years, the physical properties that could be measured using scanning probe microscopes were strongly extended. In 1984, the scanning near-field optical microscope (SNOM) was in-

vented which enables measurement of optical properties without being restricted by the wave propagation of light [66]. In 1986, the atomic force microscope (AFM) was developed which measures the force interaction between tip and sample [9]. Scanning probe microscopes based on various physical interactions (e.g. surface potential measurements [46]; lateral force measurements [59]) were developed and it could be demonstrated that the scanning probe techniques function in aqueous environments as well [76].

However, scanning probe microscopes share some common disadvantages. One is, that these methods are very slow in comparison to optical far-field microscopes due to the mechanical scanning. Furthermore, the interpretation of scanning probe images is often complicated as the local tip-sample interactions are influenced by a variety of physical effects. Last but not least, the scanning probe microscopes cannot see into an object as its imaging process is restricted to surfaces. A promising approach to overcome some of these limitations are systems which combine scanning probe techniques with light microscopy [79] or electron microscopy [80].

The drawbacks of electron and scanning probe microscopy were and are today incitements for several attempts to further extend the applicability of far-field light microscopes, particularly for investigations of biological specimens. Many problems found in biological research require microscopes that combine high resolution with sufficient chemical contrast. Fluorescence microscopy (FM) is capable of selectively imaging individual components of the specimens as dyes can be bound to specific molecules. Advanced fluorescence techniques[1] have become a standard tool for localizing DNA sequences [25] or perform immunological investigations [58, 72] and have successfully proven their capability to image living cells [16].

An important improvement concerning the resolution of optical far-field microscopes was the invention of the confocal scanning microscope [60, 75, 13]. By scanning a focused laser beam through the

[1] For an overview article see [82].

specimen, these types of microscopes overcame Abbe's century old limit by a factor of 1.5 and could significantly increase the three-dimensional imaging capabilities. Today, the confocal microscope has become an essential tool for investigations in cell biology.

The high intensities of the focused laser beam in the confocal microscope enabled the development of methods for resolution enhancement based on non-linear effects such as two-photon absorption [22, 41] or stimulated-emission depletion [50]. Due to the restricted number of suitable dyes, however, non-linear methods are not yet routinely employed.

Another approach to increase the resolution does not affect the image formation but the image interpretation. By electronic post-processing of images produced by conventional or confocal light microscopes, a significantly enhanced resolution can be achieved if *a priori* knowledge about the sample is present [19, 21]. However, these methods are sensitive against noise in the images, specifically posing a problem in fluorescence microscopy.

1.1.1 Resolution enhancement by harmonic excitation

Since Ernst Abbe's works, far-field light microscopes are known to produce Airy patterns from point sources (see Fig. 1.1). The most common definition for resolution of light microscopes is the well known Rayleigh criterion. According to Rayleigh, two self-luminous points are considered as just resolved if their lateral separation equals the radius of the first dark ring of the Airy pattern. This radius is denoted as the Rayleigh distance; the contrast dip for two just resolved points amounts to 27%. The Rayleigh criterion, however, is somewhat arbitrary as assumptions about the observable contrast dip are made. A more universal definition for resolution can be obtained in frequency domain. From the object spectrum, the microscope exclusively transfers spectral components within a bounded region, called

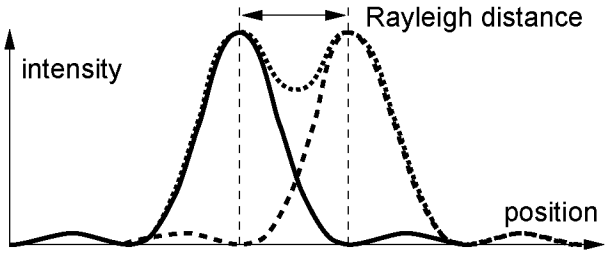

Figure 1.1: Image produced by a light microscope for two point sources separated by the Rayleigh distance (incoherent imaging).

the passband of the microscope. Thus, the extent of the passband is a reasonable measure for the resolution of light microscopes.[2]

In harmonic excitation light microscopy (HELM), described in this thesis, the extent of the passband is more than doubled by employing space harmonic (i.e. sinusoidal) excitation patterns. The key idea of HELM is a widespread practice in communications engineering and many other disciplines. The principle is known as frequency mixing or heterodyne conversion. Basically, frequency mixing describes the fact that signals can be shifted in frequency domain by modulation with harmonic functions. In HELM, additional components of the object spectrum are brought into the passband of the microscope by this shift.

The idea of frequency mixing has first been applied to optical microscopy more than 30 years ago by Lukosz [57, 56]. The method described then, however, was not practical for high resolution microscopy as it required a moving mask in the object plane and a synchronized one in the image plane.

[2]From the scaling theorem for Fourier transforms (Eq. 10) it follows that the width of the frequency representation of a function is reciprocal to the width of the spatial representation. For this reason, an extension of the passband of the microscope corresponds to a narrowing of the point response.

In relation to Lukosz's method, the one described in this thesis [30, 31] shows two key differences: First, the harmonic excitation is realized by illuminating the specimen with an interference pattern of a laser source. This is a practical way to produce fine illumination structures in the object plane of even high resolution microscopes. Secondly, the synchronized mask in the image plane has been omitted by using electronic postprocessing of the images. As a result, the method can be easily implemented on conventional fluorescence microscopes.

Chapter 2

Summary of the method

The objective of this chapter is to briefly summarize the HELM method without overloading it with details. Aspects which are not essential for understanding the HELM principle are discussed later in chapters 3 and 4.

In the two-dimensional HELM setup four laser beams, which can be considered as plane waves, interfere in the object plane of a microscope under a common angle α to the optical axis (see Fig. 2.1). Neglecting scaling factors, the resulting intensity pattern I of the electric field can be written as

$$I(x, y) = 2 + \cos(ux + \Delta_x) + \cos(uy + \Delta_y), \tag{2.1}$$

where $u = 4\pi n \sin(\alpha)/\lambda$ is the spatial frequency of the harmonic excitation, n=1.52 is the refractive index of glass, λ is the vacuum wavelength of excitation and Δ_x, Δ_y describe the shift of the pattern relative to the sample in x- and y-direction, respectively (see subsection 3.3.1 for a derivation of Eq. 2.1). For the illuminated sample, the fluorescence ϕ is proportional to the excitation intensity I times the density of dye-molecules ψ, the latter called original image in the

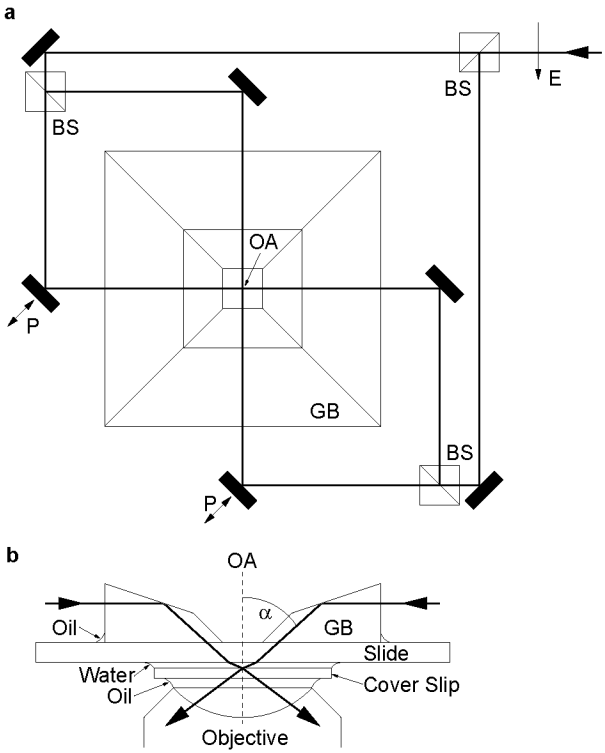

Figure 2.1: Optical train for generation of a two-dimensional interference pattern in the object plane of the microscope. (**a**) top view. A collimated laser beam is split by beam splitters BS into four beams of equal intensity that cross at the optical axis OA of the microscope.The electrical polarization E is parallel to the image plane, so only antiparallel beams and not orthogonally oriented ones interfere. Piezo-actuated mirrors P are used to vary the phase of the x- and y-interference patterns independently. (**b**) cut view through the optical axis. The four laser beams (only 2 shown) are coupled to the object by a glass block GB which is oil-immersed to the slide. The beam's angle to the optical axis is α=55° in the glass block, corresponding to 70° in the water layer between slide and cover slip.

following text (see section 3.2):

$$\phi(x,y) = \psi(x,y)I(x,y) \tag{2.2}$$

With ˜ denoting the two-dimensional Fourier transform of a variable, one obtains for the spectrum of the illuminated sample (by inserting Eq. 2.1 into Eq. 2.2 and using the convolution theorem Eq. 8):

$$\tilde{\phi}(k_x,k_y) = 4\overbrace{\tilde{\psi}(k_x,k_y)}^{=:A} + e^{i\Delta_x}\overbrace{\tilde{\psi}(k_x+u,k_y)}^{=:B} + e^{-i\Delta_x}\overbrace{\tilde{\psi}(k_x-u,k_y)}^{=:C} + e^{i\Delta_y}\overbrace{\tilde{\psi}(k_x,k_y+u)}^{=:D} + e^{-i\Delta_y}\overbrace{\tilde{\psi}(k_x,k_y-u)}^{=:E} \tag{2.3}$$

The spectrum $\tilde{\phi}$ is a superposition of the original spectrum A plus four spectra $B..E$ that have been shifted along the k_x- and k_y-axis in positive and negative reciprocal space direction, respectively. In frequency domain, the imaging property of the microscope can be described in two dimensions, as well as in three, by a multiplication with an instrument-specific function, called the optical transfer function (OTF, see section 3.1). In regions where the OTF is non-zero, called the support of the OTF or the passband, the frequency components of the sample, in principle, can be reconstructed, while outside this region the information is irrecoverably lost. For fluorescence microscopy, the passband is a circular region centered at the origin with a cut-off radius $k_c = 4\pi\mathrm{NA}/\lambda$, where λ is the vacuum-wavelength of emission (about 540 nm for the fluorescein-like dyes) and NA is the numerical aperture of the objective.

The occurrence of the shifted spectra $B..E$ in Eq. 2.3 as a result of the spatially harmonic excitation is the basis of HELM. Through this shift, additional high frequency regions of the optical spectrum are brought into the passband of the microscope. Fig. 2.2 shows the enhanced support of the OTF that is achieved by the current setup.

The images acquired for HELM, however, must be postprocessed electronically to extract the individual components A..E and to rearrange these to the final high resolution image. This is possible by

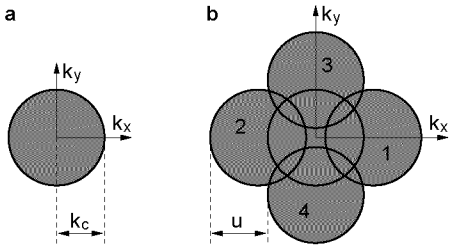

Figure 2.2: The enhancement of the support of the OTF by means of standing wave excitation. (**a**) shows the circular passband for standard fluorescence microscopy with cut-off frequency k_c. (**b**) is the cloverleaf-shaped OTF of HELM. The four circular regions $1, 2, 3, 4$ are relocated copies of the circular passband from (**a**) and correspond to the components B,C,D,E from Eq. 2.3, respectively. The displacement u is equal to the spatial frequency of the harmonic excitation.

recording five images for which the nodes and antinodes of the excitation pattern are at different positions. In the setup, the x- and y-phase offsets (Δ_x, Δ_y) are sequentially adjusted to the values $(0, 0)$, $(\pi/2, 0)$, $(\pi, 0)$, $(0, \pi/2)$, $(0, \pi)$ by piezo actuators.

For the Fourier transforms of the five acquired images, Eq. 2.3 holds with the appropriate coefficients $e^{\pm i\Delta_x}$ and $e^{\pm i\Delta_y}$. Thus, a 5×5 set of linear equations is obtained which can be solved for the five spectral components $A..E$. Numerically, a fast Fourier transform is performed on the measured images and the set of linear equations is solved for every pixel. By doing so, the spectral components $A \ldots E$ are obtained which, additionally, have been attenuated by the OTF of the microscope. The remaining computational task is to shift the components back to their original position and, finally, superimpose them taking into account the attenuation by the microscope's OTF. All calculation steps together require only a few seconds on a standard personal computer for a 512×512 image.

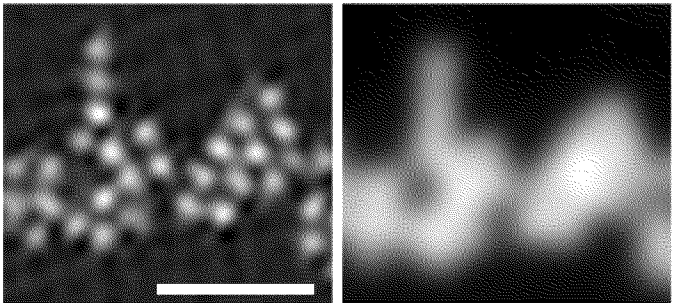

Figure 2.3: Fluorescent beads with a diameter of 200 nm imaged with HELM (left) and standard fluorescence microscopy (right). Scale bar is 1 μm. The wavelength of emission is 540 nm and the numerical aperture of the objective is 1.4. The center-to-center distance of the tightly packed beads approximates the Rayleigh limit which is 240 nm for these conditions. The almost invisible contrast dip between the individual beads in the right image is a consequence of the fact that the beads are not point sources. Furthermore, one has to take into account that, for water immersed beads, the effective NA of the objective (nominal: 1.4) becomes smaller [44].

Fig. 2.3 shows beads with a diameter of 200 nm which approximately equals the Rayleigh limit for standard fluorescence microscopy.

The HELM image (left) demonstrates that such beads can be clearly distinguished, even when they are closely packed. In the standard fluorescence microscopy image (right), in contrast, the individual beads remain blurred. In relation to the confocal fluorescence microscope, there are several advantages of HELM:

- The resolution enhancement relativ to conventional FM amounts to more than a factor of 2 compared to 1.5 which is achieved by confocal scanning under ideal conditions [78].

- In HELM, all photons entering the lenses can be exploited for image formation. In CFM, in contrast, a pinhole in the imaging path makes it necessary to trade off resolution vs. the fraction of photons which contribute to the image. As a result, the signal-to-noise level of CFM is deteriorated.

- HELM is well suited for high speed imaging. In CFM, fundamental reasons imposed by dye-saturation (see subsection 5.1.1) as well as practical ones imposed by mechanical scanning limit the imaging speed.

For these reasons and as the system requirements for microscopes based on the principle of harmonic excitation are similar to those of confocal devices, HELM systems could become a commercial alternative to confocal ones.

Chapter 3

Theory

3.1 The microscope as linear shift invariant (LSI) system

From a very general perspective, the propagation of electromagnetic waves within a microscope is described by the Maxwell equations together with the boundary conditions for the transitions between different media, e.g. the air-glass interfaces at the lens surfaces [45]. The time dependent electromagnetic disturbance at any point in three-dimensional space can be described by the electric field $\mathbf{E}(\mathbf{r}, t)$ as well as by the magnetic induction $\mathbf{B}(\mathbf{r}, t)$. For this thesis, it is more appropriate to write the equations using the electric field as this one is directly related to important optical effects such as photon absorption by atoms or molecules.

The considerations are restricted to the case of time harmonic (monochromatic) excitation. As a consequence of the harmonic excitation, the electric field vector $\mathbf{E}$ at any point $\mathbf{r} \in \mathbb{R}^3$ in space is also time harmonic and, therefore, can be written by using the complex time-

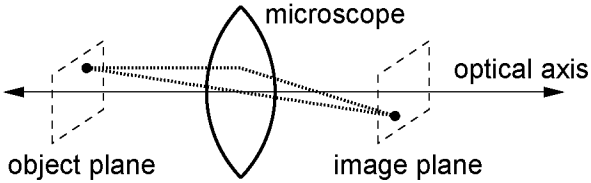

Figure 3.1: The microscope system studied.

independent notation:

$$\mathbf{E}(\mathbf{r},t) = \mathrm{Re}\left(\mathbf{E}(\mathbf{r})\, e^{iwt}\right), \tag{3.1}$$

where $\mathbf{E}(\mathbf{r},t) \in \mathbb{R}^3$ and $\mathbf{E}(\mathbf{r}) \in \mathbb{C}^3$.

> In the context of this work, the complex time-independent notation $\mathbf{E}(\mathbf{r})$ is used with the implicit time dependence given according to Eq. 3.1.

With this notation, one can describe linear as well as elliptical polarized light.

Now, a microscope according to Fig. 3.1 is considered which performs two-dimensional imaging between object plane and image plane. The imaging property of the microscope can be described in the framework of linear system theory. The electrical disturbance in the object plane is denoted by the Greek letter $\boldsymbol{\phi}$ and that one in the image plane by $\boldsymbol{\theta}$. Using this notation, the microscope's imaging process is a mapping of functions $\boldsymbol{\phi} : \mathbb{R}^2 \to \mathbb{C}^3$ to functions $\boldsymbol{\theta} : \mathbb{R}^2 \to \mathbb{C}^3$. This mapping is characterized by the following two basic properties:

Linearity The response of the microscope to a superposition of disturbances in the object plane is the superposition of the responses to the individual disturbances:

$$\boldsymbol{\theta}\left(\lambda\boldsymbol{\phi}_1 + \mu\boldsymbol{\phi}_2\right) = \lambda\boldsymbol{\theta}(\boldsymbol{\phi}_1) + \mu\boldsymbol{\theta}(\boldsymbol{\phi}_2)\,. \tag{3.2}$$

This property is a consequence of the linearity of the Maxwell equations.

Shift invariance The response to a shifted disturbance is the shifted response to the unshifted disturbance:

$$\boldsymbol{\theta}(\boldsymbol{\phi}(\mathbf{u}+\mathbf{a}))(\mathbf{v}) = \boldsymbol{\theta}(\boldsymbol{\phi}(\mathbf{u}))(\mathbf{v}+\mathbf{a}), \tag{3.3}$$

with $\mathbf{u}, \mathbf{v}, \mathbf{a} \in \mathbb{R}^2$ and where magnification and mirroring of the microscope is neglected. The shift invariance is not strictly true for real microscopes as aberrations increase for points far away from the optical axis. Nevertheless, the shift invariance is a good approximation to the real situation.

For linear shift invariant (LSI) systems, the imaging property can be completely described by the response of the system to a point disturbance, the so-called point spread function (PSF):[1]

$$\theta(\delta(\mathbf{u})) =: \mathrm{PSF}(\mathbf{u}), \tag{3.4}$$

where δ denotes the two-dimensional Dirac's delta-distribution. The response of a LSI system to an arbitrary disturbance can be seen to be the convolution of the disturbance with the PSF of the system:

$$\begin{aligned}
\theta(\phi(\mathbf{u})) &\overset{\text{Eq. 13}}{=} \theta\left(\int_{\mathbb{R}^2} \phi(\mathbf{v})\delta(\mathbf{u}-\mathbf{v})\, dv_1 dv_2\right) \\
&\overset{\text{Linearity}}{=} \int_{\mathbb{R}^2} \theta\left(\phi(\mathbf{v})\delta(\mathbf{u}-\mathbf{v})\right)\, dv_1 dv_2 \\
&\overset{\text{Linearity}}{=} \int_{\mathbb{R}^2} \phi(\mathbf{v})\theta\left(\delta(\mathbf{u}-\mathbf{v})\right)\, dv_1 dv_2
\end{aligned} \tag{3.5}$$

[1] Henceforth, only scalar fields are considered for simplicity. For non-scalar problems, the PSF-formalism can be easily extended to vector fields as well.

$$\overset{\text{Shift invariance}}{=} \int_{\mathbb{R}^2} \phi(\mathbf{v})\mathrm{PSF}(\mathbf{u}-\mathbf{v})\,dv_1 dv_2$$

$$\overset{\text{Eq. 6}}{=} \ll \phi, \mathrm{PSF} \gg \tag{3.6}$$

For optical systems, the Fourier transform of the point spread function is called the optical transfer function (OTF). For the Fourier transform of the image $\tilde{\theta}$ one obtains by using the convolution theorem (Eq. 8):

$$\tilde{\theta} = \ll \widetilde{\phi, \mathrm{PSF}} \gg = \tilde{\phi} \times \widetilde{\mathrm{PSF}} = \tilde{\phi} \times \mathrm{OTF} \tag{3.7}$$

According to Eq. 3.7, the imaging property of a microscope (or, more generally, the transmission characteristic of a LSI system) can be described by a simple multiplicative filtering operation in Fourier space.

The coherent OTF of a microscope can be calculated by scalar diffraction theory [33, 12]. Except for scaling factors, the coherent OTF of a microscope turns out to be the pupil function of the objective.

In case of incoherent illumination or fluorescence, the object cannot be described adequately by a complex field amplitude as there is no fixed phase relation between different object points. Instead, a description by emission *intensity* is appropriate since systems of incoherent emitters are linear in intensity. The derivation of the incoherent OTF is straightforward: The intensity response to a point object is the squared amplitude response to a point object. Therefore, the incoherent OTF is the autocorrelation of the coherent one (autocorrelation theorem, Eq. 9). The coherent and incoherent OTF for a scalar system with circular pupil are shown in Fig. 3.2.

For high NA objectives, the scalar theory is not strictly applicable. Calculations taking into account the vector nature of light also exist [77] and include the case of high NA optics. In this thesis, the scalar theory is used for qualitative descriptions while the measured OTF is employed by the image reconstruction algorithm. The measured OTF covers high NA effects as well as imperfections in the optical components.

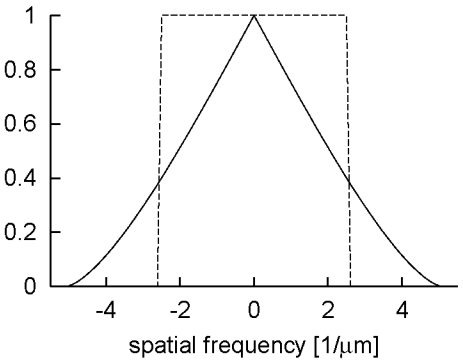

Figure 3.2: Coherent (dashed line) and incoherent (solid line) optical transfer functions for an objective with a NA of 1.4 and a wavelength of 540 nm. The rotational symmetric two-dimensional OTF is obtained by rotating the graphs around the ordinate.

3.2 Fluorescence

In this section, the basic properties of fluorescence and its impact for fluorescence microscopy will be discussed. Fig. 3.3 shows a simplified energy level scheme for a typical fluorophore. The lifetime of the excited states is typically in the order of 1 ns and, hence, about six orders of magnitude larger then the period of exciting oscillation. As a consequence, the fluorophores destroy the coherence of the exciting electromagnetic wave and emit —to a very good approximation— incoherently. This is a very important property of fluorescence emission as it allows one to describe the image formation of the microscope by the theory of incoherent imaging regardless of the coherence of excitation light.

Because the transition from ground level s_0 to the exited state s_1 is an electrical dipole transition, the fluorescence absorption rate (FAR)

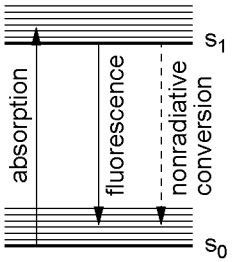

Figure 3.3: Simplified representation of the energetic states of a fluorophore. Higher vibrational sublevels are indicated by thin lines. By photon absorption, the fluorophore is excited into a vibrational sublevel of the excited state s_1 from which it quickly relaxes to the lowest sublevel (vibrational relaxation, not shown). Relaxation to the ground state s_0 is possible by fluorescence or by non-radiative conversion both followed by vibrational relaxation to the lowest sublevel of s_0 (not shown). The energy difference between absorption photon energy and emission photon energy is the well known Stokes shift. The fraction of the exited fluorophores that relax radiatively is called the quantum efficiency of the fluorophore.

is proportional to the square of the electrical field strength oriented parallel to the absorption dipole moment:

$$\mathrm{FAR} = c\,|\mathbf{E}\,\mathbf{n}_{\mathrm{dm}}|^2, \tag{3.8}$$

where $\mathbf{n}_{\mathrm{dm}}$ is the normalized absorption dipole moment and c is a constant depending on the particular fluorophore [71, chapter 2].

Now an ensemble of N isotropically distributed fluorophores is considered. In this case, one would probably expect that the fluorescence absorption rate of the ensemble is proportional to the squared modulus of the complex electric field independent of the polarization state. For linear polarized light, this is in fact quite obvious, but, for arbitrary polarization states, it is not evident. As the interference

generating apparatus of the setup produces excitation patterns with complicated polarization states (see subsection 3.3.1), further calculations are required to validate the expectation for such polarization states.

For isotropically distributed fluorophores, the number of fluorophores ∂N oriented per solid angle $\partial\Omega$ is

$$\frac{\partial N}{\partial \Omega} = \frac{N}{4\pi}. \tag{3.9}$$

The normalized absorption dipole moment $\mathbf{n}_{\mathrm{dm}}$ belonging to a number of fluorophores oriented in a direction specified by the azimuthal and polar angles ζ and η, respectively, is

$$\mathbf{n}_{\mathrm{dm}} = \begin{pmatrix} \cos(\zeta)\cos(\eta) \\ \sin(\zeta)\cos(\eta) \\ \sin(\eta) \end{pmatrix}. \tag{3.10}$$

To obtain the fluorescence absorption rate of the ensemble, Eq. 3.8 has to be summed up for all fluorophores. To simplify the calculations without affecting the general applicability, it is assumed that the polarization ellipsis of the exciting electric field is within the x-y-plane. Thus, the electrical field vector can be written as

$$\mathbf{E} = \begin{pmatrix} E_x e^{i\rho_x} \\ E_y e^{i\rho_y} \\ 0 \end{pmatrix}, \tag{3.11}$$

where the real field amplitudes E_x, E_y and the phase factors $e^{i\rho_x}, e^{i\rho_y}$ account for an arbitrary amplitude and ellipticity of polarization. For the fluorescence absorption rate $\mathrm{FAR}_{\sum}$ of the ensemble one obtains

$$
\begin{aligned}
\mathrm{FAR}_{\sum} &= c \int\limits_{\text{all fluorophores}} |\mathbf{E}\,\mathbf{n}_{\mathrm{dm}}|^2\, dN \\
&= \frac{cN}{4\pi} \int\limits_{\text{all orientations}} |\mathbf{E}\,\mathbf{n}_{\mathrm{dm}}|^2\, d\Omega \\
&= \frac{cN}{4\pi} \int_0^{2\pi} \int_{-\pi/2}^{\pi/2} \left| \begin{pmatrix} E_x e^{i\rho_x} \\ E_y e^{i\rho_y} \\ 0 \end{pmatrix} \begin{pmatrix} \cos(\zeta)\cos(\eta) \\ \sin(\zeta)\cos(\eta) \\ \sin(\eta) \end{pmatrix} \right|^2 \cos(\eta)\, d\eta\, d\zeta \\
&= \frac{cN}{4\pi} \int_{-\pi/2}^{\pi/2} \cos^3(\eta)\, d\eta \times \int_0^{2\pi} \Big[E_x^2 \cos^2(\zeta) + \\
&\quad E_y^2 \cos^2(\rho_y - \rho_x) \sin^2(\zeta) + E_y^2 \sin^2(\rho_y - \rho_x) \sin^2(\zeta) \Big] d\zeta \\
&= \frac{cN}{4\pi}\, \frac{4}{3} \left(E_x^2 \int_0^{2\pi} \cos^2(\zeta)\, d\zeta + E_y^2 \int_0^{2\pi} \sin^2(\zeta)\, d\zeta \right) \\
&= \frac{cN}{3} \left(E_x^2 + E_y^2 \right) = \frac{cN}{3} |\mathbf{E}|^2. \qquad (3.12)
\end{aligned}
$$

For spatially distributed fluorophores, the number of fluorophores N within a volume element ∂V is

$$N = \partial V\, \psi, \qquad (3.13)$$

where ψ is the density of fluorophores in the specimen. With QE denoting the quantum efficiency of the fluorophore, one obtains for the fluorescence ϕ emitted per volume

$$\phi(\mathbf{r}) = \mathrm{QE} \frac{\partial \left(\mathrm{FAR}_{\sum} \right)}{\partial V} = \frac{c\,\mathrm{QE}}{3}\, \psi(\mathbf{r})\, |\mathbf{E}(\mathbf{r})|^2. \qquad (3.14)$$

Eq. 3.14 is the basic relation describing the fluorescence emission rate of isotropically distributed fluorophores for *any polarization state of the exciting light*. In the literature, Eq. 3.14 can be found in a somewhat simpler form using the intensity instead of the electric field and omitting scaling factors:

$$\phi(\mathbf{r}) \propto \psi(\mathbf{r})\, I(\mathbf{r}). \tag{3.15}$$

Eq. 3.15 is a specialization of Eq. 3.14 for excitation with plane waves for which $|\mathbf{E}|^2$ is proportional to the energy flux or intensity of the wave [26, chapter 20]. If the generalized intensity I is defined by setting it proportional to the squared modulus of the complex electric field (i.e. $I(\mathbf{r}) \propto |\mathbf{E}(\mathbf{r})|^2$), Eq. 3.15 is also valid for the complicated excitation patterns used in HELM.

Eq. 3.15 is very fundamental for HELM. It states that the density of dyes in the specimen ψ is modulated by the excitation intensity I before being imaged by the microscope.

3.2.1 Fluorescence polarization

In this subsection, the effect of polarization of emitted fluorescence light will be briefly discussed. Fig. 3.4 shows the geometry considered. The degree of polarization p is defined by

$$p = \frac{\phi_\parallel - \phi_\perp}{\phi_\parallel + \phi_\perp}, \tag{3.16}$$

where $\phi_\parallel$ and $\phi_\perp$ is the fluorescence emission polarized along the y- and x-axis, respectively. In general, the degree of polarization is dependent on the angle between absorption dipole moment and emission dipole moment, the angular distribution of fluorophores and its rotational mobility. For many situations, it can be assumed that the fluorophores are isotropically distributed and that their orientations

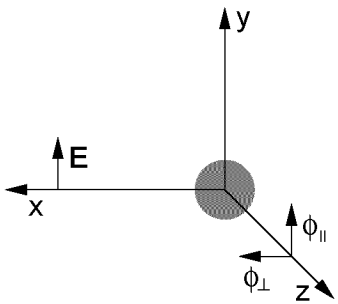

Figure 3.4: Geometry for observation of the degree of polarization. The electrical polarization of excitation is parallel to the y-axis. The grey circle represents the region containing fluorophores. Fluorescence ϕ is observed along the z-axis. Two degrees of polarization are discriminated, the first one parallel to the y-axis ($\phi_{\parallel}$) and the second one perpendicular ($\phi_{\perp}$). The axis labeling is consistent to the one used later to describe the microscope geometry.

are fixed. Then, the polarization p_0 becomes

$$p_0 = \frac{3\cos^2(\beta) - 1}{\cos^2(\beta) + 3}, \tag{3.17}$$

where β is the angle between absorption and emission dipole moment [7]. The minimum and maximum value for p_0 are $+1/2$ and $-1/3$, respectively, the maximum occurs for coincident dipole moments ($\beta = 0$), the minimum for perpendicular ones ($\beta = 90°$).

If the fluorophores are free to rotate, the degree of polarization is reduced as the orientation of the fluorophores changes during the lifetime of the excited state by thermal motion [73, 71]. This effect is important for dye molecules in aqueous environment but not for fluorophores embedded in solids, e.g. fluorescent polymer beads. For dyes bound to specific molecules in biological specimens, the situation

can be more complicated as dyes potentially have a restricted but not vanishing number of degrees of rotational freedom.

3.2.2 Dye-saturation

As mentioned before in this section, the excited states of typical fluorophores have a relatively long lifetime of about 1 ns. For a sufficient high excitation power, a non-negligible fraction of the fluorophores can reside in the excited state, an effect which is named "ground state depletion" [7] or "dye saturation" [70]. As a consequence of the decreasing number of fluorophores in the ground state, the fluorescence emission rate cannot exceed an upper limit. This imposes a fundamental limit on the imaging speed of fluorescence microscopy, particularly for confocal scanning.

Under steady state conditions, the fluorescence emission rate FER of a dye becomes

$$\mathrm{FER} = \frac{\alpha}{\alpha\tau_F + 1}, \tag{3.18}$$

where τ_F is the lifetime of the excited state and $\alpha = \frac{I\sigma}{h\nu}$ with I is the excitation intensity, σ is the absorption cross section and $h\nu$ is the absorbed photon energy [70]. One sees that the fluorescence emission rate is not linear in excitation power as it is limited by $\lim_{\alpha\to\infty}(\mathrm{FER}) = \frac{1}{\tau_F}$ even for infinite excitation intensity (see Fig.3.5). For the so-called saturating intensity I_{sat}, the fluorescence emission rate equals one half of its upper limit. For I_{sat} this leads to

$$I_{\mathrm{sat}} = \frac{h\nu}{\sigma\tau_F}. \tag{3.19}$$

For a typical fluorophore (Rhodamin B, absorption cross section $\sigma = 1 \times 10^{-20}$ m^2, $\tau_F = 1$ns, [70]), the saturating intensity I_{sat} is approx. $10^{10}\,\frac{\mathrm{W}}{\mathrm{m}^2}$.

It should be noted, that dye saturation is independent of the density of dyes at a certain location. Consequently, dye saturation does

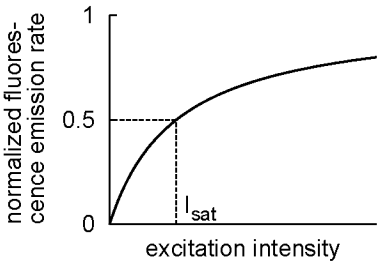

Figure 3.5: Dependence of fluorescence emission rate on excitation intensity. The fluorescence emission rate is normalized to its maximum value.

not decrease the contrast of a fluorescence microscope image but reduces the number of photons emitted by the specimen and, thus, results in a darker and noisier image.

3.3 Harmonic excitation light microscopy (HELM)

3.3.1 Interference generating apparatus

In this subsection, an expression for the electrical field distribution which is produced by the interference generating apparatus (see Fig. 2.1) will be derived. Fig. 3.6 shows the geometry for one pair of incident laser beams (oriented in the x-z-plane and referred to herein as x-pair). The other pair (not shown, oriented in the y-z-plane and referred to herein as y-pair) is polarized perpendicular to the ones shown and can be considered independently later.

Due to the partial reflection of the two incident beams at the water-glass boundary, the electric field is effectively generated by interference of four plane waves with wave vectors $k_{1i}, k_{2i}, k_{1r}, k_{2r}$.

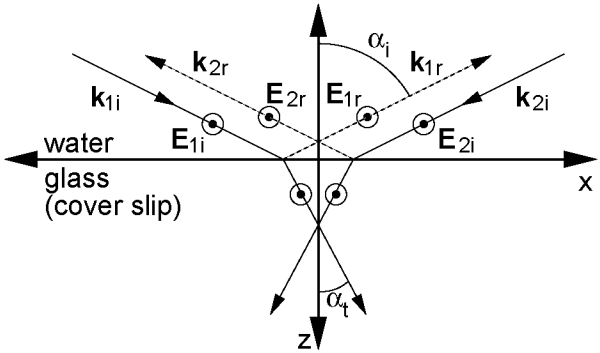

Figure 3.6: Plane electromagnetic waves producing the interference pattern at the water-glass boundary. For clarity, the two incident beams ($\mathbf{k}_{1i}$ and $\mathbf{k}_{2i}$) are horizontally displaced.

It turns out, that the reflected beams lead to an unwanted z-dependence of the intensity distribution which reduces the excitation intensity in the focal plane.

Because all beams are polarized along the y-axis, a scalar notation for the electrical field strength is used:

$$E_{1i} = E_1\, e^{-i(k_x x + k_z z)}, \tag{3.20}$$

$$E_{1r} = -E_1\, R\, e^{-i(k_x x - k_z z)}, \tag{3.21}$$

$$E_{2i} = E_2\, e^{i\Delta}\, e^{-i(-k_x x + k_z z)} \quad \text{and} \tag{3.22}$$

$$E_{2r} = -E_2\, e^{i\Delta}\, R\, e^{-i(-k_x x - k_z z)}, \tag{3.23}$$

where E_1, E_2 are the field amplitudes of the incident beams,[2] where

$$R = \frac{\sin(\alpha_i - \alpha_t)}{\sin(\alpha_i + \alpha_t)} \tag{3.24}$$

[2]The negative signs of E_{1r} and E_{2r} describe the 180° phase shift induced by reflection at an optically denser medium.

is the coefficient of reflection according to the *Fresnel formulae* [12] with α_i the incident beam's angle to the interface normal vector (Fig. 3.6) and with

$$\alpha_t = \arcsin\left(\frac{n_{\text{water}}}{n_{\text{glass}}}\sin(\alpha_i)\right) \tag{3.25}$$

the transmitted beam's angle to the interface normal vector (with n_{water} and n_{glass} the refractive indices of water and glass, respectively) and where

$$k_x = 2\pi\, n_{\text{water}}\, \sin(\alpha_i)/\lambda \qquad \text{and} \tag{3.26}$$

$$k_z = 2\pi\, n_{\text{water}}\, \cos(\alpha_i)/\lambda \tag{3.27}$$

are the x-and z-component of the wave vector of the left incident beam (with λ the vacuum wavelength of the incident plane wave) and where $e^{i\Delta}$ accounts for an arbitrary phase shift between the two incident waves. The resulting electric interference field E_{res} is the sum of the two incident electric field distributions plus the two reflected ones. By using Eq. 3.20 to Eq. 3.23 and performing tedious but basic calculations, one obtains

$$\begin{aligned} E_{\text{res}} &= E_{1\text{i}} + E_{1\text{r}} + E_{2\text{i}} + E_{2\text{r}} \\ &= 2\,E_1 e^{i\frac{\Delta}{2}} \cos\left(k_x x + \frac{\Delta}{2}\right)\Big[(1-R)e^{-ik_z z} - R\,2i\sin(k_z z)\Big] + \\ &\quad (E_2 - E_1)e^{i\Delta}e^{ik_x x}\Big[(1-R)e^{-ik_z z} - R\,2i\sin(k_z z)\Big]. \end{aligned} \tag{3.28}$$

For the intensity distribution I (more strictly the squared modulus of the electrical field, see section 3.2 for motivation of this generalized intensity definition) one obtains

$$I = |E_{\mathrm{res}}|^2 = \overbrace{(E_2^2 + E_1^2)\left(1 + \underbrace{\frac{2E_1E_2}{E_1^2 + E_2^2}}_{=:M_{\parallel}} \cos(2k_x x + \Delta)\right)}^{=:F_{\parallel}} \times \overbrace{(1 + R^2)\left(1 - \underbrace{\frac{2R}{1 + R^2}}_{=:M_{\perp}} \cos(2k_z z)\right)}^{=:F_{\perp}}. \tag{3.29}$$

As can be seen from Eq. 3.29, the spatial dependence of the intensity consists of two factors $F_{\parallel}$ and $F_{\perp}$ which depend only on the x- and z-coordinate, respectively.

$F_{\parallel}$ provides cosinusoidal x-modulation of the intensity distribution which is the basis of the HELM method. The x-modulation depth $M_{\parallel}$ depends on the ratio of the field amplitudes E_1, E_2 of the incident beams. For equivalent field amplitudes ($E_1 = E_2$ leading to $M_{\parallel} = 1$), a pure standing wave with nodes of vanishing electrical field is obtained. For different amplitudes $E_1 \neq E_2$, the modulation depth $M_{\parallel}$ becomes smaller than unity as the field consists of a standing wave plus a propagating one. The latter one results in an additional DC-component of the intensity distribution.

$F_{\perp}$ leads to an unwanted z-modulation with a node at the water-glass boundary. For increasing coefficient of reflection R, the intensity at the interface ($z = 0$) is reduced by a factor of $1 - M_{\perp}$ while the intensity is enhanced by $1 + M_{\perp}$ for the antinodal planes at $z = -(\pi/k_z)(l+1/2)$ with $l \in \mathbb{N}^+$. Table 3.1 shows the relative attenuation ratio $(1 - M_{\perp})/(1 + M_{\perp})$ for different incident beam's angles α_i.

In most cases, the object has to be located in direct proximity to the cover slip, first to ensure best imaging fidelity of oil-immersion objectives and, secondly, as standard sample preparations deposit the specimen onto the cover slip. Then, the first antinodal plane of the

α_i	α_t	R	$M_\perp$	$(1-M_\perp)/(1+M_\perp)$
50°	42.1°	0.14	0.27	0.57
60°	49.3°	0.20	0.38	0.45
70°	55.3°	0.31	0.57	0.28
80°	59.5°	0.54	0.84	0.08
85°	60.7°	0.73	0.95	0.02

Table 3.1: Calculated values for the intensity attenuation rate of the nodal planes. The calculations are based on a refractive index of 1.33 for water and 1.52 for glass. α_t is calculated by Eq. 3.25, R is calculated by Eq. 3.24 and $M_\perp$ equals $\frac{2R}{1+R^2}$ according to Eq. 3.29. The last column shows the factor by which the intensity is decreased for nodal planes relative to antinodal ones.

z-modulation coincides with the focal plane of the microscope and, as a consequence, the out-of-focus blur for images of three-dimensional objects is enhanced relative to the in-focus components. As this effect strongly increases for incident beam's angles α_i approximating 90°, it has to be taken into account when discussing the optimal α_i in subsection 3.3.3.[3,4]

The polarization of the interference field

In the last paragraphs, an expression was derived for the y-polarized electrical field produced by interference of the x-pair of incident laser beams oriented in the x-z-plane. Now, the situation when the y-pair of incident beams (oriented in the y-z-plane, not shown in Fig. 3.6) is also present will be considered. The resulting polarization of

[3]One possibility to reduce the unwanted z-modulation would be a dielectric anti reflection coating on the cover slip.

[4]The application of mesh-like interference patterns for optical trapping are discussed in appendix A. For an optical trap, working near flat incidence (i.e. $\alpha_i \approx 90°$) is advantageous.

the electrical field distribution will be discussed and its impact on fluorescence will be studied. The considerations are made under the following two constraints:

1. equal amplitudes of all four incident beams
2. points at the interface (i.e. $z = 0$)

Then, Eq. 3.28 becomes

$$E_{\text{res}} = 2(1-R)E_1\, e^{i\frac{\Delta}{2}} \cos\left(k_x x + \frac{\Delta}{2}\right). \tag{3.30}$$

The electric field produced by interference of the y-pair of incident beams is completely analogous with exchanged x- and y-coordinates. For the x- and y-polarized electric field E_x and E_y, respectively, one obtains

$$E_y = e^{i\frac{\Delta_x}{2}} \cos\left(k_x x + \frac{\Delta_x}{2}\right) \tag{3.31}$$

$$E_x = e^{i\frac{\Delta_y}{2}} \cos\left(k_y y + \frac{\Delta_y}{2}\right), \tag{3.32}$$

where scaling factors are neglected. Depending on the phase difference $\Delta_x - \Delta_y$ and on the position within the interference pattern, the total electrical field can be linearly or elliptically polarized. Two possible polarization states are shown schematically in Fig. 3.7.

Assuming that the beam's angle to the optical axis α_i are equivalent for both pairs of incident beams and using the generalized intensity definition $I \propto |\mathbf{E}|^2$ (which is consistent with fluorescence absorption, see section 3.2) one obtains

$$I(\mathbf{r}) = 2 + \cos(ux + \Delta_x) + \cos(uy + \Delta_y), \tag{3.33}$$

with $u = 4\pi\, n_{\text{glass}} \sin(\alpha_i)/\lambda$ and where scaling factors are neglected and where the identity $\cos^2(a) = \frac{1}{2}(1 + \cos(2a))$ is used. For isotropically distributed fluorophores, the fluorescence is proportional to the

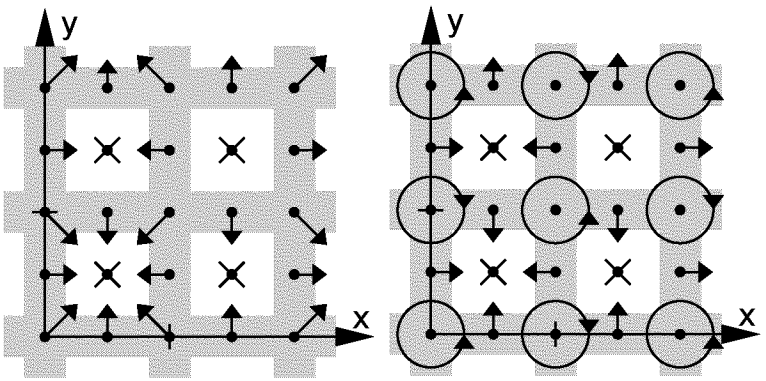

Figure 3.7: Two possible polarization states of the interference field. The coordinate system is displaced by $(-\Delta_x/2k_x)$ and $(-\Delta_y/2k_y)$ in x- and y-direction, respectively, to let the origin coincide with a point of maximum intensity. The grey bars illustrate the bright zones, the diagonal crosses indicate the nodes with vanishing electrical field. The left panel shows the electrical polarization vectors for phase offsets $\Delta_x = \Delta_y$. The polarization at every point is pure linear (indicated by arrows). The right panel illustrates the polarization for $\Delta_x = \Delta_y + \pi$. Depending on the position in the object plane, the polarization can be pure linear, pure circular (indicated by circles) or elliptical (between the two extremes, not shown).

generalized intensity as defined in section 3.2. Thus, for this case, Eq. 3.33 gives the spatial modulation of fluorescence introduced by the interference generating apparatus. However, for non-isotropically distributed fluorophores, the situation is different and Eq. 3.33 *does not necessarily* describe the fluorescence modulation adequately.

A second point worth mentioning is the resulting degree of polarization of the fluorescence light. This polarization can be neglected if

- the fluorophores destroy the polarization by thermal motion (see section 3.2.1) or
- the imaging properties of the microscope are not affected by the polarization.

Both conditions may not be true and, in those cases, the effective modulation function may be different from Eq. 3.33 even for isotropically distributed fluorophores.

Generalization for non-ideal interference geometry

Now, the description of intensity distribution in the object plane (Eq. 3.33) will be generalized to account for non-ideal experimental conditions.

The equations describing the x- and y-polarized electric field (Eq. 3.32 and Eq. 3.31, respectively) are based on the following idealizations:

1. The x- and y-pair of incident beams are assumed to be oriented in the x-z-plane and y-z-plane, respectively.

   Minor out-off-plane components of the incident beam's wave vectors lead to a slight rotation of the x- and y-polarized electric field distribution.[5]

2. The beam's angles α_i to the optical axis are equivalent for all incident beams.

   Different angles of the incident beams lead to a different spatial frequency of the dominantly x- and dominantly y-polarized electric field distribution.

[5] By this rotation, the polarizations are not longer exactly parallel to the x- and y-axis, respectively. To indicate this fact, the naming *dominantly* x- and *dominantly* y-polarized electric field distribution is used.

3. The field amplitudes of all four incident beams are equivalent.

   Differences in the amplitudes lead to a reduced modulation depth of the electric field distribution.

Considering the above described generalizations for the electric field distributions (Eq. 3.32 and Eq. 3.31 under ideal conditions), the resulting intensity distribution (Eq. 3.33 under ideal conditions) has to be modified in the following form:

$$I(\mathbf{r}) = 2 + M_x \cos(\mathbf{u}_x\mathbf{r} + \Delta_x) + M_y \cos(\mathbf{u}_y\mathbf{r} + \Delta_y), \tag{3.34}$$

where

$$\mathbf{u}_x = u_x \begin{pmatrix} \cos(\gamma_x) \\ \sin(\gamma_x) \end{pmatrix} \qquad \text{and} \tag{3.35}$$

$$\mathbf{u}_y = u_y \begin{pmatrix} -\sin(\gamma_y) \\ \cos(\gamma_y) \end{pmatrix} \tag{3.36}$$

with u_x, γ_x and M_x denoting the spatial frequency, rotational angle and modulation depth of the intensity distribution generated by the x- pair of incident beams, respectively, and with u_y, γ_y and M_y denoting the corresponding values for the y-pair (see Fig. 3.8 for a graphical illustration).[6] Eq. 3.34 with the appropriate values for $u_x, u_y, \gamma_x, \gamma_y, M_x, M_y$ is a very good approximation to the real intensity distribution in the experimental setup.

3.3.2 Image reconstruction

In this subsection the influence of the non-uniform excitation pattern on the image produced by the microscope will be studied and an

[6] In Eq. 3.34, it was implicitly assumed that the total intensity equals the sum of the squared moduli of the dominantly x-and dominantly y-polarized electric field distributions, i.e. it was assumed $|E_x + E_y|^2 = |E_x|^2 + |E_y|^2$. This relation holds for orthogonally polarized fields only, i.e. for $\gamma_x = \gamma_y$. It remains, however, a good approximation for the small rotational angles $\gamma_y \leq 1^\circ$ and $\gamma_y \leq 1^\circ$ caused by minor imperfections in the experimental setup.

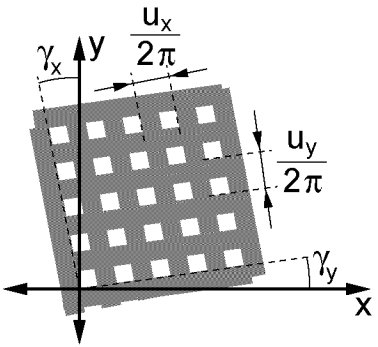

Figure 3.8: Schematic representation of the non-ideal intensity pattern produced by the interference generating apparatus.

algebraic approach for reconstruction of the specimen spectrum within an extended passband will be derived.

With $\tilde{}$ denoting the Fourier transform of a variable, one obtains the spectrum $\tilde{I}$ of the intensity pattern by calculating the Fourier transform of Eq. 3.34:

$$\tilde{I}(\mathbf{k}) = 8\pi^2\delta(\mathbf{k}) + 2\pi^2 M_x \left[e^{i\Delta_x}\delta(\mathbf{k}+\mathbf{u}_x) + e^{-i\Delta_x}\delta(\mathbf{k}-\mathbf{u}_x) \right] + 2\pi^2 M_y \left[e^{i\Delta_y}\delta(\mathbf{k}+\mathbf{u}_y) + e^{-i\Delta_y}\delta(\mathbf{k}-\mathbf{u}_y) \right], \tag{3.37}$$

where δ is Dirac's delta function (Eq. 12) and where the identity $\cos(a) = \frac{1}{2}(e^{ia} + e^{-ia})$ is used.

To simplify further calculations, the following scale-shift operators are introduced:

$$s_1(F(\mathbf{v})) := F(\mathbf{v}) \quad \text{is the identical mapping,} \tag{3.38}$$
$$s_2(F(\mathbf{v})) := M_x F(\mathbf{v} + \mathbf{u}_x), \tag{3.39}$$
$$s_3(F(\mathbf{v})) := M_x F(\mathbf{v} - \mathbf{u}_x), \tag{3.40}$$
$$s_4(F(\mathbf{v})) := M_y F(\mathbf{v} + \mathbf{u}_y), \quad \text{and} \tag{3.41}$$
$$s_5(F(\mathbf{v})) := M_y F(\mathbf{v} - \mathbf{u}_y). \tag{3.42}$$

The inverse scale-shift operators are given by

$$s_1^{-1} := s_1, \tag{3.43}$$
$$s_2^{-1}(F(\mathbf{v})) := \frac{1}{M_x} F(\mathbf{v} - \mathbf{u}_x), \tag{3.44}$$
$$s_3^{-1}(F(\mathbf{v})) := \frac{1}{M_x} F(\mathbf{v} + \mathbf{u}_x), \tag{3.45}$$
$$s_4^{-1}(F(\mathbf{v})) := \frac{1}{M_y} F(\mathbf{v} - \mathbf{u}_y), \quad \text{and} \tag{3.46}$$
$$s_5^{-1}(F(\mathbf{v})) := \frac{1}{M_y} F(\mathbf{v} + \mathbf{u}_y). \tag{3.47}$$

In frequency domain, the imaging property of the microscope is described as a multiplication of the fluorescence spectrum $\tilde{\phi}$ with the optical transfer function (OTF) T of the microscope (see section 3.1). Thus, one obtains for the spectrum $\tilde{\theta}$ of the image produced by the microscope

$$\tilde{\theta} = T\tilde{\phi} \tag{3.48}$$
$$\overset{\text{Eq. 3.15}}{=} T(\widetilde{\psi I}) \tag{3.49}$$
$$\overset{\text{Eq. 8}}{=} T \ll \tilde{\psi}, \tilde{I} \gg$$
$$= T\Big[4s_1(\tilde{\psi}) + e^{i\Delta_x} s_2(\tilde{\psi}) + e^{-i\Delta_x} s_3(\tilde{\psi}) + e^{i\Delta_y} s_4(\tilde{\psi}) + e^{-i\Delta_y} s_5(\tilde{\psi})\Big], \tag{3.50}$$

where $\ll\gg$ denotes the convolution operation and where scaling factors are neglected.

Experimentally, five images θ_j are recorded for which the x- and y-phase offsets are set to different values by piezo-actuators. In the setup, the pair (Δ_x, Δ_y) is sequentially set to $(0,0)$, $(\pi/2,0)$, $(\pi,0)$, $(0,\pi/2)$ and $(0,\pi)$. Eq. 3.48 holds for each of the acquired images with the appropriate coefficients $e^{\pm i\Delta_x}$ and $e^{\pm i\Delta_y}$, thus resulting in a 5×5 set of linear equations:

$$\begin{pmatrix} \tilde{\theta}_1 \\ \tilde{\theta}_2 \\ \tilde{\theta}_3 \\ \tilde{\theta}_4 \\ \tilde{\theta}_5 \end{pmatrix} = T \overbrace{\begin{pmatrix} 4 & 1 & 1 & 1 & 1 \\ 4 & i & -i & 1 & 1 \\ 4 & -1 & -1 & 1 & 1 \\ 4 & 1 & 1 & i & -i \\ 4 & 1 & 1 & -1 & -1 \end{pmatrix}}^{=:M} \begin{pmatrix} s_1(\tilde{\psi}) \\ s_2(\tilde{\psi}) \\ s_3(\tilde{\psi}) \\ s_4(\tilde{\psi}) \\ s_5(\tilde{\psi}) \end{pmatrix} \tag{3.51}$$

The components $s_j(\tilde{\psi})$ can be calculated by inversion of matrix M:

$$\begin{aligned} \begin{pmatrix} s_1(\tilde{\psi}) \\ s_2(\tilde{\psi}) \\ s_3(\tilde{\psi}) \\ s_4(\tilde{\psi}) \\ s_5(\tilde{\psi}) \end{pmatrix} &= \frac{1}{T} M^{-1} \begin{pmatrix} \tilde{\theta}_1 \\ \tilde{\theta}_2 \\ \tilde{\theta}_3 \\ \tilde{\theta}_4 \\ \tilde{\theta}_5 \end{pmatrix} \\ &= \frac{1}{T} \begin{pmatrix} 0 & 0 & \frac{1}{4} & 0 & \frac{1}{4} \\ \frac{1+i}{4} & \frac{-i}{2} & \frac{-1+i}{4} & 0 & 0 \\ \frac{1-i}{4} & \frac{i}{2} & \frac{-1-i}{4} & 0 & 0 \\ \frac{1+i}{4} & 0 & 0 & \frac{-i}{2} & \frac{-1+i}{4} \\ \frac{1-i}{4} & 0 & 0 & \frac{i}{2} & \frac{-1-i}{4} \end{pmatrix} \begin{pmatrix} \tilde{\theta}_1 \\ \tilde{\theta}_2 \\ \tilde{\theta}_3 \\ \tilde{\theta}_4 \\ \tilde{\theta}_5 \end{pmatrix} \end{aligned} \tag{3.52}$$

In each row of Eq. 3.52, the original spectrum $\tilde{\psi}$ can be calculated from components $s_j(\tilde{\psi})$ by shifting it in the opposite direction (i.e.

multiplication with the inverse shift operator s_j^{-1}) and by rescaling with the inverse OTF:

$$\tilde{\psi} = s_j^{-1}\left(\frac{\left(M^{-1}\tilde{\boldsymbol{\theta}}\right)_j}{T}\right) \qquad 1 \leq j \leq 5, \tag{3.53}$$

where $\tilde{\boldsymbol{\theta}}$ is a notation for the vector consisting of components $\tilde{\theta}_1 ... \tilde{\theta}_5$ and where the subscript j of a vector denotes its j-th component. These five equations for indices $j = 1...5$ are the basic relations to reconstruct the original spectrum from the measured images.

For a certain index j, Eq. 3.53 can be evaluated only for those points in frequency domain where $s_j^{-1}(T(k_x, k_y)) \neq 0$, called the domain of definition of Eq. 3.53 for index j. For an ideal fluorescence microscope, the support of the OTF, T, is a circular region with a radius k_c where $k_c = 4\pi \mathrm{NA}/\lambda$, NA is the numerical aperture of the microscope and λ the emission wavelength (see section 3.1). Recalling Eq. 3.43 to Eq. 3.47, the domains of definition for the particular indices $j = 1...5$ can be determined. For instance, for $j = 1$ the domain of definition equals the circular passband of conventional fluorescence microscopy as the shift operator s_1^{-1} is the identical mapping. In contrast, for $j = 2$ a different circular region is obtained as s_2^{-1} shifts along the k_x-axis in positive direction. The resulting passband for HELM is the total of the domains of definition for the indices $j = 1...5$. The resulting clover leaf shaped passband is shown in Fig. 3.9.

3.3.3 OTF design

In the overlap regions of the circles 1...5 in Fig. 3.9, the original spectrum can be calculated from the measured images by evaluating Eq. 3.53 for more than one index j. To achieve a high signal-to-noise ratio of the final image, the results obtained by evaluating Eq. 3.53 for different indices should be weighted according to their respective noise level. As noise is amplified by the inverse of the denominator

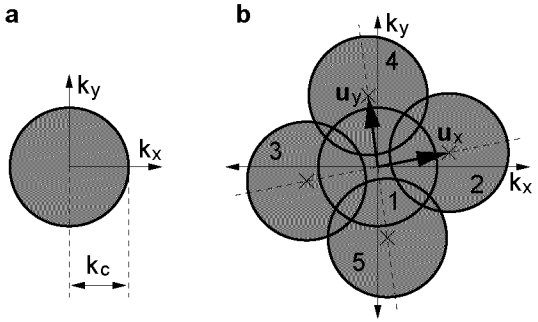

Figure 3.9: The passband enhancement achieved by HELM. (**a**) shows the circular passband for standard fluorescence microscopy with cut-off frequency k_c. (**b**) shows the extended passband of HELM. The object information can be reconstructed within the five circular regions 1...5 by applying Eq. 3.53 with the corresponding index j. The displacements $\mathbf{u}_x$ and $\mathbf{u}_y$ are equal to the spatial frequencies of the harmonic excitation pattern (see Fig. 3.8).

in Eq. 3.53, the weights w_j are set to the value of the denominator, i.e. $w_j = s_j^{-1}(T(k_x, k_y))$. By using these weights w_j, the following expression $\tilde{\psi}_{\text{est}}$ to estimate of the original spectrum within the clover leaf shaped passband for HELM is obtained:

$$\tilde{\psi}_{\text{est}} = \sum_{j=1}^{5} w_j s_j^{-1} \left(\frac{\left(M^{-1}\tilde{\boldsymbol{\theta}}\right)_j}{T} \right) = \frac{\sum_{j=1}^{5} s_j^{-1} \left(\left(M^{-1}\tilde{\boldsymbol{\theta}}\right)_j \right)}{\sum_{j=1}^{5} s_j^{-1}(T)} \tag{3.54}$$

To calculate the spectrum of the final image in HELM, two additional modifications to Eq. 3.54 are introduced. First, the maximum noise amplification when the denominator $\sum_{j=1}^{5} s_j^{-1}(T)$ tends to zero

(i.e. at the boundary of the passband for HELM) has to be limited. Secondly, to reduce the ripple in the final image, the Fourier spectra are apodized by an appropriate function $T_{\mathrm{H}}(k_x, k_y)$. Taking into account the above modifications, the final equation for reconstruction of the spectrum $\tilde{\psi}_{\mathrm{H}}$ of the HELM image is obtained:

$$\tilde{\psi}_{\mathrm{H}} = \min \left(\frac{T_{\mathrm{H}}(k_x, k_y)}{\sum_{j=1}^{5} s_j^{-1}(T)}, \gamma \right) \sum_{j=1}^{5} s_j^{-1} \left(\left(M^{-1} \underline{\tilde{\theta}} \right)_j \right) \tag{3.55}$$

The limiter γ is chosen according to the total noise level of the acquired images which is influenced by shot noise, temperature dependent dark current noise, noise of the analog circuits in camera and frame grabber and, finally, quantization noise of the analog-to-digital converter. For the system used (uncooled camera, 8-bit quantization) values between 20 and 50 yield good results for the measured samples. Except for the outermost region of the passband where the γ-limitation sets in, T_{H} equals the resulting optical transfer function for HELM.

The influence of the apodisation function T_{H} on the resulting point spread function (PSF) is studied numerically. Fig. 3.10**a** and Fig. 3.10**b** show the situation for the simple case of a constant OTF $T_{\mathrm{H}} = 1$ and $\gamma = 20$. It can be seen, that the PSF has strong side lobes, most noticeable is the negative overshoot of about 26% in the diagonal directions. Taking into account the fact that such overshoots originating from different point sources could interfere constructively, this level is hardly acceptable. As is well known from basic Fourier transform properties, the side lobes can be reduced by smoothly reducing the value of T_{H} towards the cut-off frequency. Fig. 3.10**c** shows the OTF finally used for the HELM images. [7] With T_{H} chosen that way, the

[7] The equation for setting T_{H} within the clover leaf shaped passband (see Fig. 2.2 on page 10) is

$$T_{\mathrm{H}}(k_x, k_y) = 1 - \left(\frac{|\mathbf{k}|}{k_m} + \frac{|\mathbf{k}|^2}{b^2} - \frac{|\mathbf{k}|^2}{b k_m} \right)^2, \tag{3.56}$$

negative overshoot is reduced to about 13% while the width of the PSF is largely preserved.

As can be seen in Fig. 3.9, the PSF for HELM is not isotropic. This is a consequence of the anisotropy of the interference pattern leading to a non circularly-symmetric OTF. Experimentally, this anisotropy could largely be avoided by employing six or eight laser beams oriented in multiples of 60° or 45°, respectively.

Another interesting approach to reduce the anisotropy without the need for experimental add-ons would be the application of band extrapolation algorithms to the HELM images [2, 19]. With such algorithms, the reconstruction of some missing parts of the object spectrum is possible by taking into account a priori knowledge about the sample such as non-negativity of the intensity distribution. Applied to HELM, the computational reconstruction of the object information within the missing regions in the diagonal directions in frequency domain could potentially yield an more isotropic point spread function.

---

where

$$k_m = u + k_c \tag{3.57}$$

is the maximum cut-off frequency and where

$$b = \sqrt{k_c^2 + u^2 - 2u\left(\frac{p}{2} - \sqrt{\frac{p^2}{4} - q}\right)} \tag{3.58}$$

with

$$p = \frac{2u(k_y/k_x)^2}{1 + (k_y/k_x)^2} \qquad \text{and with} \tag{3.59}$$

$$q = \frac{u^2(k_y/k_x)^2 - k_c^2}{1 + (k_y/k_x)^2} \tag{3.60}$$

is the cut-off frequency in direction of $\mathbf{k}$. Eq. 3.59 and 3.60 apply to one half quadrant only, i.e. for $k_y \geq 0$ and $k_x > k_y$. For reciprocal space points which do not fulfill this condition, the mirror symmetry of T_{H} at the k_x- and k_y-axis and at the diagonal axes must be employed, i.e. the appropriate transformations $k_x \leftrightarrow -k_x$, $k_y \leftrightarrow -k_y$ and $k_x \leftrightarrow k_y$ must be performed befor applying Eq. 3.56.

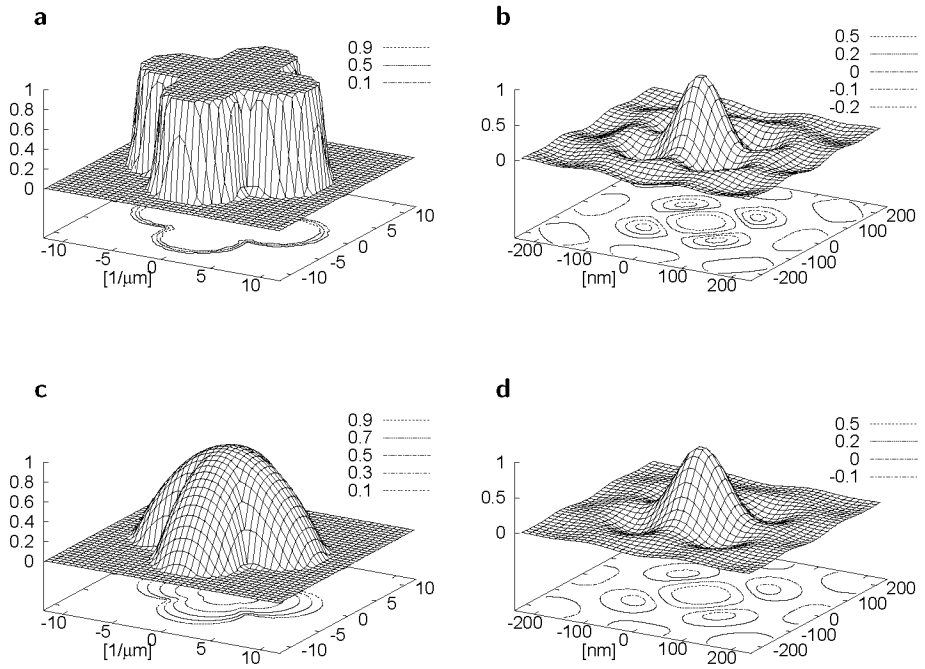

Figure 3.10: Optical transfer functions for HELM (left) and corresponding point spread functions (right) for two different apodisation functions T_{H}. (**a**) and (**b**) show the situation for a constant apodisation $T_{\mathsf{H}}(k_x, k_y) = 1$ and $\gamma = 20$, (**c**) and (**d**) for a smoother apodisation function (Eq. 3.56) and also $\gamma = 20$.

Chapter 4

The HELM setup

In this chapter, the setup which is used to achieve resolution enhancement in HELM is described.

The basic goal of the setup is the generation of a two-dimensional mesh-like interference pattern in the object plane of the microscope. As has already been mentioned (see chapter 2), this pattern is the result of interference of four mutually coherent laser beams which cross in the object plane of the microscope.

4.1 General considerations

One essential requirement for the HELM setup is that standard sample preparations should be usable. Standard sample preparations consist of a slide (size typically 75 mm $\times$ 25 mm $\times$ 1 mm) and a thin cover slip which form the specimen chamber. Basically, two possibilities exist to couple the laser beams to the specimen chamber:

1. The laser beams are coupled through the objective (see Fig. 4.1). This arrangement is rather elegant as it partly employs the same optics for imaging and for illumination. No problems arise

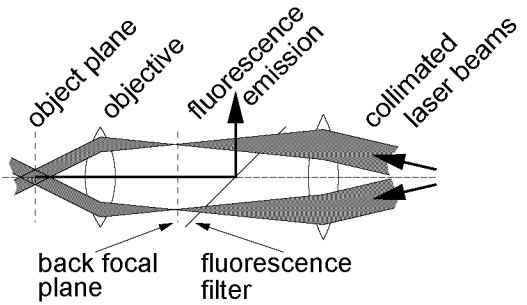

Figure 4.1: Simplified optical train for generation of an interference pattern by illuminating through the objective. For simplicity, only two beams are shown. The collimated beams are focused by a lens to form a focal spot in the back focal plane of the microscope.

with the translation stage or with the condenser used for trans-illumination. A drawback of this arrangement is the fact that the coupling unit would be strongly connected to one particular type of microscope as the unit's design would be influenced by optical parameters as focal distance of the objective, type of objective (infinity corrected or not) and, last but not least, the available ports of the microscope.

2. The laser beams are coupled to the specimen chamber from the backside through the slide. One fundamental difference of such an arrangement is the fact that the direct laser light travels in the same direction as the fluorescence light. This allows one to record the interference pattern by removing the fluorescence filter from the imaging path of the microscope. This is advantageous as geometric parameters of the pattern can be easily obtained from these non-fluorescence images. On the other hand, the residual laser light which passes the fluorescence filter could potentially deteriorate the fluorescence image. This draw-

back, however, turned out to be negligible, probably due to the high attenuation ratio of the fluorescence filter for the strictly monochromatic laser light. Last but not least, a setup using the backside-arrangement can be realized remarkably simpler. One reason for that is that a plane parallel arrangement for the beam splitting unit can be used.

Taking into account the *pros* and *cons* of the two arrangements, a decision for the backside arrangement was made. By an elegant design, the translation stage with little modifications is still usable and trans-illumination images are still possible with a long distance condenser.[1] Advantageous is the fact, that the setup is not closely tied to one particular type of microscope. It can be used on an inverted microscope (the normal case) and even with an upright one (with an appropriate translation stage).

4.2 The beam splitting unit

The beam splitting unit serves to generate four coherent laser beams of equal intensity that interfere in the object plane of the microscope. The arrangement used is shown in Fig. 4.2. An Ar-ion laser (Omnichrome 543-AP-A01, wavelength 488 nm, power 120 mW) serves as a coherent light source. It is coupled to the beam splitting unit by an optical single-mode fiber with integrated pigtail-style fiber couplers.

A rotatable $\lambda/2$-wave-plate and a polarizer serve for setting the incident laser power. Three non-polarizing beam splitters with a splitting ratio of 1:1 produce four laser beams of equal intensity. Because the path lengths of the four beams are equivalent (at least to a few millimeters caused by production imperfections), the crossing beams are mutually coherent as long as the coherence length of the laser exceeds a few millimeters. The coherence length of the used Ar-ion

[1] Trans-illumination is used for rough orientation only and, hence, the lower resolution achievable with long distance condensers poses no problem.

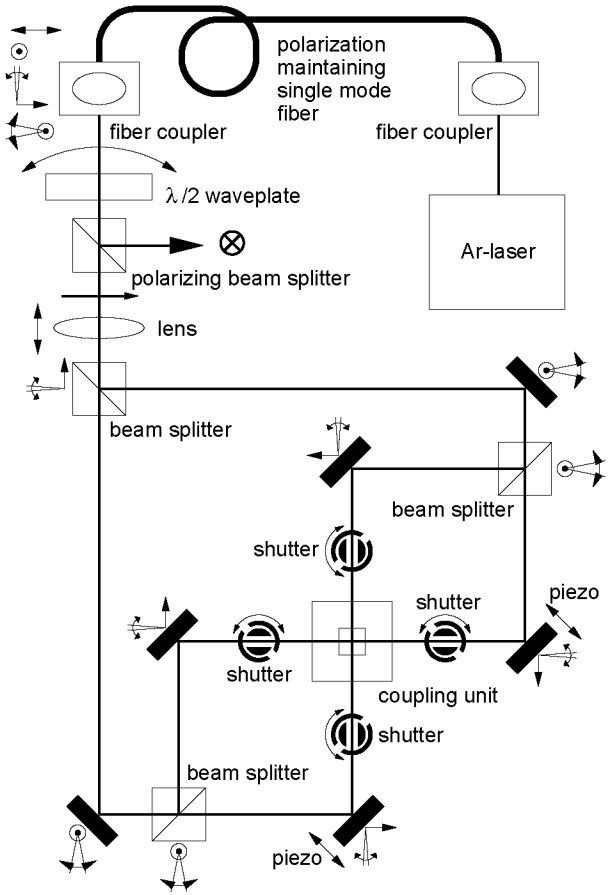

Figure 4.2: Optical train of the beam splitting unit. The symbols ⟷ and ⊙ denote translatory degrees of freedom within and perpendicular to the paper plane, respectively. The symbols and denote rotational degrees of freedom around axes parallel and perpendicular to the paper plane, respectively.

laser is specified to be 300 mm and, consequently, well within the acceptable range.

The path length for two beams can be slightly varied by piezo-actuated mirrors to move the excitation pattern relative to the specimen. Four shutters are provided to block one or more laser beams. These shutters are helpful for aligning the four beams to cross at the optical axis in the object plane.

During the work with the HELM setup, the idea of using the mesh-like interference pattern for optical trapping of sub-micrometer sized particles arose. First results of such an optical interference trap are presented in appendix A.

4.2.1 Illumination spot size

The beam diameter at the output of the collimating fiber coupler is 1.5 mm, a weak lens (focal length $f = 300$ mm) is used to slightly focus the laser beam. Gaussian beam optics [68] predict a beam waist diameter w_f of

$$w_f = 4\frac{f\lambda}{\pi w_0} = 125\mu\text{m}, \tag{4.1}$$

where λ is the wavelength of light and w_0 is the beam waist diameter of the incident beam.[2] The experimental value (roughly 140 μm, see Fig. 4.3) is close to the theoretical expectation. This rather large spot size ensures uniform sample illumination within the field of view. The extent of the field of view for the employed 63× NA 1.4 objective, for the given pixel distance of 8.3 μm on CCD-chip and for the processed image size of 512 × 512 pixels amounts to 25 μm × 25μm or 40 μm × 40 μm for an intermediate magnification of 2.5 or 1.6, respectively.

[2] Eq. 4.1 strictly holds only if the primary beam waist coincides with the focal plane of the lens. However, for the large primary beam waist diameter (1.5 mm) it is a good approximation as long as the distance between primary beam waist and focal plane does not exceed a few meters.

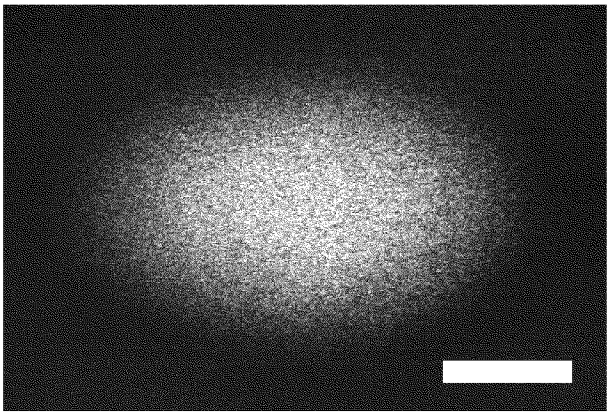

Figure 4.3: Image of the illumination ellipsis produced by one beam (three beams are blocked by shutters). A scattering sample of statistically distributed polystyrene beads with a diameter of 200 nm is imaged with an 10× NA 0.2 objective. The lens (see Fig. 4.2) is set to a position where the spot diameter is minimal. Scale bar is 100 μm.

It can be shown that, for this geometry, the curvature of the wavefronts is negligible in the field of view even when there is a distance of a few centimeters between the object plane and the secondary beam waist. Therefore, displacements of the lens can be used to extend the spot size.

4.2.2 The piezo actuator

In HELM, the phase offset of the interference pattern is sequentially set to five different values. During acquisition of one image it is crucial that the phase offset is constant. For this reason, the well-known creeping of common piezoelectric actuators causes problems.

An alternative to piezoelectric actuators are electrostrictive ones. The physical difference between the two is that piezoelectric actuators are remanently polarized during manufacturing (and, consequently, must be operated below the Curie temperature to maintain polarization) while electrostrictive ones are not remanently polarized and are operated slightly above the Curie temperature. From a practical point of view, there are four key differences:

1. The mechanical response to an applied voltage is approximately linear for piezoelectric actuators while it is a quadratic function for electrostrictive ones.

2. Hysteresis and creep are strongly reduced for electrostrictive actuation in relation to piezoelectric one.

3. The mechanical extension for an applied voltage is more temperature dependent for electrostrictive actuators.

4. The electrical capacity of electrostrictive actuators is increased by a factor between five and ten in relation to piezoelectric ones. This potentially poses a problem with common high voltage amplifiers, as these are not designed for such strong capacitive loads.

As the linearity of the actuator as well as the temperature independence is of minor impact for HELM, electrostrictive piezo actuators are well suited for the demands. Finally, electrostrictive stack actuators (XIRE 0710L, XINETICS Inc., Devens MA, USA) were chosen. They are operated with a self-made high voltage amplifier designed for the high capacitive load (approx. 9,2 μF). The measured curve (Fig. 4.4) confirms the expectation about the actuator characteristic. The hysteresis is 1% which is about one tenth of a typical value for piezoelectric actuators.

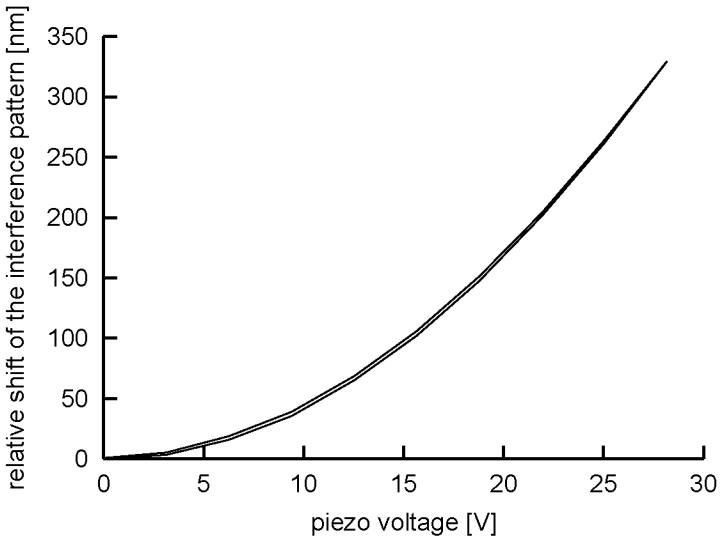

Figure 4.4: The measured actuator characteristic. The position of the interference pattern is plotted against the applied voltage. The trajectory shown is the response to a triangular control voltage.

4.2.3 The coupling unit

As has been mentioned in the beginning of this chapter, the laser beams are coupled to the specimen chamber from the backside through the slide. To achieve this, the four plane parallel laser beams produced by the beam splitting unit undergo total internal reflection (TIR) at the hypotenuses of four custom-made glass prisms which are oil-immersed to the slide (Fig. 4.5). The design of these prisms determines the beam's angle α to the optical axis and, as a result, the nodal spacing of the interference pattern. α is set to 55° in the current setup allowing one to directly observe of the laser light through a high NA oil-immersion objective (see section 5.1.1 for a discussion of this choice).

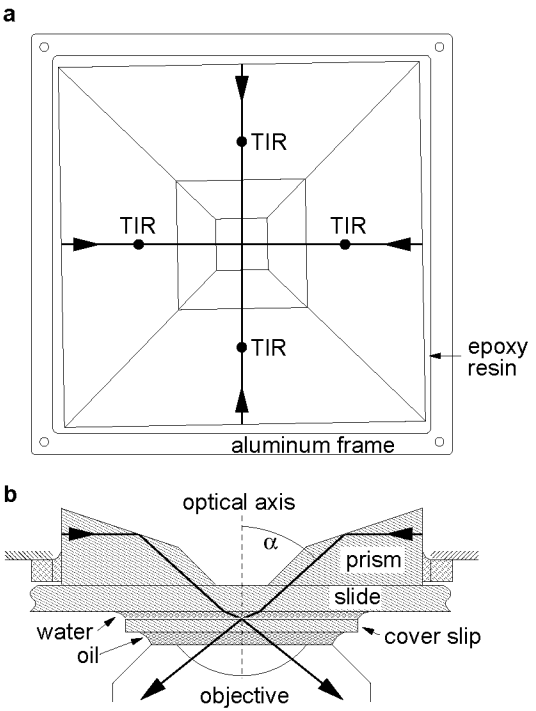

Figure 4.5: The coupling unit. (**a**) top view, (**b**) cut view. Four glass prisms are glued together to couple the laser beams to the sample. By TIR at the hypotenuses of the prisms, the beams are "bent" out of a plane parallel to the object plane. The prism block is slightly rotated (approx. 0.2°, shown exagerated for clarity) to avoid power fluctuations caused by laser light which is back-reflected into the laser cavity.

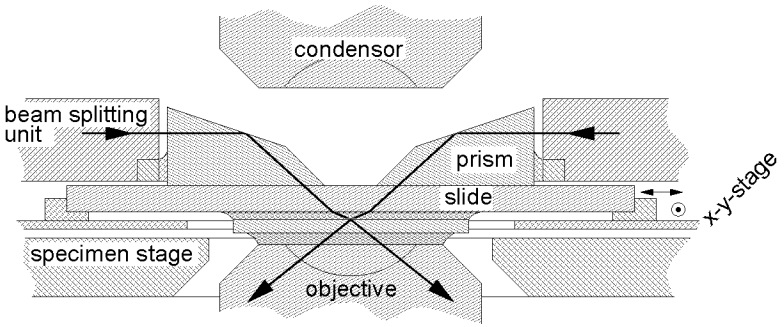

Figure 4.6: Cut view along the optical axis showing how the sample is moved between the microscope desk and the interference generating apparatus.

The assembly of the four prisms in Fig. 4.5 (referred to herein as coupling unit) together with the beam splitting unit form the interference generating apparatus. The coupling unit can be attached to the beam splitting unit as shown in Fig. 4.5 and Fig. 4.6 (for use with inverted microscopes) or it can be rotated by 180° around a lateral axis to fit on upright microscopes. When using an inverted microscope, the x-y-translation stage can be used; only the clamp mechanism for the slide must be replaced. Fig. 4.6 illustrates how the slide is moved in the air gap between the upper edge of the specimen stage and the lower edge of the interference generating apparatus (the gap is approx. 4 mm).

4.3 The overall system

The interference generating apparatus is mounted on an inverted microscope (Zeiss Axiovert 100, see Fig. 4.7). The used camera is

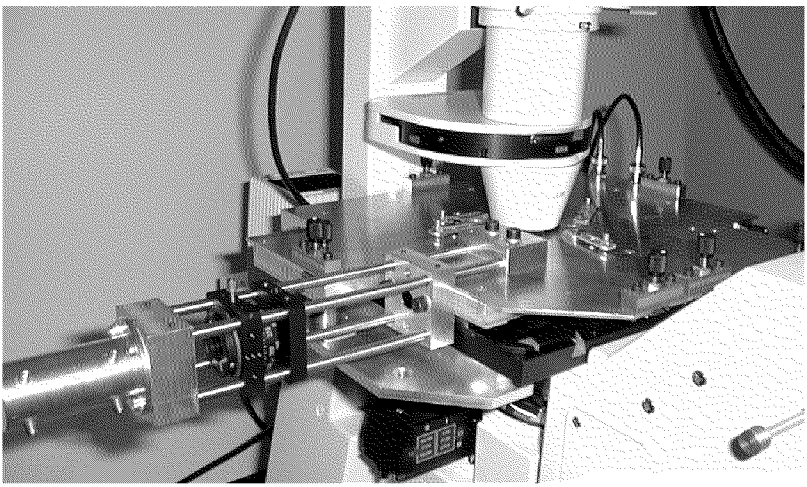

Figure 4.7: Photography of the interference generating apparatus mounted on an inverted Zeiss Axiovert 100 microscope.

an uncooled industrial grade CCD-camera (LV-8500, Leutron Vision, Glattbrugg, Switzerland) which is connected to the bottom port of the microscope to minimize image deterioration caused by imperfect optical components in the standard folded paths. A standard personal computer is used to read out image data, control the measurement sequence and perform image calculations. The computer is equipped with a frame grabber allowing pixel-synchronous image acquisition (Pic-Port, Leutron Vision, Glattbrugg, Switzerland) and with an analog input-output card (ADIODA-12, MESSCOMP GmbH, Wasserburg, Germany). A dedicated real-time operating system is not required for measurement control; the computer runs under MS WINDOWS NT 4.0. The software (the one for measurement control as well as that one for image reconstruction) is programmed in C++ using the BORLAND C++-Builder 4.0. The choice of C++ as programming

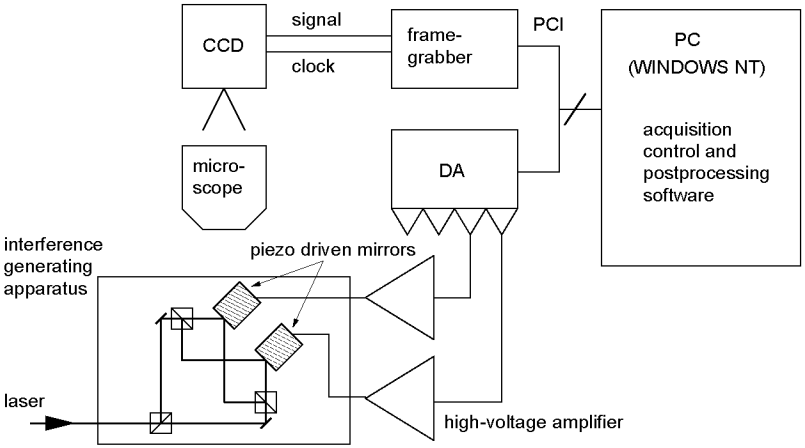

Figure 4.8: Schematic of the HELM system.

language and the realization of the image reconstruction algorithm as command line program ensure easy portability to different platforms. An overview of the system is shown in Fig. 4.8.

4.4 System stability

The measured interference pattern is shown in Fig. 4.9. One point of practical interest is the stability of the interference pattern. To avoid expensive materials like INVAR, the interference generating apparatus mainly consists of aluminum parts which have a rather large thermal coefficient of extension. To nevertheless bring thermal drift into an acceptable range, a very compact design was chosen for the interference generating apparatus. Experimentally, the thermal drift of the pattern has been determined to be typically 20 nm/min for a system in thermal equilibrium with the environment. As phase offset

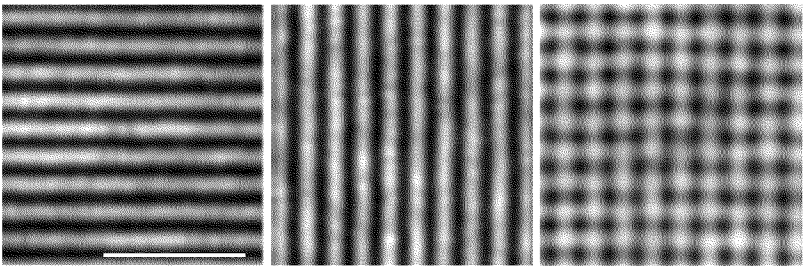

Figure 4.9: Resulting intensity patterns for interference of the y-pair of incident beams (left; the x-pair is blocked by shutters), for interference of the x-pair (mid; the y-pair is blocked) and for interference of all four beams (right). Scale bar is 1 μm.

errors of one tenth of the nodal spacing (20 nm) turned out to be just tolerable, thermal drift limits the acquisition time to a few tens of seconds. For the uncooled CCD-camera, this imposes no additional limit since the dark current does not allow longer exposure times. However, for cooled cameras it could become a restriction. In this case the limitation could be easily overcome by recalibrating the phase offset during a long term measurement or using advanced materials like INVAR.

Chapter 5

Results

5.1 Achievable resolution by HELM

As test objects for the achieved resolution of the HELM device, commercially available fluorescent polystyrene beads with a diameter of 100 nm were used. For closely packed beads, the center-to-center distance is far below the Rayleigh limit for standard fluorescence microscopy (240 nm for a NA=1.4 objective and green light) and also below that one of confocal devices. To stabilize the structures, the carboxylate-modified surface of the beads (Fluoresbrite YG carboxylate microspheres, Polysciences Inc., Warrington PA) was linked to the cover slip with polylysine (poly-L-lysine hydrobromide, MW 36 kDa, Sigma, Buchs, Switzerland).

To compare the resolving power of different techniques, the same region of H_2O immersed beads was imaged using HELM (Fig. 5.1a), standard illumination (Fig. 5.1b), and confocal scanning (Fig. 5.1c).[1]

[1] A short note to pixelation and printing resolution of all light microscopic images in this thesis: The pixel distance of the acquired images was chosen to comply with the Shannon criterion. The quasi-continuous images printed were generated by band-limited interpolation to one quarter of the original pixel size

As a reference for the actual locations of the individual beads, an atomic force microscope image is also given (Fig. 5.1d) which was acquired in air.

The resolution of the HELM image is clearly superior to that of the standard and also to that of the confocal image. Distinguishing individual beads is not possible in the latter ones but is possible in HELM, although for HELM resolving 100-nm beads is close to the limit. Fig. 5.2 illustrates the achieved resolution gain in Fourier space.

Fig. 5.3 shows beads with a diameter of 200 nm which approximately equals the Rayleigh limit for standard fluorescence microscopy. The HELM image Fig. 5.3a demonstrates that such beads can be clearly distinguished by HELM, even when they are closely packed. In the standard fluorescence microscopy image Fig. 5.3b, in contrast, the individual beads remain blurred (see also Fig. 2.3 on page 11).

5.1.1 Discussion

Choosing the spatial frequency of excitation

One important parameter in HELM is the beam's angle α_i to the optical axis (Fig. 4.5) which determines the spatial frequency of excitation. The choice of α_i requires trading of maximum cut-off frequency (see Fig. 3.9 on page 37) vs. anisotropy of the resulting passband and vs. unwanted decrease of excitation intensity in the focal plane (see Tab. 3.1 on page 28). The chosen value (55° leading to a mesh spacing of 195 nm) is a good compromise and, additionally, allows one to directly observe the interference pattern with oil-immersion objectives.

Due to the non-isotropic passband, the images of the beads show some anisotropy and an overshooting near the edges of the beads, most noticeable are the dark zones in the diagonal directions in Fig. 5.1a. The experimental observation is in good agreement with the

with subsequent bicubic interpolation to the required printing resolution. This interpolation procedure smoothes the pixel noise of the original images and is the reason for the granular structure of e.g. Fig. 5.1c.

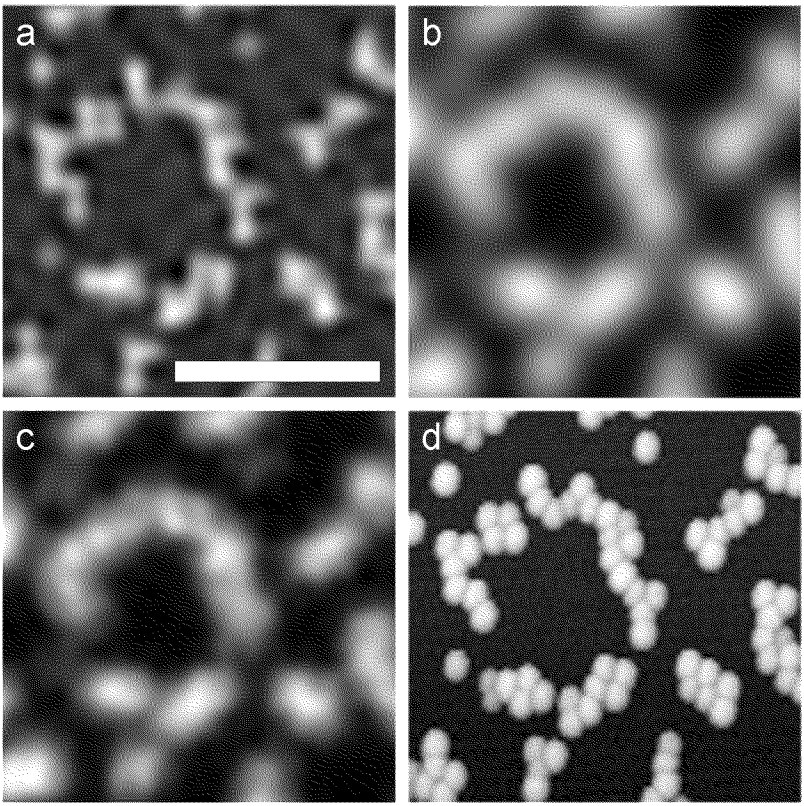

Figure 5.1: Identical area of a sample of 100 nm diameter fluorescent polystyrene beads imaged with different techniques. Scale-bar length is 1 μm. (a) was imaged using HELM on a Zeiss Axiovert microscope with a Plan Apo 63$\times$ NA1.4 objective. (b) was imaged through identical lenses using standard illumination. The confocal image (c) was recorded on a Leica NTSP using a Leica Plan Apo 100$\times$ NA1.4 objective. The pinhole diameter was set to 67% of the inner Airy-disk diameter, the resolution deterioration due to this finite pinhole size is about 15% [69]. (d) was recorded with an atomic force microscope (Topometrix Accurex II MS).

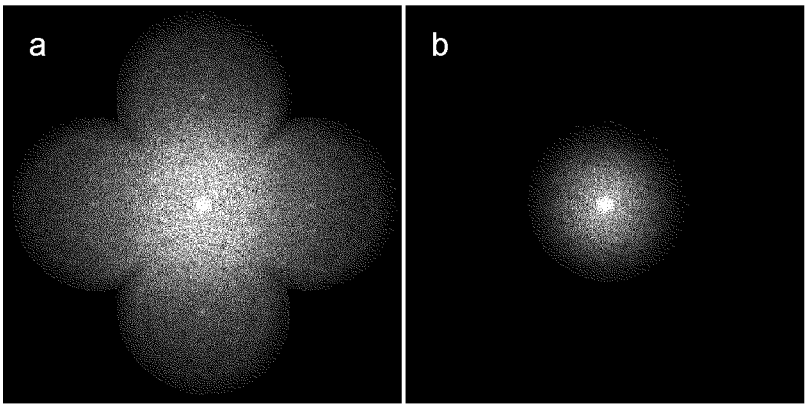

Figure 5.2: The Fourier transforms of the HELM image Fig. 5.1a and of the standard image Fig. 5.1b. Shown is the modulus of the complex Fourier transform in a logarithmic scale.

theoretically predicted point spread function given in Fig. 3.10d on page 40.

A more isotropic resolution together with a high cut-off frequency is achievable by employing more than four laser beams oriented along various orientations. This has been shown experimentally in a very recent work [35] for a somewhat different setup. Here, harmonic excitation patterns at 0°, 120° and 240° are produced sequentially by a rotatable phase grating. As expected, the point spread function is almost isotropic at the expense of one additional mechanical degree of freedom and a higher acquisition time.

A further resolution enhancement is possible by increasing α_i to values leading to TIR at the glass-water boundary around the specimen chamber [20]. However, the evanescent illumination restricts the approach to thin specimens and does not allow one three-dimensional

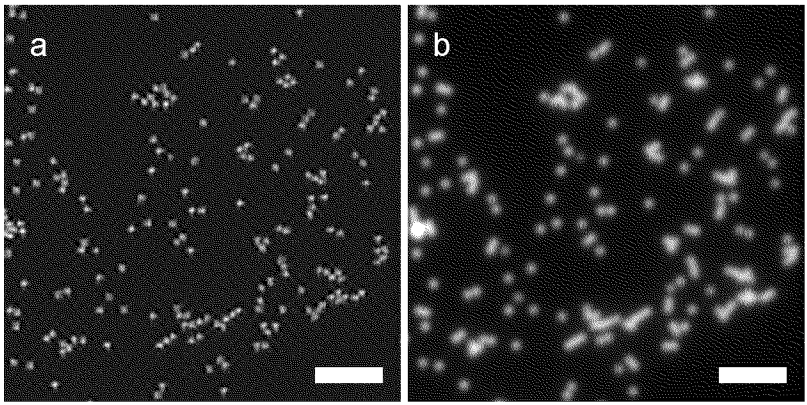

Figure 5.3: Fluorescent beads with a diameter of 200 nm imaged with HELM (a) and standard fluorescence microscopy (b). Scale-bar length is 2 μm. The microscope system as well as the specimen preparation are identical to the ones in Fig. 5.1a and 5.1b, respectively.

imaging which is expected to be a crucial area of application for future HELM devices (see chapter 6).

Signal-to-noise ratio and imaging speed in relation to confocal microscopy

In scanning confocal fluorescence microscopy (CFM), a diffraction limited light spot is scanned across the specimen and the fluorescence light emitted by the specimen is collected using the same objective. By means of a pinhole in a secondary image plane, the resolving power of CFM is increased by a factor of 1.5 for an infinitesimally small pinhole [69, 85, 78]. Unfortunately, this pinhole necessitates trading off noise level vs. resolution. Conversely, in HELM all photons entering the lenses can be collected by the camera.

Regarding the experimental data, it is striking that the signal-to-

noise ratio (SNR) of the HELM image Fig. 5.1a is superior to that one of the confocal image Fig. 5.1c even though the total time integrated laser power was 0.16 mWs and 32 mWs, respectively.[2] One reason for the reduced SNR of the confocal image is the above described photon-blocking pinhole. Another very fundamental effect increasing the noise and limiting the imaging speed in CFM is dye saturation (see subsection 3.2.2). Due to the finite lifetime of the excited state, the maximum emission rate of the fluorophores is limited. In HELM, roughly one half of the fluorophores are illuminated by the interference pattern at one time, whereas in the common single-point CFM this applies to only a tiny fraction of the fluorophores (approx. one per million for a 1024×1024 pixel image). As a consequence, the total photon flux from the specimen is limited to values that are several orders of magnitude smaller for the sequential operation of CFM than for the parallel one of HELM. Since the SNR is proportional to the square root of the number of acquired photons, a higher photon flux allows one to increase SNR or to speed up image acquisition (or a combination of both).

A rough estimation illustrates that dye saturation actually occurs in CFM even for moderate laser powers: The intensity in the focal spot I_{spot} of the CFM used in Fig. 5.1 is roughly

$$I_{\text{spot}} = \frac{\text{laser power}}{\text{spot area}} = \frac{5\text{mW}}{\pi\ 100\text{nm} \times 100\text{nm}} = 1.6 \times 10^{11} \frac{\text{W}}{\text{m}^2}. \quad (5.1)$$

This value is one or two orders of magnitude above the saturating intensity of typical fluorophores (see subsection 3.2.2). Therefore, dye saturation is assumed to be one reason for the striking SNR difference between Fig. 5.1a and Fig. 5.1c even though the saturating intensity

[2] Confocal image: Laser power in object plane 5 mW (manufacturer specification), acquisition time 6.5 s, size 25 μm × 25 μm. HELM image: Laser power 4 mW out of polarizing beam splitter, acquisition time 1.6 s, image size 25 μm × 25 μm, geometric spot size 140 μm × 140 μm × 1/cos(55°). ⇒ Laser energy in field of view: 0.12 mWs. Assuming 25% security factor to account for errors in spot size measurement: 0.16 mWs.

of the particular fluorophore embedded in the beads is not known.

Concerning high speed imaging, HELM also reduces the problems linked to mechanical scanning mechanisms as only five scans per image are performed in contrast to CFM, where one scan per line is required. Both the dye saturation problem and the mechanical scanning difficulties of CFM, however, can be reduced by the newer multi-point scanners [47, 86].

The advantages in the field of imaging speed can also be seen in the experimental data. The total acquisition time for the five images required for HELM in Fig. 5.1a was 1.6 s compared to 6.5 s for the confocal image Fig. 5.1c. Taking into account the higher signal-to-noise ratio of the HELM image which is achieved with an uncooled industrial grade CCD camera, this is a clear difference.

5.2 Measuring biological samples

HELM was used with various biological samples.[3] Fig. 5.4 to Fig. 5.7 show different polymer embedded rat tissues. Similar specimen preparation methods are employed routinely for diagnostic purposes as presence and localization of e.g. hormones can be studied by appropriate staining. Fig. 5.8 and Fig. 5.9 show cell cultures where the tubulin filaments are immunostained. Tubulin filaments play an important role in spatial organization and transport mechanisms within cells [3, chapter 16].

5.2.1 Materials and Methods

Histological samples. The tissue samples were embedded in GMA (2-hydroxyethyl methacrylate) resin and, using a microtome, semi-

[3]I gratefully thank Jakob Zbären, Inselspital, Bern, for supplying histological samples (Fig. 5.4 to Fig. 5.7) and a microtubule sample (Fig. 5.8). Likewise, I thank Rosemarie Sütterlin and Prof. Ueli Aebi, Biozentrum, Basel, for the other microtubule sample (Fig. 5.9).

thin sections (approx. 750 nm) were cut with glass knives. Apart from the use of different antibodies, the immunostaining procedure for the four tissue sections (Fig. 5.4 to Fig. 5.7) was basically the same. Due to the very weak penetration of the large antibody molecules into the GMA resin, the immunohistochemical reaction is restricted to the section surface. Firstly, appropriate primary antibodies were added to the tissue section. In the next step, suitable secondary antibodies attached to a dextran polymer chain with numerous horseradish peroxidase (HRP) sites (EnVision, Dako Diagnostics, Zug, Switzerland) bound onto the primary antibodies. Finally, fluorochrome conjugated HRP-antibodies were used to visualize the reaction sites whereby several hundred fluorochrome conjugates can bind to the numerous HRP sites available, thus providing a strong fluorescence signal despite the limited antigen epitopes present in the surface layer of the resin sections.

Tubulin filaments immunostained in human endothelial cells (Fig. 5.8). Human endothelial cells were cultured on slides. After fixation a primary anti-β-tubulin antibody was applied followed by a suitable secondary biotinylated antibody. Finally visualization was achieved with the binding of numerous (a few hundred) fluorochrome conjugated anti-biotin antibodies to the reaction sites.

Tubulin sample of human gingiva fibroblasts (Fig. 5.9). Human fibroblasts were grown on a cover slip. After fixation a primary mouse anti-β-tubulin antibody was applied. Finally a fluorophore conjugated anti-mouse antibody was used for visualization. The fluorophore-to-protein ratio was 7.0 (manufacturer specification), therefore, seven fluorophores per antigen epitope is the maximum achievable.

5.2.2 Discussion

Concerning the histological samples Fig. 5.4 to Fig. 5.7, it is striking that the HELM images show a granularity of the fluorescence emission

which is hardly visible in the standard FM images. This granularity probably does not correspond to real biological structures as the size of the vesicles amounts to a few hundred nanometers [3, chapter 13] and, hence, cannot fully explain the observation. The granularity is expected to be partially a result of the sample preparation. The staining procedure employed binds a few hundred fluorophores to one specific antigen epitope. This multiplication of fluorescence emission is required to compensate for the relatively low number of antigens available for immunochemical reactions in polymer. The presumption is that, as a result of the high resolution of HELM, the individual labeled antigen epitopes (with a few hundred fluorophores attached) are resolved and lead to the granular structure. Hence, the high resolving power of HELM shows staining artifacts which are hardly visible in the standard FM images.

For cell culture samples in Fig. 5.8 and Fig. 5.9, different staining procedures were used (see subsection 5.2.1). As a result, the number of fluorophores per labeled antigen epitope amounts to seven for the fibroblast sample (Fig. 5.9) while it is a few hundred for the endothelium cell sample (Fig. 5.8). The observed brightness of the endothelium cell sample was higher by a factor of approx. four in relation to the fibroblast sample. Since this brightness difference is much less than expected as a result of the different staining procedures, it is assumed that the number of antigen epitopes available for staining was higher in the fibroblast sample. This assumption is confirmed by the experimental observation that the fluorescence distribution is more uniform along the filaments in Fig. 5.9 than in Fig. 5.8. The HELM image Fig. 5.8c even shows little gaps along the filaments where no fluorescence emission is observed. The reason for the different number of available antigens, however, is not clear.

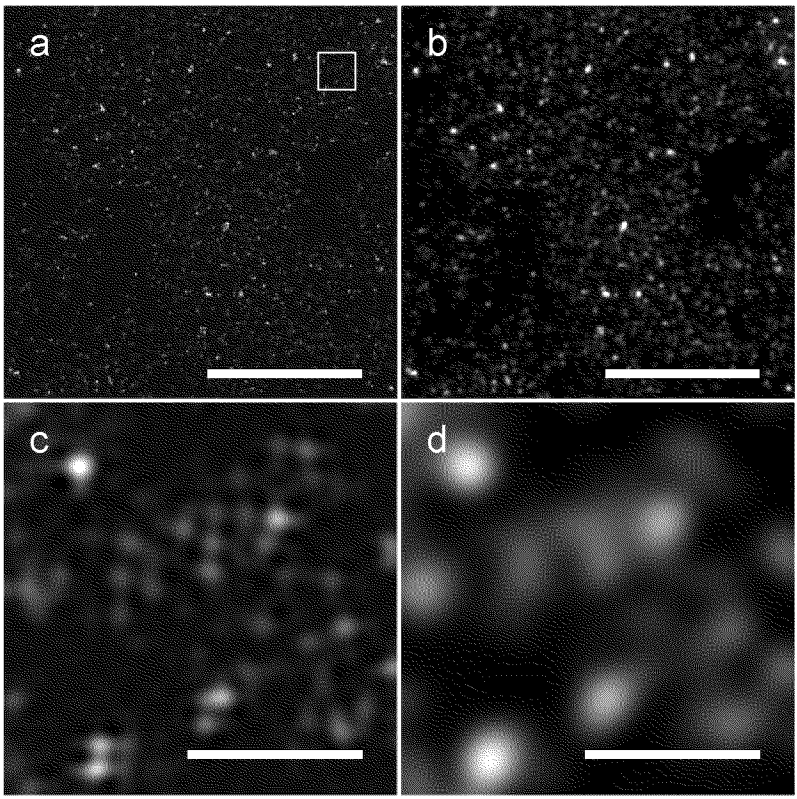

Figure 5.4: Rat pancreas semi-thin plastic section. The hormone insulin secreted by the β-cells of the islets of Langerhans is immunostained. Prior to release from the cells, insulin is contained in secretory vesicles or granules within the cytoplasma. (a) and (b) are imaged by HELM and by standard FM, respectively. Scale bar is 10 μm. (c) and (d) show a small detail of (a) and (b), respectively. Scale bar is 1 μm.

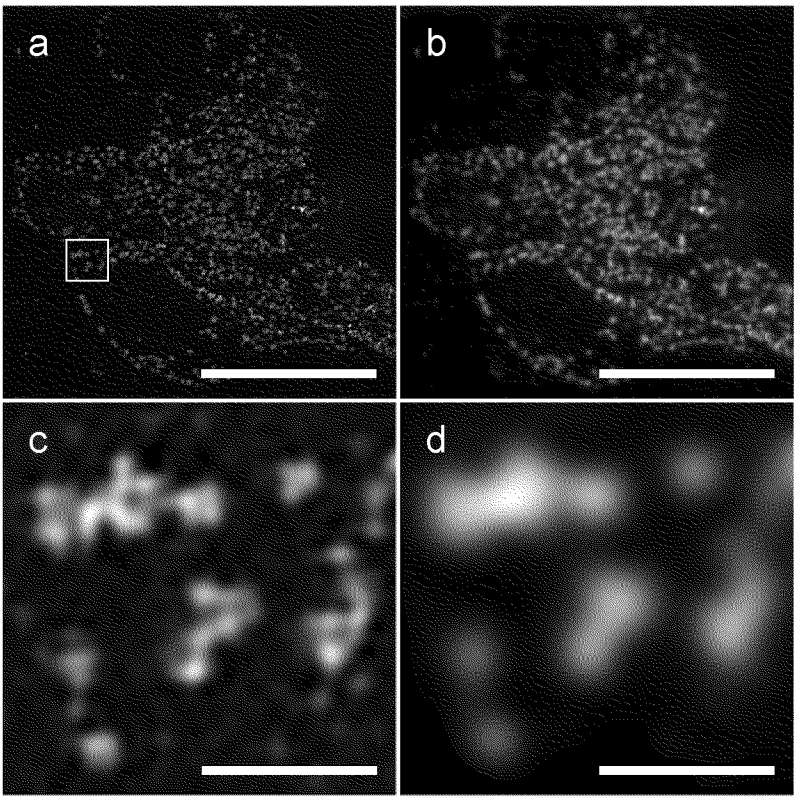

Figure 5.5: Rat pancreas semi-thin plastic section. The hormone glucagon secreted by the α-cells of the islets of Langerhans is immunostained. Prior to release from the cells, glucagon is contained in secretory vesicles or granules within the cytoplasma. (a) and (b) are imaged by HELM and by standard FM, respectively. Scale bar is 10 μm. (c) and (d) show a small detail of (a) and (b), respectively. Scale bar is 1 μm.

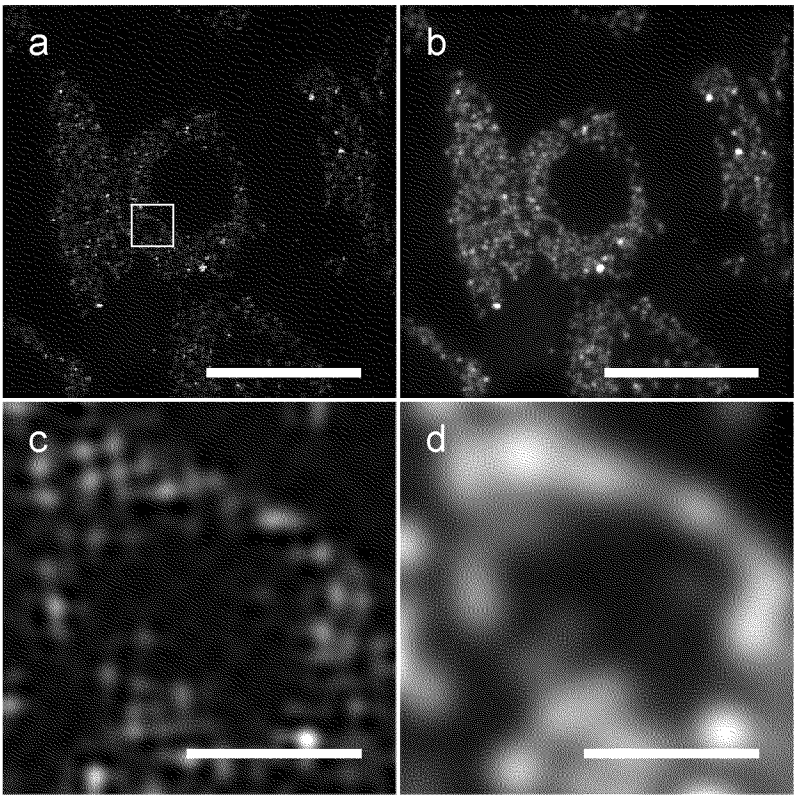

Figure 5.6: Rat hypophysis (pituitary gland) semi-thin plastic section. Sematotropin is immunostained. The sematotroph cells secret the growth hormone, sematotropin, which is contained in secretory vesicles or granules within the cytoplasma prior to release from the cells. (a) and (b) are imaged by HELM and by standard FM, respectively. Scale bar is 10 μm. (c) and (d) show a small detail of (a) and (b), respectively. Scale bar is 1 μm.

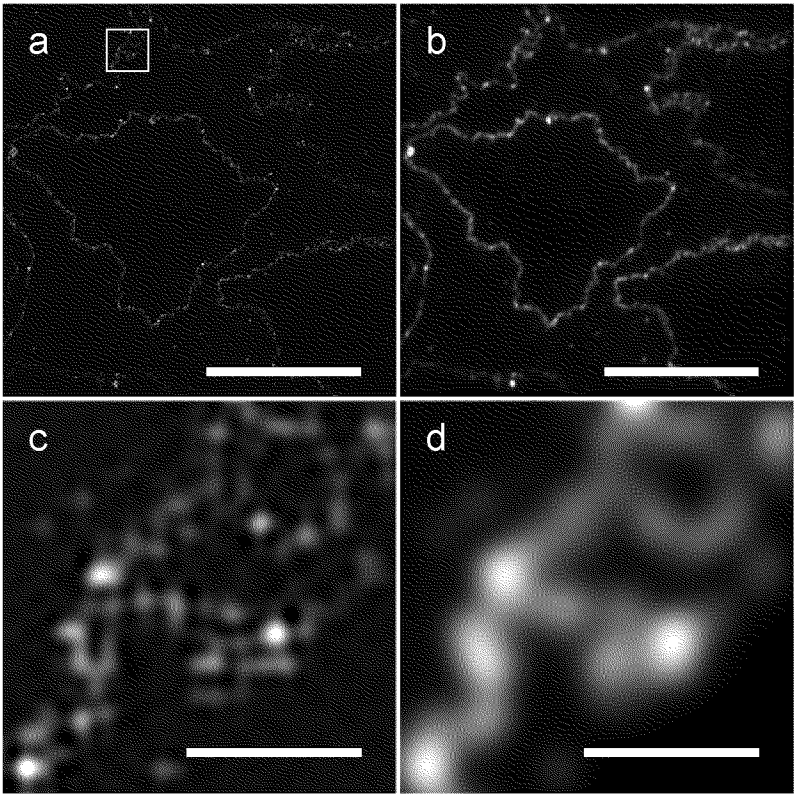

Figure 5.7: Rat kidney semi-thin plastic section. Laminin is immunostained. Laminin and collagen fibrils compose the basal lamina layer of basement membranes which provide structural support for epithelia and build selective barriers between epithelial cells and connective tissue. (a) and (b) are imaged by HELM and by standard FM, respectively. Scale bar is 10 μm. (c) and (d) show a small detail of (a) and (b), respectively. Scale bar is 1 μm.

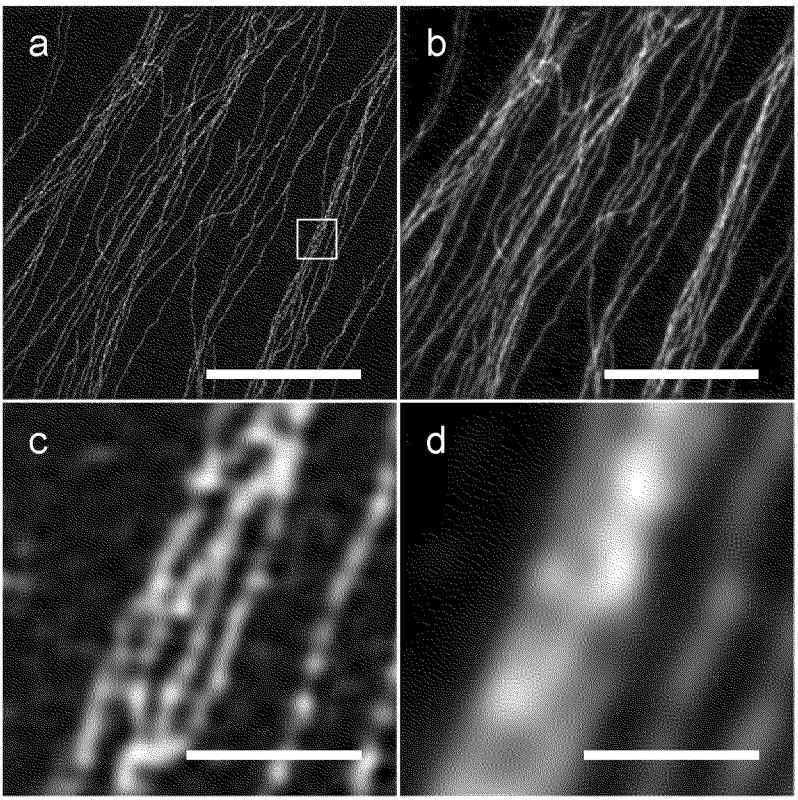

Figure 5.8: Microtubules in human endothelial cells. The actual diameter of the tubulin filaments is about 25 nm. [3, chapter 16]. (a) and (b) are imaged by HELM and by standard FM, respectively. Scale bar is 10 μm. (c) and (d) show a small detail of (a) and (b), respectively. Scale bar is 1 μm.

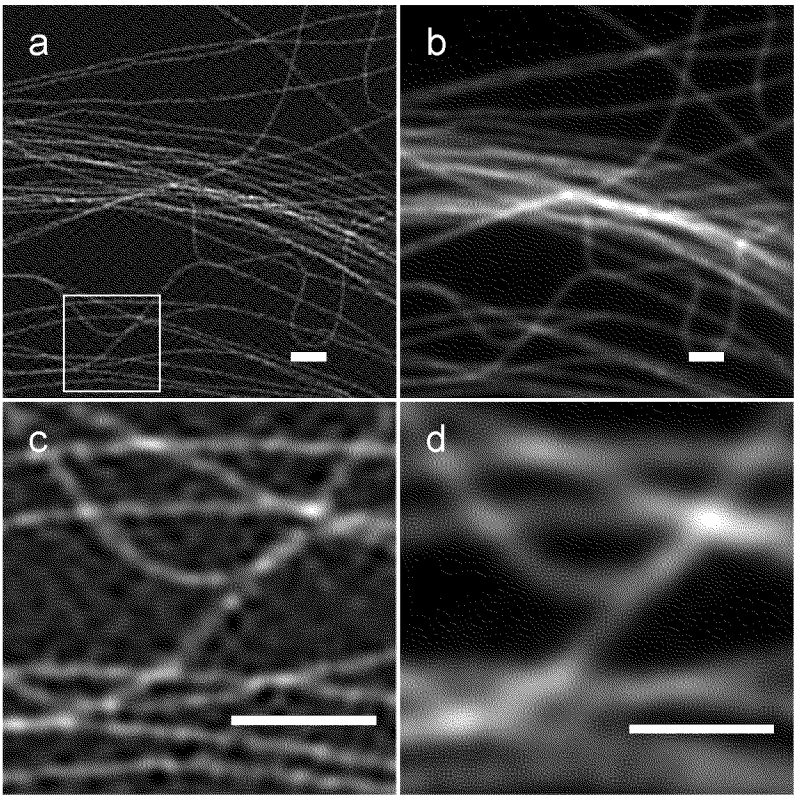

Figure 5.9: Microtubules in a cell culture of human gingiva fibroblasts. The actual diameter of the tubulin filaments is about 25 nm. [3, chapter 16]. (a) and (b) are imaged by HELM and by standard FM, respectively. (c) and (d) show a small detail of (a) and (b), respectively. Scale bar is 1 μm. The structured background is a result of the fact that the contrast of the camera had to be set to a very high value for the relative low luminosity of the sample. Therefore, the noise level is increased in relation to the images in Fig. 5.4 to Fig. 5.8.

5.3 Measuring the OTF

Image reconstruction in HELM by applying Eq. 3.55 requires at least an approximate knowledge of the optical transfer function of the microscope. The OTF expected from scalar theory [33] as well as the predicted cut-off frequency turned out to be noticeably different from the measured ones.

To measure the OTF, polystyrene beads with a diameter of 100 nm and an emission wavelength of 540 nm served as point sources. Two corrections were introduced in the OTF calculations: First, the beads were modeled as uniformly emitting circles. In this case, the spectrum is the well-known *besinc*-function [33], as opposed to the constant spectrum of a point source, and can easily be introduced into the calculations. Secondly, the finite size of the CCD-pixels (8.3 μm $\times$ 8.3 μm on chip corresponding to 53 nm $\times$ 53 nm in the object plane) was taken into account. As the CCD-pixels integrate the incoming light over an area which approximates the pixel size , the CCD-camera acts as an effective low-pass filter [55]. The attenuation at the theoretical cut-off frequency introduced by finite pixel size and finite bead size is 10% and 28%, respectively. The cut-off frequency itself is not affected at all. To assure ideal optical conditions, the beads were adsorbed on a cover slip which was selected for a thickness of 170$\pm$5 μm.

Additionally to the measured and scalar curves, a calculated curve obtained from Carl Zeiss in Göttingen (personal communication Dr. A. Faulstich, 1999) is presented in Fig. 5.10. The manufacturer's curve was computed for an optical system consisting of the objective (Zeiss Plan Apochromat 63$\times$ 1.4 Oil DIC) and the tube lens for a wavelength of 540 nm. In the calculations, both components were assumed to be free from geometric or material imperfections.

Most crucial for HELM is the usable bandwidth of the microscope since this, in conjunction with the spatial frequency of excitation, determines the shape of the passband for HELM. As a practical measure of bandwidth, the spatial frequency for which the value of the OTF

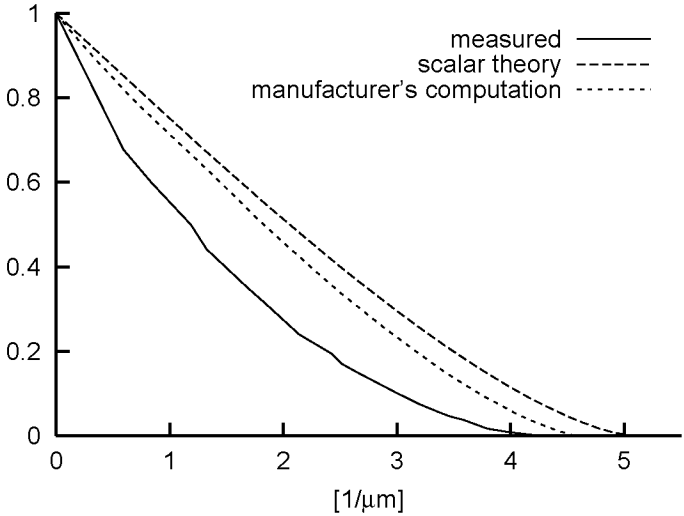

Figure 5.10: Measured and calculated optical transfer function. The spatial frequency is specified in line pairs per μm which is different by a factor of 2π from the angular frequency used elsewhere in the text.

drops below 1% is used. The 1%-bandwidth expected from scalar theory is $4.9/\mu$m whereas the measured one is about $3.95/\mu$m which is a difference of 20%. The manufacturer's value ($4.45/\mu$m) is in between and imposes an upper limit for what can be achieved with the microscope.

Various possible reasons exist for the 10% difference between the manufacturer's cut-off frequency and the measured one. For example, tolerances of the objective and tube lens as well as imperfect additional components (OPTOVAR magnification system, fluorescence filter) will deteriorate the image. Furthermore, the fluorescence emission of the beads is not monochromatic as assumed in the calculations.

Last but not least, the angular emission characteristic of fluorophores at the glass-water interface is more complicated than that one of fluorophores embedded in homogeneous media [5].

Measurements were also performed for a NIKON system (NIKON Eclipse E800 with a NIKON Plan Fluor 100× 1.3 Oil DIC objective). Again, the experimental cut-off frequency was about 25% less than expected.

Measurements performed by other groups also report noticeable differences between measured and predicted imaging properties of the microscope. In [51], point spread functions which are broadened by approx. 25% in relation to theoretical expectation are reported. The measurements were performed under comparable experimental conditions, the OTF was not considered. Cut-off frequencies which differ by about 50% from theory are reported in [74] and [83] but the experimental conditions were quite different (non-fluorescence mode, edge-object instead of point-object).

For the image reconstruction algorithm of HELM, the measured OTF of the microscope is used.

5.4 Determination of geometric parameters of illumination mesh

To determine the orientation and spatial frequency of the interference pattern, one bright-field image I_b with the fluorescence filter removed from the imaging path of the microscope is acquired.[4] Without the fluorescence filter, the direct light from the laser beams is dominant since the fluorescence light is several orders of magnitude weaker. Numerically, the correlation between the measured image and an analytical term for the interference pattern with varying orientation and spatial

[4] Alternatively, the mesh parameters can also be determined from the fluorescence images [35]. Using bright field images for that purpose has the advantage of working independently of the SNR of the fluorescence images.

frequency is maximized according to the following expression:

$$\max_{\Delta_x,\Delta_y,\mathbf{u}_x\mathbf{u}_y} \sum_{l,m} I_{\mathrm{b}}(l,m) \times \left[\cos\left(d\,\mathbf{u}_x \begin{pmatrix} l \\ m \end{pmatrix} + \Delta_x\right) + \cos\left(d\,\mathbf{u}_y \begin{pmatrix} l \\ m \end{pmatrix} + \Delta_y\right)\right], \quad (5.2)$$

where l and m are the x- and y-pixel coordinates, respectively, and d is the pixel distances in the object plane.

By performing the maximization in expression 5.2, the phase offsets Δ_x and Δ_y are also determined. Unfortunately, the removal of the fluorescence filter from the imaging path gives rise to additional displacements in the image, probably due to a slightly wedge-shaped filter or a not ideally infinity corrected optical path.[5] Therefore, there is no absolute spatial coincidence between bright-field and fluorescence image. Fortunately, the absolute phase offset common for all images can be easily determined from the fluorescence images. Assuming additional constant phase offsets, the phase offset pairs Δ_x, Δ_y for the five acquired images become (ϵ_x, ϵ_y), $(\epsilon_x + \pi/2, \epsilon_y)$, $(\epsilon_x + \pi, \epsilon_y)$, $(\epsilon_x, \epsilon_y + \pi/2)$ and $(\epsilon_x, \epsilon_y + \pi)$. It can be easily shown that, by applying Eq. 3.53 with the given coefficients of matrix M^{-1}, the original spectrum $\tilde{\psi}$ multiplied by additional complex phase factors is reconstructed. For the indices $j = 1...5$ these phase factors are $1, e^{i\epsilon_x}, e^{-i\epsilon_x}, e^{i\epsilon_y}$ and $e^{-i\epsilon_y}$, respectively. Depending on temperature and mechanical adjustment of the HELM setup, the constant phase offset ϵ_x and ϵ_y can have any value between 0 and 2π.

To determine ϵ_x and ϵ_y from the measured fluorescence images, the reconstructed spectra for different indices j (denoted as $\tilde{\psi}_{j=k}, k = 1 \ldots 5$) are compared in the appropriate overlap regions. More for-

[5] Since the fluorescence filter is tilted by 45° relative to the optical axis it leads to a lateral displacement of the beams. This lateral beam displacement does not affect the lateral image position in case of parallel beams in infinity corrected systems. However, if the system is not ideally infinity corrected for a certain wavelength the parallel beam displacement leads to a lateral image shift.

mally, ϵ_x and ϵ_y are calculated by

$$\epsilon_x = \arg \frac{\tilde{\psi}_{j=2}}{\tilde{\psi}_{j=1}} = \arg \frac{s_2^{-1} \left(\left[M^{-1} \tilde{\boldsymbol{\theta}} \right]_2 \right)}{\left(M^{-1} \tilde{\boldsymbol{\theta}} \right)_1} \quad \text{and} \tag{5.3}$$

$$\epsilon_y = \arg \frac{\tilde{\psi}_{j=4}}{\tilde{\psi}_{j=1}} = \arg \frac{s_4^{-1} \left(\left[M^{-1} \tilde{\boldsymbol{\theta}} \right]_4 \right)}{\left(M^{-1} \tilde{\boldsymbol{\theta}} \right)_1}, \tag{5.4}$$

where Eq. 3.53 is inserted and where the fact that the OTF T is a real number is used. To achieve precise results, Eq. 5.3 and Eq. 5.4 are averaged for a few points in the appropriate overlap region. To account for the real phase offsets ϵ_x and ϵ_y, the reconstructed spectra $\tilde{\psi}_{j=k}, k = 1 \ldots 5$ are multiplied with the inverse phase factors (i.e. $1, e^{-i\epsilon_x}, e^{i\epsilon_x}, e^{-i\epsilon_y}$ and $e^{i\epsilon_y}$, respectively) before Eq. 3.55 is employed to calculate the spectrum of the final image. Fig. 5.11 illustrates the influence of an intentionally introduced phase offset error of π on the resulting images.

Fig. 5.12 shows the resulting images with various intentionally introduced mesh parameter errors. The conclusion is that errors of 0.1% and 0.25° in spatial frequency and orientation angle, respectively, do not significantly deteriorate the images. This accuracy is easily surpassed by the correlation procedure.

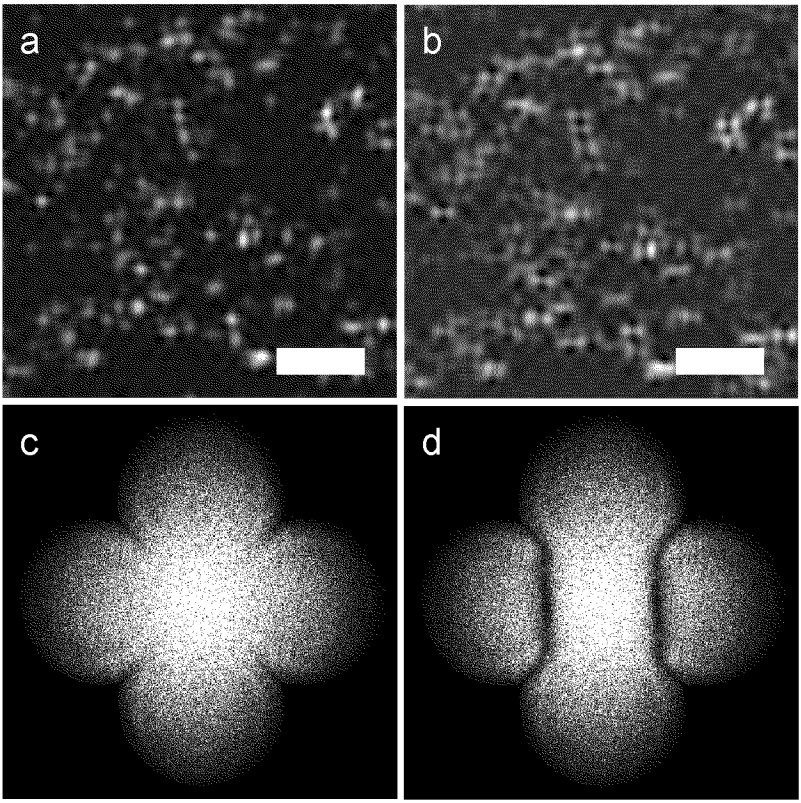

Figure 5.11: The influence of absolute phase errors on image formation in HELM. Scale bar 1 μm. (a) shows a detail of Fig. 5.4a, (c) shows the modulus of the Fourier transform of (a). For images (b) and (d), the x-phase offset ϵ_x determined by applying Eq. 5.3 was intentionally changed by π for image reconstruction. This effectively inverts the horizontally shifted components of the spectrum. As a result, image (d) clearly shows the cancellation in the overlap region. In spatial domain (b), the image looks like an echo image.

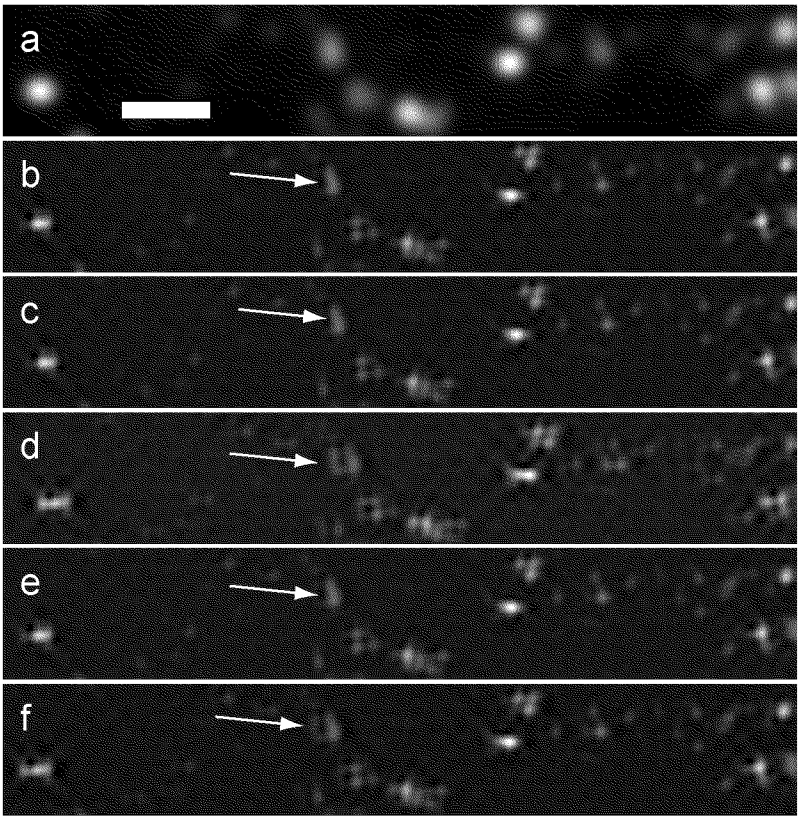

Figure 5.12: The influence of mesh parameter errors on image formation in HELM. Scale bar 1 μm. A detail of Fig. 5.4 is shown. (a) is imaged with standard fluorescence microscopy, (b) is the corresponding HELM image. In (c) and (d) the x-angle γ_x determined by applying Eq. 5.2 was intentionally changed by 0.25° and 1°, respectively, for image reconstruction. In (e) and (f), the determined spatial frequency of excitation $\mathbf{u}_x$ was changed by 0.1% and 0.5%, respectively.

5.5 Influence of defocus on HELM

For defocused objects, the effective OTF of the microscope lenses becomes different from the one used by the image reconstruction algorithm in HELM [33, 12, 24]. As a consequence, the effective HELM-OTF is also altered. Because the width of the OTF is reduced for increasing defocus, the HELM-OTF basically shows a gap at medium frequencies. Experimentally, the influence of defocus is shown in Fig. 5.13.

For increasing defocus, the images show stronger side-lobes, most noticeable is the increased background level. This is a result of the scaling procedure which sets the most negative value to black and the most positive to white.

The occurrence of visible image deterioration for a defocus of about 200 nm is a result of the very low depth of focus of high NA oil-immersion objectives [44]. In [12, chapter 9], the OTF is calculated for various defocus z according to scalar theory. The calculations show that for $z = 240$ nm the value of the OTF at half the cut-off frequency drops to 55% of the in-focus value.[6] Therefore, the results about focus sensitivity of HELM are in good agreement with theoretical predictions.

[6]The parameter m used in the calculations in [12] can be rewritten using the numerical aperture as $m = \frac{\pi \mathrm{NA}^2}{2\lambda n} z$. Therefore, $m = 1$ corresponds to a defocus of 240 nm for NA=1.4, λ=540 nm and n=1.52.

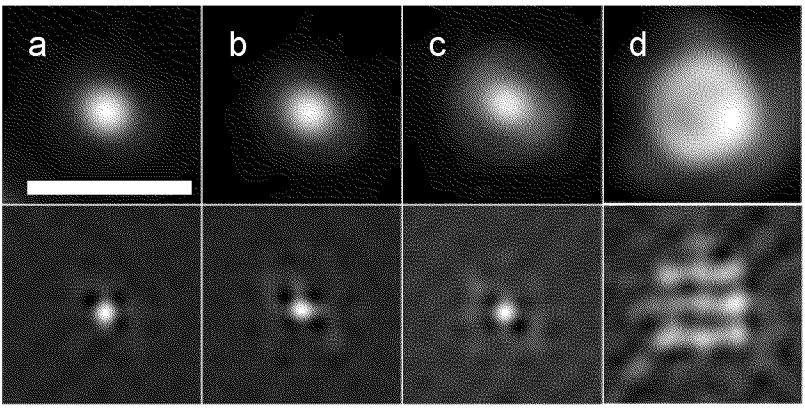

Figure 5.13: Influence of focusing errors on image formation in HELM. Scale bar 1 μm. Images (a) to (c) show four different 100 nm diameter fluorescent beads of the same sample imaged with standard FM (top) and with HELM (bottom) for defocus of 0, 105 nm and 200 nm, respectively. The images are obtained by using a preparation of beads dried on a cover slip which was inclinated by an angle of 0.6° relative to the object plane. In (d) a gelatine embedded bead of the same size located approx. 1-2 μm behind the cover slip is imaged with the focal plane left at the cover slip-water interface. Contrast and brightness of all images are scaled to span the full grey-scale range.

Chapter 6

Three-dimensional HELM

In the previous chapters, the HELM method was discussed in the framework of two-dimensional imaging. For a large area of applications, investigating the three-dimensional structure of the specimen is of major interest. Three-dimensional imaging is possible by stepping the focus through the specimen and, thus, acquiring a stack of two-dimensional images ("optical sectioning microscopy", OSM). Evidently, this requires weakly absorbing objects with low refractive index heterogeneity. Typical biological specimens belong to this class of objects and, therefore, OSM has become an important tool for investigations in structural biology.

Unfortunately, the axial resolution achievable in fluorescence with standard microscopes is strongly limited and, even worse, the images show potential artifacts (see section 6.1).[1] Several attempts have been

[1] In contrast to fluorescence imaging, a very high axial resolution of approx. 200 nm has been reported for phase sensitive imaging modes (e.g. differential interference contrast) [43].

made to enhance the axial resolution in optical microscopy, the most common being the confocal scanning microscope. In this chapter, different known methods for high resolution three-dimensional microscopy will be discussed. Afterwards, the three-dimensional extension of HELM, referred to herein as 3D-HELM, will be studied.

6.1 The limitation of optical sectioning microscopy

In the following, the considerations will be restricted to the case of fluorescence microscopy, i.e. incoherent imaging. In analogy to the two-dimensional case, the microscope can be described as a linear shift invariant system. As mentioned in section 3.1, LSI systems can be completely described by their optical transfer function. The three-dimensional OTF (denoted herein as 3D-OTF) can be derived from the two-dimensional OTF for various degrees of defocus[2] [29, 24] which can be calculated by scalar diffraction theory [33]. The 3D-OTF (shown schematically in Fig. 6.1) is a torus-like object with two key properties:

1. The support of the OTF (the passband) does not include a cone-shaped region around the k_z-axis centered at the origin (generally known as "missing cone"). As a consequence, even very low frequency components of the object spectrum are not transferred at all. The spectrum of slice-shaped objects oriented parallel to the x-y-plane, for instance, mainly consists of components within the cone-shaped region. Consequently, such objects are hardly resolved [54]. The fact that the resolution for

[2]With $\mathrm{OTF}_{z_0}(k_x, k_y)$ denoting the 2D-OTF for defocus z_0, the 3D-OTF $\mathrm{OTF}(k_x, k_y, k_z)$ can be easily shown to be the Fourier transform of $\mathrm{OTF}_{z_0}(k_x, k_y)$ with respect to the z_0-coordinate. The 2D-OTF can be obtained from the 3D-OTF by averaging the values along the k_z-axis.

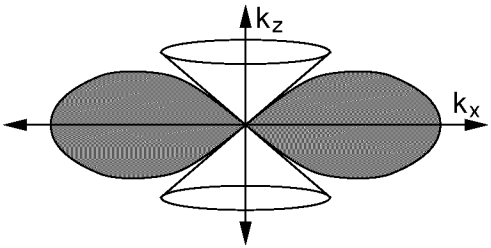

Figure 6.1: The support of the three-dimensional OTF of a fluorescence microscope. Shown is a k_x-k_z cut-view of the rotational symmetric function. The OTF is exactly zero within a conical region around the k_z-axis.

particular objects can break down completely is often referred to as artifactual imaging.

2. The 3D-OTF becomes singular at the origin. This property of the OTF corresponds to the fact that the average intensity of an image is independent of the defocus of the object.[3] As a consequence, the contrast of thick objects is strongly reduced as the highly-resolved in-focus information is overlaid by a strong out-off-focus blur.

Due to these unfavorable properties of 3D-imaging with standard fluorescence microscopes, alternative methods to achieve an uniformly high resolution in three-dimensional space have been intensely studied in the last three decades. The most relevant ones will be shortly discussed in the next section.

[3]Conservation of average intensity is a consequence of the fact that all photons entering the lenses contribute to the image produced by the microscope.

6.2 Approaches for axial resolution enhancement

6.2.1 The confocal microscope

In confocal fluorescence microscopy (CFM), photons originating from *out-off-focus* planes are partially blocked by a small pinhole located in a secondary image plane of the microscope. The OTF of the confocal microscope can be shown to be the autocorrelation of the standard OTF[4] [75, 54] and has neither singularities nor missing cones (see Fig. 6.2**a**). The extent of the passband in lateral as well as in axial direction is doubled in relation to standard fluorescence microscopy. However, the achievable resolution gain is less due to the rapid decline of the OTF towards high spatial frequencies. The lateral resolution is of the order of 150 nm at best for NA 1.4 oil-immersion objectives and the axial one is about 0.8 μm [14] and, thus, still inferior to the lateral one. These ideal values are achieved for an infinitesimally small pinhole, consequently the real resolution gain is less [49, 23, 85, 78]. In addition to the limited photon efficiency caused by the pinhole, CFM has two main drawbacks:

1. The scanning data acquisition limits—at least for practical reasons—the achievable imaging speed. These difficulties, however, can be reduced by the newer multi-point scanners [47, 86].

2. The high peak intensities of the focused laser beam in CFM potentially saturate the fluorophores (see subsection 3.2.2). As a result, the total photon flux emitted from the specimen is limited to values several orders of magnitude lower than for methods illuminating the whole specimen in parallel. Since a minimum number of photons is required for a certain signal-to-noise level, the fundamental imaging speed limitation is much

[4]For fluorescence microscopy, this relation is an approximation not taking into account the wavelength difference between excitation and emission light.

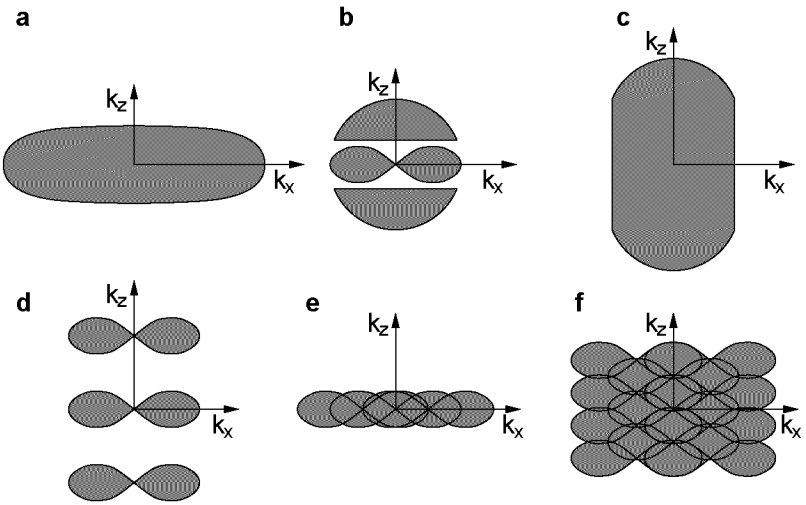

Figure 6.2: Qualitative illustration of passband enhancements achieved by different approaches. Panels (**a**) to (**e**) show the passbands achieved by confocal microscopy, I^2M, I^5M, ASWFM and LSWFM, respectively. (**f**) is the resulting passband obtained in 3D-HELM for one particular combination of excitation patterns with various orientations. Only confocal microscopy and 3D-HELM allow simultaneous enhancement of lateral as well was axial resolution.

lower for CFM than for parallel methods (see also subsection 5.1.1).

A derivative of the CFM is the so-called 4π-microscope [39, 40]. Here, a second objective is used for illuminating and for imaging purposes. By using such an arrangement, the axial resolution is improved to about 120 nm while the lateral resolution remains unchanged compared to the CFM. The 4π-arrangement is very sensitive to displacements of one objective relative to the other and it requires digital

image processing to remove artifacts originating from the extremely non-uniform OTF.

6.2.2 Image interference microscopy (I^2M)

As the 4π-microscope does, image interference microscopy (I^2M) also employs a second objective. But, in contrast, it is a non-scanning method. The images produced by the two objectives are coherently superimposed on a CCD-chip [36, 37]. As a result, additional high axial frequency components of the specimen are transferred resulting in an increased axial resolution. However, there is still a missing cone in the OTF making the images potentially artifactual (see Fig. 6.2**b**). A further development of the I^2M is the "image interference with incoherent interference illumination" microscopy (I^5M) [38]. Here, the focal plane is selectively illuminated by interference of two beams originating from an incoherent light source. The axial resolution of this device is approx. 120 nm and, thus, even outperforms the lateral one (see Fig. 6.2**c**). Just as 4π-microscopy, I^2M and I^5M are sensitive to relative displacements of the objectives and require digital post-processing of the images. Furthermore, the lateral resolution of I^2M and I^5M is not increased at all in relation to standard fluorescence microscopy.

6.2.3 Computational methods

Another approach for increased axial resolution (and sometimes also for lateral one) does not address the image formation in the microscope itself but employs digital image processing algorithms to extract additional information [8, 2, 1, 42, 53, 18, 19]. Taking into account a priori knowledge such as non-negativity of the intensity distribution, reconstruction of some parts of the spectrum outside the support of the OTF is possible. In practice, however, such methods are susceptible to noise in the images, particularly posing a problem in fluorescence microscopy.

6.2.4 Standing wave excitation methods

Different approaches addressing axial resolution enhancement by standing wave excitation have been proposed. Interference fields with their nodal and antinodal planes parallel to the object plane can be employed to selectively excite individual sections of the specimen (axial standing wave fluorescence microscope, ASWFM). For objects which are thin in relation to the period of the excitation pattern, an axial resolution of the order of one tenth of the emission wavelength was found [6, 28, 54]. For arbitrary objects, however, the imaging is still potentially artifactual as a missing cone in the OTF [52] remains (see Fig. 6.2**d** and section 6.3).

Another approach is based on interference fields with their nodal and antinodal planes in parallel to the optical axis (lateral standing wave fluorescence microscope, LSWFM). An axial resolution of about 400 nm has been demonstrated [64, 65], which is an improvement to standard fluorescence microscopy but still inferior to the lateral resolution (see Fig. 6.2**e**). The effect of arbitrarily oriented standing wave patterns on the 3D-OTF will be studied formally in section 6.3.

Another related technique is topometry by fringe projection [88]. Here, a topographic map of the specimen is obtained by oblique projection of a fringe pattern onto the object surface. By this projection, the depth information is encoded in the phase shift of the fringe pattern. Digital image processing is used to reconstruct the topographic information [87].

6.3 3D-OTF extension by harmonic excitation

The effect of excitation with a three-dimensional interference pattern on the 3D-OTF can be described in far-reaching analogy to the two-dimensional case (see section 3.3.1 and 3.3.2). An excitation pattern

generated by interference of two laser beams[5] can be described by an intensity distribution $I(\mathbf{r})$ according to

$$I(\mathbf{r}) = 1 + M\cos(\mathbf{ur} + \Delta)), \tag{6.1}$$

where M is the modulation depth, $\mathbf{u}$ is the spatial frequency of excitation, Δ accounts for an arbitrary phase offset and where scaling factors are neglected. The Fourier transform $\tilde{I}$ of the intensity distribution is

$$\tilde{I}(\mathbf{k}) = 8\pi^3\delta(\mathbf{k}) + 4\pi^3 M\left[e^{i\Delta}\delta(\mathbf{k}+\mathbf{u}) + e^{-i\Delta}\delta(\mathbf{k}-\mathbf{u})\right], \tag{6.2}$$

where δ denotes Dirac's delta function. Introducing the following scale-shift operators

$$s_1(F(\mathbf{v})) := F(\mathbf{v}), \tag{6.3}$$
$$s_2(F(\mathbf{v})) := MF(\mathbf{v}+\mathbf{u}) \quad \text{and} \tag{6.4}$$
$$s_3(F(\mathbf{v})) := MF(\mathbf{v}-\mathbf{u}), \tag{6.5}$$

one obtains for the spectrum $\tilde{\theta}$ of the three-dimensional image produced by the microscope:

$$\tilde{\theta} = T\Big[2s_1(\tilde{\psi}) + e^{i\Delta}s_2(\tilde{\psi}) + e^{-i\Delta}s_3(\tilde{\psi})\Big], \tag{6.6}$$

where $\tilde{\psi}$ is the fluorescence spectrum and T is the 3D-OTF and where scaling factors are neglected. By sequential acquisition of three images θ_1, θ_2 and θ_3 for phase offsets of Δ_1, Δ_2 and Δ_3, respectively, the following 3×3 set of linear equations is obtained:

$$\begin{pmatrix}\tilde{\theta}_1\\ \tilde{\theta}_2\\ \tilde{\theta}_3\end{pmatrix} = T\overbrace{\begin{pmatrix}2 & e^{i\Delta_1} & e^{-i\Delta_1}\\ 2 & e^{i\Delta_2} & e^{-i\Delta_2}\\ 2 & e^{i\Delta_3} & e^{-i\Delta_3}\end{pmatrix}}^{=:M}\begin{pmatrix}s_1(\tilde{\psi})\\ s_2(\tilde{\psi})\\ s_3(\tilde{\psi})\end{pmatrix} \tag{6.7}$$

[5]Section 6.4 explains why the considerations are restricted to two beam interference for 3D-HELM.

The object spectrum can be reconstructed by

$$\tilde{\psi} = s_j^{-1}\left(\frac{\left(M^{-1}\tilde{\boldsymbol{\theta}}\right)_j}{T}\right) \qquad 1 \le j \le 3, \tag{6.8}$$

in regions where $s_j^{-1}(T) \neq 0$ for at least one index $1 \le j \le 3$. As s_2 and s_3 shift by the vector $\pm\mathbf{u}$ in reciprocal space, the effective passband becomes the total of the original one plus two shifted copies.

Additional copies of the 3D-passband shifted in desired directions in reciprocal space can be obtained by employing excitation patterns with appropriate orientations.

Fig. 6.2**f** illustrates how such additional passband regions can be superimposed to a passband with a high cut-off frequency throughout reciprocal space. Thus, lateral as well as axial resolution enhancement can be achieved at one time in 3D-HELM.

6.4 A three-dimensional HELM setup

In this section, a practical realization of a 3D-HELM device will be analyzed. In section 6.3, it is shown that extension of the 3D-passband is possible if interference patterns with various orientations are employed. In relation to the 2D-setup described in chapter 4, there are three major differences:

1. In 2D-HELM, two patterns with orthogonal orientation were overlaid in the object space *at one time*. This enables one to enhance the resolution in two dimensions without the need for deflection units. In 3D-HELM, this method becomes unpractical as one would have to overlay more than two patterns with various orientations. Therefore, a practical setup will produce patterns oriented along selected orientations *sequentially* by appropriate deflection units.

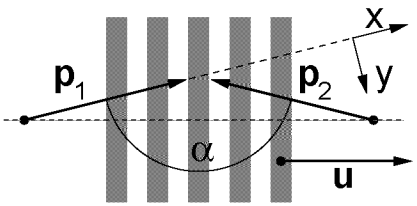

Figure 6.3: Superposition of two mutually coherent beams with wave vectors $\mathbf{p}_1$ and $\mathbf{p}_2$. For simplicity, $\mathbf{p}_1$ is assumed to be parallel to the x-axis.

2. In 2D-HELM, the propagation vectors of the incident beams reside within the lower half space as the beams are coupled to the specimen from the backside through the slide (Fig. 4.5). In 3D-HELM, the propagation vectors of the two interfering beams reside in the lower and upper half space (see subsection 6.4.1). This requires a second objective for illumination.

3. In 2D-HELM, the interfering beams are linearly polarized with parallel orientation for maximum modulation depth. Ensuring parallel polarization in a 3D-setup would require additional mechanical degrees of freedom (DOF) for rotatable half-wave plates. Using circularly polarized light instead leads to a reduced modulation depth (see subsection 6.4.1) but makes the setup remarkably simpler.

The following subsections will discuss the realization of a 3D-HELM setup in more detail.

6.4.1 Two-beam interference

We consider the interference of two coherent plane waves according to Fig. 6.3. The two plane waves are assumed to be *circularly* polarized with opposite sense of rotation. The complex electric fields of these

waves can be described by

$$\mathbf{E}_1 = \begin{pmatrix} 0 \\ 1 \\ i \end{pmatrix} e^{i\mathbf{p}_1\mathbf{r}} \quad \text{and} \tag{6.9}$$

$$\mathbf{E}_2 = \begin{pmatrix} -\sin(\alpha) \\ -\cos\alpha \\ i \end{pmatrix} e^{i\mathbf{p}_2\mathbf{r}}, \tag{6.10}$$

where $|\mathbf{p}_1| = |\mathbf{p}_1| = K$ with $K = \frac{2\pi n}{\lambda}$ where λ is the wavelength of excitation and n is the refractive index of the medium. For the intensity distribution $I(\mathbf{r})$ one obtains

$$I(\mathbf{r}) = |\mathbf{E}_1 + \mathbf{E}_2|^2 = 4\left(1 + \frac{1-\cos(\alpha)}{2}\,\cos\big([\mathbf{p}_1 - \mathbf{p}_2]\mathbf{r}\big)\right). \tag{6.11}$$

Except for scaling factors and a phase offset, Eq. 6.11 corresponds to Eq. 6.1 with the modulation depth $M = (1-\cos(\alpha))/2$ and with the spatial frequency of excitation $\mathbf{u} = \mathbf{p}_1 - \mathbf{p}_2$. As $\mathbf{u}$ depends on the difference vector $(\mathbf{p}_1 - \mathbf{p}_2)$ only, a rotation of both incident beam vectors around the dashed horizontal line in Fig. 6.3 leaves the pattern unaffected.

By using $|\mathbf{p}_1 - \mathbf{p}_2| = 2K\sin(\alpha/2)$ and by using the trigonometric identity $\cos(2\alpha) = 2\cos^2(\alpha) - 1$, the modulation depth M can be rewritten as

$$M = \frac{1-\cos(\alpha)}{2} = \left(\frac{|u|}{2K}\right)^2. \tag{6.12}$$

According to Eq. 6.12, M is proportional to the squared modulus of the shift vector $\mathbf{u}$ and becomes zero for $\mathbf{u} = 0$.

6.4.2 Choosing the incident beam vectors

As shown in subsection 6.4.1, the choice of the incident beam vectors $\mathbf{p}_1$ and $\mathbf{p}_2$ for a desired spatial frequency of excitation $\mathbf{u}$ is ambiguous.

In this subsection, a particular choice will be derived for which $\mathbf{p}_1$ and $\mathbf{p}_2$ reside in the lower and upper half space, respectively.

Given a desired spatial frequency of excitation $\mathbf{u}$ with $|\mathbf{u}| \leq 2K$ and $\mathbf{u}_z \geq 0$,[6] the incident beam vectors are set to

$$\mathbf{p}_{1z} = \frac{\mathbf{u}_z}{2}, \tag{6.13}$$

$$\mathbf{p}_{2z} = -\frac{\mathbf{u}_z}{2}, \tag{6.14}$$

$$\mathbf{p}_{1x} = \frac{\mathbf{u}_x}{2} + \mathbf{u}_y \sqrt{\frac{K^2 - \frac{\mathbf{u}_z^2}{4}}{\mathbf{u}_x^2 + \mathbf{u}_y^2} - \frac{1}{4}}, \tag{6.15}$$

$$\mathbf{p}_{2x} = \mathbf{p}_{1x} - \mathbf{u}_x, \tag{6.16}$$

$$\mathbf{p}_{1y} = \frac{\mathbf{u}_y}{2} - \mathbf{u}_x \sqrt{\frac{K^2 - \frac{\mathbf{u}_z^2}{4}}{\mathbf{u}_x^2 + \mathbf{u}_y^2} - \frac{1}{4}} \quad \text{and} \tag{6.17}$$

$$\mathbf{p}_{2y} = \mathbf{p}_{1y} - \mathbf{u}_y. \tag{6.18}$$

This choice fulfills $\mathbf{u} = \mathbf{p}_1 - \mathbf{p}_2$, $|\mathbf{p}_1| = |\mathbf{p}_2| = K$ and, additionally, makes the z-components of $\mathbf{p}_1$ and $\mathbf{p}_2$ the inverse of each other.

6.4.3 A setup with minimal number of DOF

A possible realization for a 3D-HELM setup is shown in Fig. 6.4. The setup makes use of the fact that, for the particular choice of incident

[6] $\mathbf{u}_z \geq 0$ implies no essential restriction as the transformation $\mathbf{u} \leftrightarrow -\mathbf{u}$ does not change the pattern (Eq. 6.1).

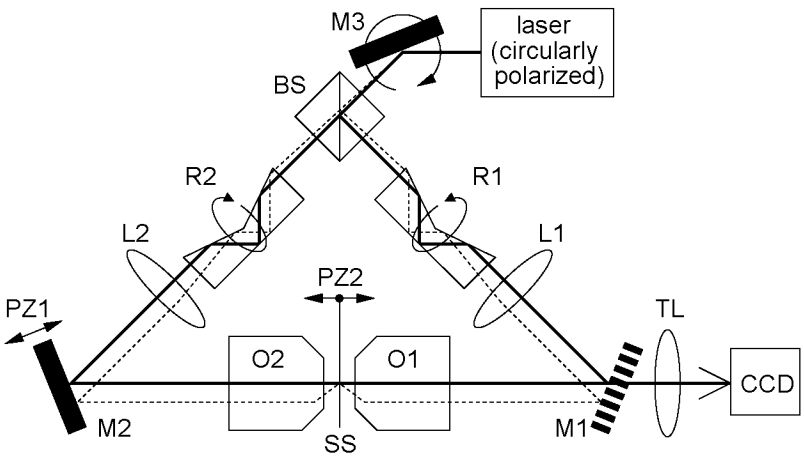

Figure 6.4: Proposed setup for 3D-HELM. This arrangement requires the minimum number of DOF. A beam splitter BS splits a collimated laser beam into two beams of equal intensity which illuminate the specimen through two objectives O1 and O2. Two lenses L1 and L2 form a focal spot in the back aperture of O1 and O2, respectively. An actuated mirror M3 located in the focal plane of L1 and L2 sets the common off-axis distance of the focal spots. Rotatable Abbe-König prisms R1 and R2 rotate the focal spots around the optical axis [63]. A piezo actuated mirror M2 serves for setting the phase offset of the interference pattern. A dichromatic mirror M1 allows one acquisition of the fluorescence image with a CCD-camera.

beam vectors described in subsection 6.4.2, the projections of $\mathbf{p}_1$ and $\mathbf{p}_2$ on the object plane have equivalent length. This corresponds to the fact that the off-axis distances of the focal spots formed in the back apertures of the two objectives are equivalent.

If the DOFs for CFM required in practice are related to those of 3D-HELM, it turns out that 3D-HELM requires one additional DOF:

3D-HELM		CFM	
Pattern orientation	2	Lateral scanning	2
Pattern spacing	1	Pinhole radius	1
z-Translation stage	1	z-Translation stage	1
Phase offset	1		
$\sum$	5	$\sum$	4

The drawback of the additional DOF in 3D-HELM, however, is compensated by the lower speed requirements for the 3D-HELM actuators: In CFM, the fastest DOF requires one scan per line. In 3D-HELM the piezo actuated mirror for setting the phase offset and the z-translation stage require one scan per 2D-image. The other DOFs require one scan per 3D-image only, i.e. one scan in several tens of seconds. Since these lower speed requirements for 3D-HELM drastically simplify the actuator design, it is expected that a practical realization of 3D-HELM should not cost more than one for CFM.

6.5 Simulation results

In this section, simulation results for 3D-HELM are presented. The simulations are based on a numerical aperture of the objective of 1.4, an excitation wavelength of 488 nm and an emission wavelength of 540 nm. The 3D-OTF used in the calculations is an approximation given in [24]. This approximation is valid if the thickness of the object does not exceed approx. 15 μm.

For the standard fluorescence microscope simulations, this approximative OTF is used without any modifications. For the 3D-HELM calculations, the object spectrum is computationally apodized within the passband by a cosine-bell.

In 3D-HELM, a variety of possible combinations of shift directions can be employed for passband extension. The simulations cover three particular combinations of shift vectors given in Tab. 6.1. The resulting passband is shown schematically in Fig. 6.5. Case (b) is a

case	normalized shift vectors (k_x, k_y, k_z)	number of required images	minimal modulation depth
a	—	1	—
b	$(0.5, 0, 0)$	3	0.23
c	$(0, 0, 0.65)$ $(0.5, 0, 0.325)$ $(0, -0.5, 0.325)$ $(-0.5, 0, 0.325)$ $(0, 0.5, 0.325)$	11	0.31
d	$(0, 0, 0.65)$ $(0.5, 0, 0.325)$ $(0, -0.5, 0.325)$ $(-0.5, 0, 0.325)$ $(0, 0.5, 0.325)$ $(0.5, 0, 0.975)$ $(0, -0.5, 0.975)$ $(-0.5, 0, 0.975)$ $(0, 0.5, 0.975)$	19	0.31

Table 6.1: The particular combinations of shift vectors the simulations are performed for. The shift vectors given are normalized with respect to the incoherent cut-off frequency which is $\frac{4\pi \mathrm{NA}}{\lambda}$. The number of required images (per 2D-section) is $2N+1$ with N the number of employed shift vectors.[7] The minimum modulation depth is calculated by Eq. 6.12.

very simple one since only one shift direction parallel to the k_x-axis is used. Therefore, the OTF (as well as the PSF) is not symmetric

[7]The first employed shift vector requires a total of three images to reconstruct the object spectrum within the original passband plus the two shifted passband regions. For each additional shift vector, the unshifted component is already known. Therefore, only two additional images per further shift vector are required.

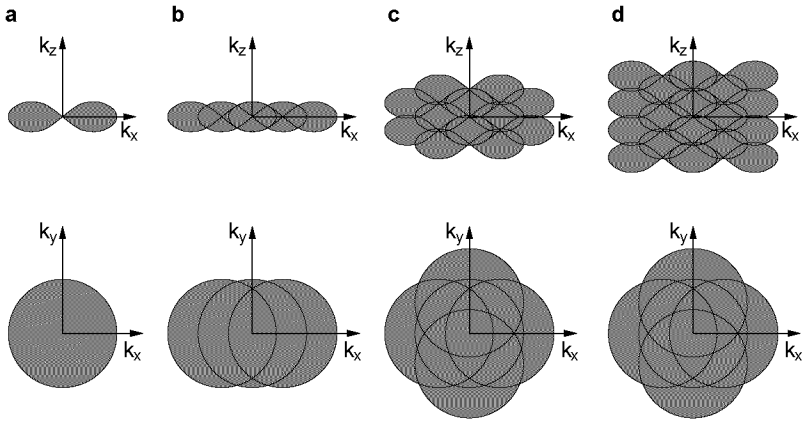

Figure 6.5: Schematic representation of the passband regions obtained by using the combinations of shift vectors given in Tab. 6.1. The panels (**a**) to (**e**) correspond to the cases (a) to (e) from Tab. 6.1. Shown is a projection on the k_x-k_z-plane (top row) and on the k_x-k_y-plane (bottom row).

with respect to the k_x- and k_y-coordinate. Case (c) employs a total of five shift directions. The OTF as well as the PSF are symmetric with respect to the k_x- and k_y-coordinate. Case (d) further increases the axial resolution by using four additional shift directions. The symmetry corresponds to that one of case (c). For case (c) and (d), data for the diagonal direction in the k_x-k_y-plane are also given in Fig. 6.8 and 6.9. Additionally, each figure shows calculations for standard fluorescence microscopy (case (a)).

For each of these cases, the microscope's response to two different objects is calculated. First, a point-like object is simulated to obtain the 3D-PSF of 3D-HELM. Secondly, a infinitesimally thin slice with a diameter of 2 μm oriented parallel to the x-y-plane is considered. Such slice objects clearly illustrate the imaging artifacts present in

case	FWHM lateral point	FWHM axial point	FWHM axial slice, 2 μm$\varnothing$
a	200 nm	480 nm	2270 nm
b	125 nm	470 nm	410 nm
c	125 nm	180 nm	220 nm
d	125 nm	115 nm	120 nm

Table 6.2: The full widths at half maximum (FWHM) of the responses to point and slice objects. The data are extracted from the graphs shown in Fig. 6.8 and Fig. 6.9.

standard optical sectioning microscopy (see Fig. 6.7a). The results of the simulations are summarized in Tab. 6.2.

6.6 Conclusion

The simulation results clearly show that an almost isotropic resolution in the 100 nm range can be achieved in three-dimensional harmonic excitation light microscopy. As an especially useful feature, the lateral as well as axial resolution in 3D-HELM can be adjusted to the specific demands by choosing an appropriate combination of shift vectors.

The number of required images for 3D-HELM given in Tab. 6.1 seems rather high. However, it must be related to the maximum voxel size which is imposed by the Shannon criterion. In lateral as well as in axial direction, the cut-off frequency in CFM is twice that one of standard fluorescence microscopy. Therefore, the maximum voxel volume of the original images is eight times higher in 3D-HELM than in CFM. Consequently, the images in 3D-HELM can be acquired eight times faster to obtain the same number of photons per voxel.

For a practical realization of 3D-HELM, some aspects have to be

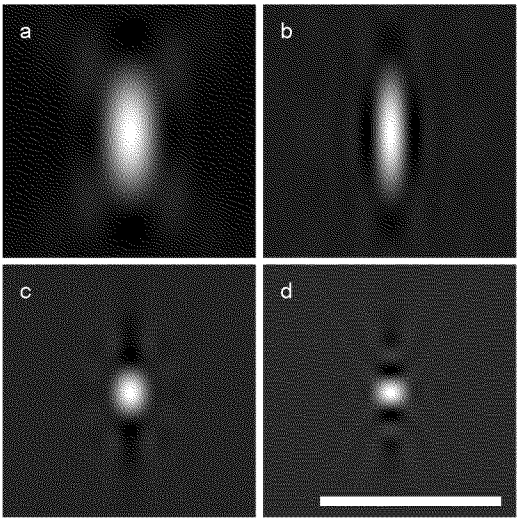

Figure 6.6: Calculated point spread functions for for 3D-HELM. Panels (a) to (d) correspond to to the respective cases in Tab. 6.1. Shown is a k_x-k_z-section of the three-dimensional PSF. To enhance the visibility of the side lobes, a non-linear grey scale with $\gamma = 1.2$ was used. Scale bar is 1 μm.

considered more carefully than in 2D-HELM. Thermal drift could become a serious problem due to the strongly extended data acquisition time. It is expected, however, that drift problems can be handled by an optimized design and/or computational drift compensation by the image reconstruction algorithm. Furthermore, a different approach for pattern parameter estimation is required. Basically, this is possible in two dimensions as well as in three by analyzing the overlap regions of the different passband copies in 3D-HELM [35]. And, last but not least, the efficiency of the algorithm is of major concern due

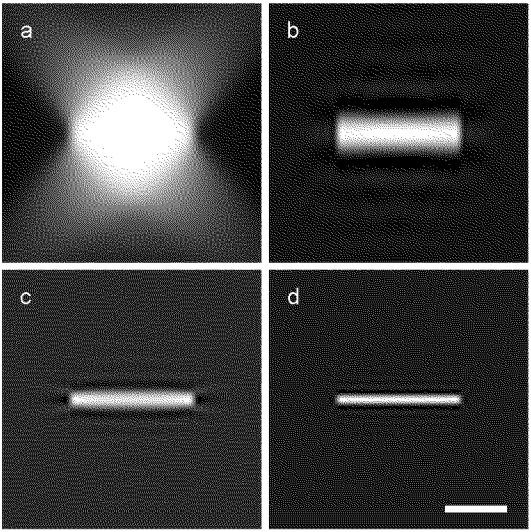

Figure 6.7: Calculated responses to a slice object (diameter 2 μm) in 3D-HELM. Panels (a) to (d) correspond to to the respective cases in Tab. 6.1. Shown is a k_x-k_z-section of the three-dimensional image. To enhance the visibility of the side lobes, a non-linear grey scale with $\gamma = 1.2$ was used. Scale bar is 1 μm.

to the high volume of data.

To conclude, 3D-HELM has the potential to achieve an unrivaled resolution in three dimensional space. Furthermore, HELM has some inherent advantages compared to CFM since neither a photon blocking pinhole is required nor limitations imposed by dye saturation are relevant. The cost of the experimental setup is comparable to that one of CFM. The additional problems of 3D-HELM in relation to the two-dimensional case are technical ones and are expected to be solvable.

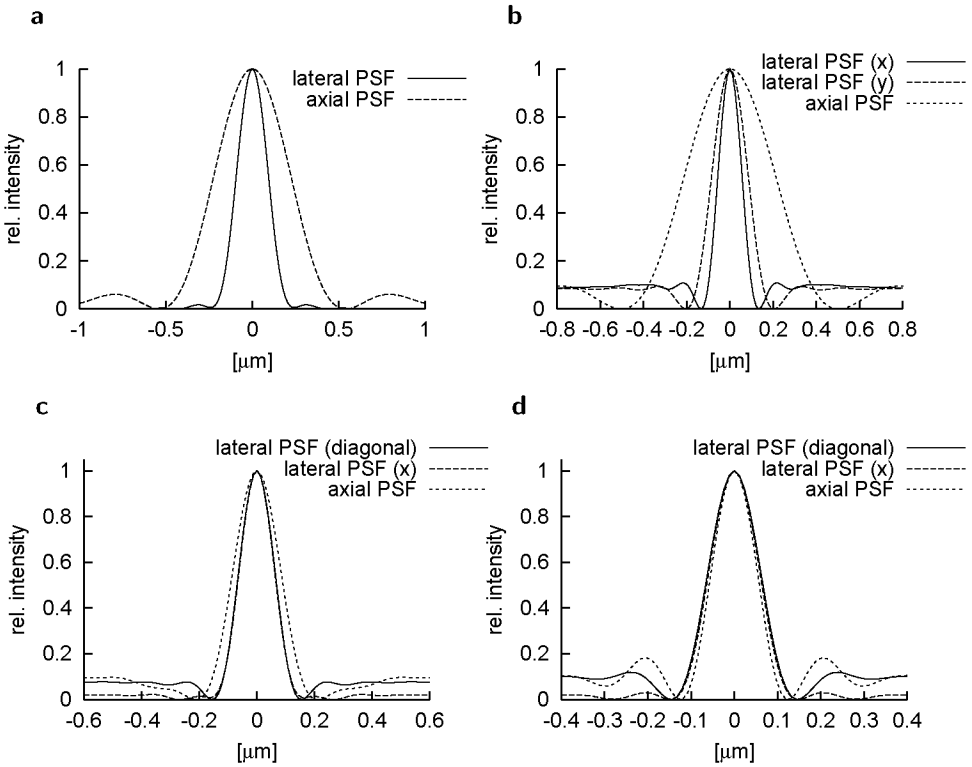

Figure 6.8: Calculated point spread functions in 3D-HELM. Graphs (**a**) to (**d**) refer to case (a) to (d) of Tab. 6.1. Attention should be paid to the different scalings on the abscissae.

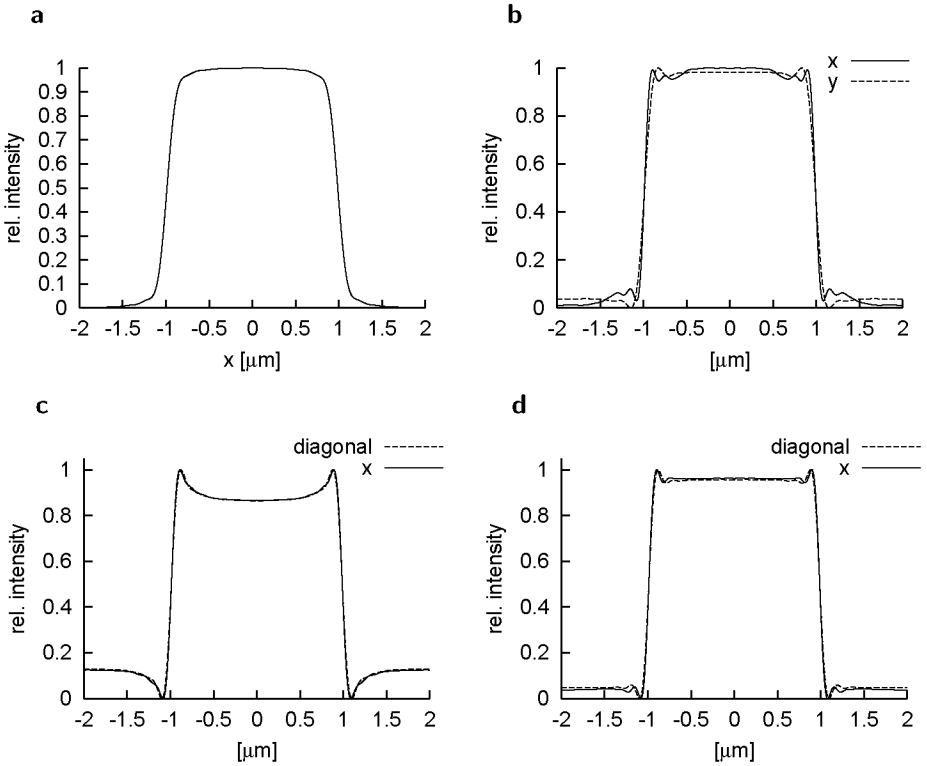

Figure 6.9: Calculated lateral responses to a thin slice of 2 μm diameter oriented parallel to the k_x-k_y-plane. Graphs (**a**) to (**d**) refer to cases (a) to (d) of Tab. 6.1.

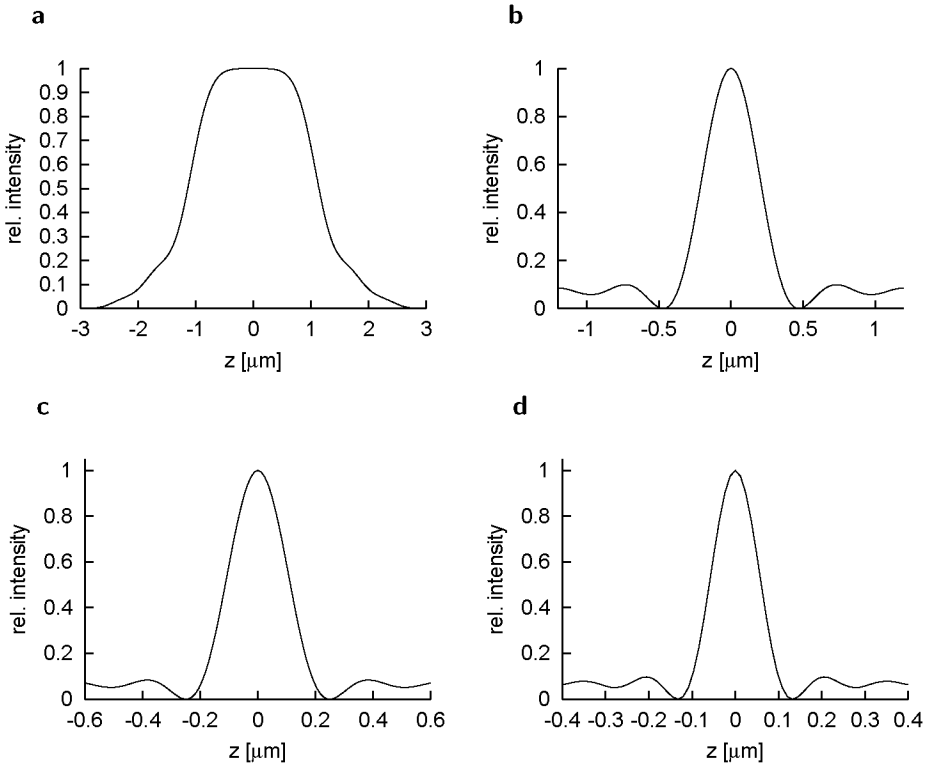

Figure 6.10: Calculated axial responses to a thin slice of 2 μm diameter oriented parallel to the k_x-k_y-plane. Graphs (**a**) to (**d**) refer to cases (a) to (d) of Tab. 6.1. Attention should be paid to the different scalings on the abscissae.

Chapter 7

Conclusion

This thesis concentrates on resolution enhancement in far-field fluorescence microscopy by illuminating the specimen with structured light. A method, called "harmonic excitation light microscopy" (HELM), has been introduced and realized which employs space-harmonic intensity patterns generated by interference of laser beams to more than double the resolution.

The first part of the thesis is a theoretical study of the electrical field distribution in the object plane and of the influence of the light pattern on the image formation. Frequency domain analysis shows that additional information not accessible in conventional microscopy can be extracted. For that purpose, images for different translatory shifts of the pattern must be acquired and postprocessed electronically.

In a next step, a setup was planed and realized. The main component is the interference generating apparatus which produces a two-dimensional mesh-like interference pattern in the object plane. Using a mesh-like pattern allows one to enhance the resolution in two dimensions without mechanical actuators to rotate the pattern. A critical design issue was the stability of the pattern for the relatively long

acquisition time. Sufficient stability could be achieved by a compact design reducing thermal drift and by using electrostrictive actuators. Since the interference generating apparatus illuminates the specimen from the backside through the slide, no modifications in the imaging path were required. For this reason, the setup is not restricted to any particular type of microscope.

The implementation of an image reconstruction algorithm showed two main difficulties: The optical transfer function calculated by paraxial theory turned out to be too inaccurate and the orientation of the interference pattern had to be determined with sub-pixel precision. These hurdles could be mastered by carefully measuring the transfer function under comparable optical conditions and by acquiring additional brightfield images with the fluorescence filter removed from the imaging path.

The HELM-method was tested with artificial as well as biological samples. To verify the resolution enhancement, the same area of a sample of fluorescent beads was imaged with HELM and, additionally, with an atomic force microscope for reference. Images of microtubules and of various histological samples showed that the resolution enhancement can also be achieved with objects of practical interest. Compared to the widely used confocal microscope, an even better resolution was achieved. Furthermore, HELM has no photon efficiency reducing pinhole and is not subject to fundamental imaging speed limitations imposed by the small illumination spot size in confocal microscopy.

A further topic of the thesis is the extension of the method to three-dimensional imaging. A modified setup is proposed which allows one to generate space harmonic interference patterns with any desired orientation in three-dimensional space. The complexity of the proposed setup is comparable with that one of confocal devices. The achievable resolution gain of this device was analyzed by numeric simulations. It provides an almost isotropic resolution in the 100 nm range without the need for a lateral scanning mechanism. These properties are not

achieved by any other method.

The next step would be the realization of a three-dimensional HELM setup and the implementation of the appropriate image reconstruction algorithm. Possible complications in three-dimensional HELM are an increased mechanical drift due to the long image acquisition time and computational limitations caused by the high volume of data. It is expected, however, that these issues can be solved by employing smart algorithms and, probably, experimental add-ons to calibrate the object and/or pattern position. Then, three-dimensional HELM would provide an unrivaled resolution combined with high photon efficiency and high speed imaging capability.

Appendix A

Optical trapping in interference fields

This thesis is part of the NANO-II project at the "Eidgenössische Technische Hochschule Zürich" where NANO stands for "Non-contact Assembly of Nano-Objects and Non-contact Analysis of Nano-Objects". The goal of the project is to study methods for visualizing and manipulating objects in the sub-micrometer range. The HELM setup described in this thesis produces interference patterns which are expected to be applicable to optical trapping as well. Therefore, it was obvious to also consider the manipulation aspect. In this appendix, first results for optical trapping with HELM-like interference patterns are presented.

Generally, non-contact methods for particle handling are very favorable since problems with adhesive forces between object and manipulating tool are avoided. One important class of such non-contact methods are optical traps. Here, forces exerted on particles by intense light are employed to control their motion. The most common setup used for optical trapping works with strongly focused laser beams.

Under suitable conditions, the laser focus forms a potential well for dielectric [4, 11, 34] as well as metallic [81] particles even for moderate laser powers. Manipulation of a few particles is possible by time-multiplexed illumination [61] or by using holographic methods [67].

In practice, parallel handling of a large number of objects is often essential. Parallel manipulation can be achieved by optical traps which make use of interference patterns. Basically, particles are trapped within the bright zones of such patterns as a result of the dominant gradient force [15, 84, 17]. Suspended particles form a regular array which is denoted as optical crystal or optical matter.

Till today, however, interference traps have been realized for relatively large (a few micrometer) objects only. To meet the requirements of the NANO-II project, the particle sizes must be reduced to noticeably less than one micrometer. Potential applications of such optical traps lie in the field of writing diffractive structures [27] or photonic crystals, non-contact particle transport and controlling the crystallization of macromolecules for structural investigations by electron microscopy.

The connection to HELM lies in the fact that the interference patterns used for harmonic excitation are expected to be capable of trapping very small particles as well. Unfortunately, the intensity of the interference field in the presented HELM system turned out to be too small to achieve sufficient trapping forces. Therefore, a similar setup was built within two semester theses [32, 62] which allows one to focus the laser beams to a greater extent. Using a 100 mW Ar-ion laser, 100-nm polystyrene beads could still escape from the potential wells. However, an increased probability of presence in the bright zones could be observed and, together with theoretical predictions, this observation gives rise to the assumption that a complete trapping could be achieved by using a stronger laser source.[1]

[1] A transport of slightly larger beads (200 nm diameter) could be recently demonstrated by D. Häfliger in a one beam TIR setup.

A.1 Physical background

In this section, the basic forces exerted on particles in electromagnetic fields will be discussed. To simplify the mathematical description and to be consistent with literature, the Gaussian system of units is used [45, appendix].

The size of particles of interest (100 nm or less) is well below the wavelength of the employed light. Therefore, the particles basically act as Rayleigh scatterers. As a result of an external electric field, a Rayleigh scatterer is polarized and radiates according to the well known dipole characteristic [45]. A Rayleigh scatterer exposed to a time harmonic electromagnetic field experiences two forces, the scattering force F_{scat} and the gradient force F_{grad}. For spherical particles, the scattering force is given by

$$\mathbf{F}_{\text{scat}} = \frac{128\,\pi^5 n_m}{3\,c\lambda^4}\left(\frac{m^2-1}{m^2+2}\right)^2 R^6\,\mathbf{S}, \tag{A.1}$$

where n_m is the refractive index of the embedding medium, m is the ratio of refractive indices of particle and medium, λ is the vacuum wavelength, R is the radius of the sphere and $\mathbf{S}$ is the time averaged energy flux [84]. The gradient force is given by

$$\mathbf{F}_{\text{grad}} = \overbrace{\frac{n_m^3}{2}\left(\frac{m^2-1}{m^2+2}\right)}^{=:C_m} R^3\,\nabla(|\mathbf{E}|^2), \tag{A.2}$$

where $\mathbf{E}$ is the complex electric field strength [84].

For the two-beam interference setup studied, the gradient force is expected to be the dominant one since the lateral energy flux of the field distribution vanishes due to the lateral symmetry.[2]

[2]There is, however, a small axial force component. This axial force becomes almost zero for the more relevant setup described in section A.2.

Since the gradient force is a conservative one,[3] a potential can be defined. For a spherical particle, this potential can be calculated by integrating Eq. A.2:

$$W(\mathbf{r}) = \int_{\infty}^{\mathbf{r}} -\mathbf{F}_{\text{grad}}(\mathbf{r})\, d\mathbf{r} = -c_m\, R^3\, |\mathbf{E}(\mathbf{r})|^2, \tag{A.3}$$

where the potential energy is set to zero at infinity (i.e. $W(\infty) = 0$).

Eq. A.3 allows one to calculate the depth of the potential well induced by the HELM interference field on small spherical particles. To this end, the electric field strength in the bright zones of the illumination pattern has to be calculated first. The modulus of the energy flux $\mathbf{S}$ of a plane electromagnetic wave is given by

$$|\mathbf{S}| = \frac{c\, n_m}{8\pi} |\mathbf{E}|^2, \tag{A.4}$$

where c is the velocity of light and n_m is the refractive index of the medium (1.33 for water immersed particles) [45, chapter 7]. In HELM, four laser beams of 25 mW each are focused to a beam diameter of approx. 140 μm (see Fig. 4.3). Therefore, the amplitudes of the incident beams (E_1 and E_2 in Eq. 3.20 and 3.22, respectively) can be calculated by using Eq. A.4 as

$$E_1 = E_2 = \sqrt{\frac{8\pi|\mathbf{S}|}{c\, n_m}} = 1.01 \sqrt{\frac{\text{ERG}}{\text{cm}^3}}, \tag{A.5}$$

where the Gaussian energy unit ERG is used (1 ERG = 10^{-7} J) [45, appendix]. The electric field amplitude E_{res} of the interference pattern generated by the two y-polarized beams is according to Eq. 3.28

$$E_{\text{res}} = 2E_1 \cos\left(k_x x + \frac{\Delta}{2}\right), \tag{A.6}$$

[3] The curl of the gradient force field is zero due to $\nabla \times (\nabla F) = 0$. Therefore, the definition of a potential is unambiguous except for an additive constant.

where the partial reflection at the cover slip is neglected (i.e. $R = 0$). In the antinodal zones, E_{res} equals $2E_1$. Since the same is true for the x-polarized field, the maximum field amplitude E_{max} of the *two-dimensional* pattern becomes

$$E_{\mathrm{max}} = \sqrt{2} \times 2E_1 = 2.86 \sqrt{\frac{\mathrm{ERG}}{\mathrm{cm}^3}}, \tag{A.7}$$

where the factor $\sqrt{2}$ results from the orthogonality of the x- and y-polarized field components.

Now, the potential well depth W_0 can be calculated by applying Eq. A.3 with the appropriate material constant c_m. For water immersed polystyrene beads ($n_m = 1.33$, refractive index of polystyrene = 1.59 [48]), c_m is 0.147. Inserting Eq. A.7 and the value of c_m into Eq. A.3 a potential well depth of

$$W_0 = 1.5 \times 10^{-16}\mathrm{ERG} = 1.5 \times 10^{-23}\mathrm{J} \tag{A.8}$$

is obtained for 100 nm diameter beads. At room temperature, the average kinetic energy is of the order of $kT = 4 \times 10^{-21}$ J and, hence, two to three orders of magnitude larger than W_0 (k is the Boltzmann constant and T is the temperature in Kelvin). According to these calculations, the HELM setup is not expected to trap particles. This prediction is in complete agreement with the observations. For this reason, a different setup was built which enables one to achieve a strongly increased intensity.

A.2 The setup for optical trapping

The optical trap setup (Fig. A.1) is similar to the HELM setup. However, a few significant differences exist. As the most obvious difference, the trapping setup provides only a one-dimensional (fringe-like) interference pattern to reduce complexity and costs.

A key difference is the reduced diameter of the illuminating spot. In the trapping setup, lenses with a focal length of 18.4 mm are placed

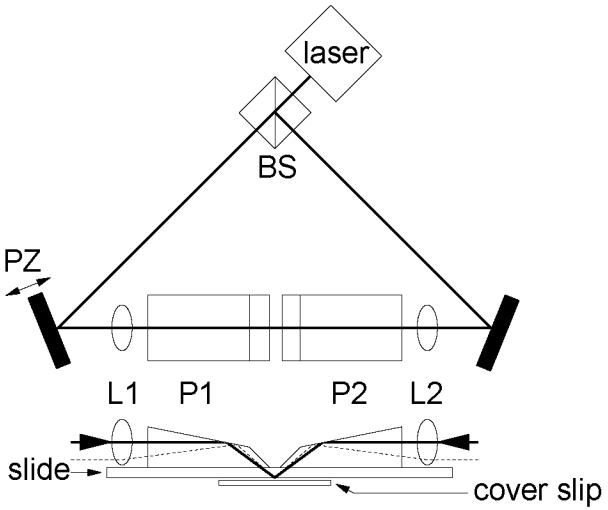

Figure A.1: Setup used for optical trapping experiments. A collimated laser beam is split by beam splitters BS into two beams of equal intensity. Two lenses L1 and L2 (focal length 18.4 mm in air) and two glass prisms P1 and P2 form a focal spot in the water layer between slide and cover slip. A vertical translation of the beams (illustrated by the dashed line) changes the angle of incidence by maximum $\pm 2.5^\circ$ without affecting the position of the focal spot. An inverted microscope (not shown) serves for observing.

in direct proximity of the prisms resulting in a theoretical beam waist diameter of 7.6 μm for the used laser source (Eq. 4.1, primary beam waist diameter $w_0 = 1.5$ mm).

The measured value is roughly 10 μm; the difference can be explained by aberrations and by measurement errors [62]. In relation to HELM, the reduced spot size leads to an intensity increase by a factor of 200.

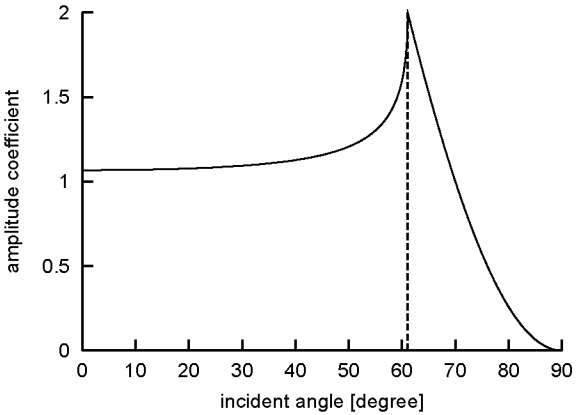

Figure A.2: Amplitude coefficient of the transmitted beam for a glass-water transition. Shown is the ratio of the electric field amplitude in the water layer in direct proximity to the interface relative to the incident one. The dashed line indicates the critical angle for TIR (61°).

Furthermore, the criterions for choosing the angle of incidence α_i are quite different for optical trapping than for HELM. The reasons for choosing α_i smaller than the critical angle for TIR (see subsection 5.1.1) do not apply to trapping experiments. Trapping is possible with propagating waves [15] as well as with evanescent ones [48]. Since the achievable electrical field strength is of major importance, the amplitude coefficient of the transmitted beam relative to the incident one (*Fresnel* formulae, [12]) should be taken into account. Fig. A.2 illustrates that working near the critical angle is favorable as this enhances the electric field strength by a factor of two resulting in a four times increased intensity. The fringe spacing for these angles of incidence is approx. 184 nm.

As in the HELM setup, a piezo actuator is provided to shift the

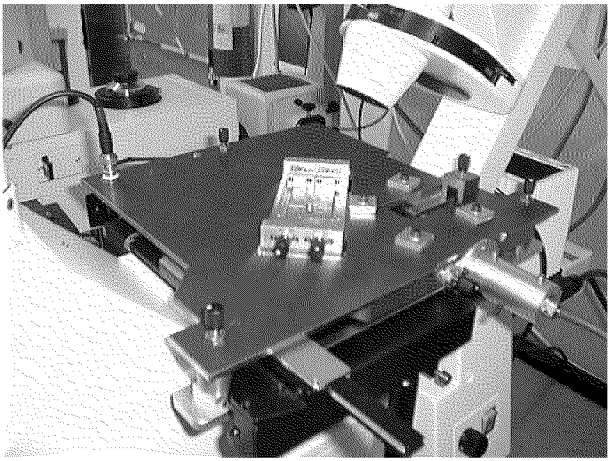

Figure A.3: Photography of the trapping setup mounted on an inverted ZEISS microscope. The two visible adjustment knobs serve for aligning the illumination spots relative to each other.

interference fringes relative to the immersion medium. By applying a sawtooth voltage to the actuator, an effective particle transport perpendicular to the fringes is expected to be achievable. Fig. A.3 and Fig. A.4 show photographs of the trapping setup.

Due to the reduced spot size and the amplitude amplification at the glass-water interface, the intensity is enhanced by a factor of approx. 800 in relation to the HELM setup. By re-performing the calculations leading to Eq. A.3, one obtains an expected potential well depth of 1.2×10^{-20} J which is slightly above the average kinetic energy (4×10^{-21} J). Though the estimated potential well depth of approx. $3kT$ may not be sufficient for a complete (i.e. long term) trapping, the setup described makes sense for two reasons: First, an increased probability of presence for particles within the bright zones should be observable. Such an observation would validate the theoretical calcu-

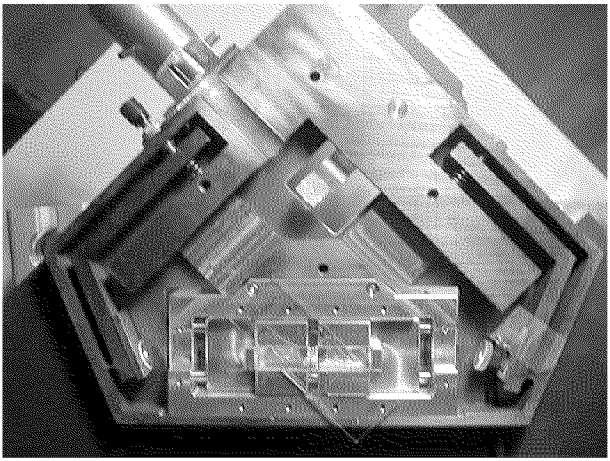

Figure A.4: Bottom view of the trapping setup with removed base plate. Visible are the optical components (prisms, mirrors and the beam splitter) and two flexible joints for aligning the optical paths.

lations. Secondly, a complete trapping is expected to be achievable by employing a stronger laser power and/or increasing the viscosity of the embedding medium to reduce thermal motion.

A.3 Results

To test the trapping behavior of the setup fluorescent polystyrene beads with a diameter of 100 nm were used. The beam's angle to the optical axis α_i was set to slightly below the critical angle for TIR. As expected, the beads were not completely trapped, i.e. they could escape from one fringe and cross over to another one. Therefore, a statistical method was needed to find out whether the probability of presence was nonuniform.

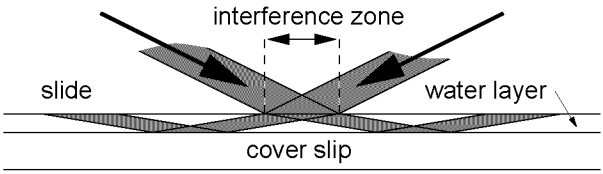

Figure A.5: Geometry of the interference zone in the optical trap setup. In contrast to the HELM setup, the interference zone is at the slide-water interface. Due to the small spot size and the flat angle of the beams in the water layer, the reflected beams do not interfere with the incident ones even for a very thin water layer of a few micrometer.

A statistical analysis is possible by measuring the scattered light intensity with a CCD-camera and relating it to the scattered intensity *without* interference.[4] For this analysis, the total light intensity on the CCD-chip for an ensemble of scatterers is assumed to be the sum of the intensities of the individual ones. The intensity of the scattered wave of one individual Rayleigh particle is proportional to $|\mathbf{E}|^2$ at the particle position [45, chapter 25]. Therefore, the total light intensity on the CCD-chip $I_\int$ can be calculated by

$$I_\int = C \int\limits_{\text{field of view}} \rho(\mathbf{r})|\mathbf{E}(\mathbf{r})|^2,\ d\mathbf{r} \tag{A.9}$$

where ρ is the density of the scatterers in the object plane and where C is a constant. Now, the field distribution of the interference field (Eq. 3.28) has to be rewritten in a somewhat different form. Since the beam reflected at the glass-water transition does not interfere with the incident beam (i.e. $R = 0$, see Fig. A.5), Eq. 3.28 becomes

$$E_{\text{res}} = 2E_1 e^{-ik_z z}\cos(k_x x) + (E_2 - E_1)e^{ik_x x}e^{-ik_z z}, \tag{A.10}$$

[4]The fluorescence light turned out to be useless for quantitative measurements due to the rapid photo-bleaching.

where the phase shift Δ is set to zero without affecting the general applicability. Taking the modulus of Eq. A.10 one obtains

$$|E_{\mathrm{res}}|^2 = E_1^2 + E_2^2 + 2E_1E_2\cos(2k_x x), \tag{A.11}$$

where the identities $\sin^2(x) = \frac{1}{2}(1 - \cos(2x))$ and $\cos^2(x) = \frac{1}{2}(1 + \cos(2x))$ are used. With N the number of scatterers in the field of view, one obtains by inserting Eq. A.11 into Eq. A.9

$$I_{\int} = CN\left((E_1^2 + E_2^2) + 2E_1E_2\overbrace{\int\limits_{\text{field of view}} \frac{\rho(\mathbf{r})}{N}\cos(2k_x x)\,d\mathbf{r}}^{=:K}\right), \tag{A.12}$$

where K describes the correlation between particle distribution and interference pattern. For the same sample of immersed beads, three images were acquired with total intensities I_1, I_2 and I_i, respectively. For the first image the second beam was blocked (i.e. $E_2 = 0$), for the second image the first beam was blocked (i.e. $E_1 = 0$) and for the last image both beams could interfere. According to Eq. A.12, the total intensities are

$$I_1 = CNE_1^2, \tag{A.13}$$

$$I_2 = CNE_2^2 \quad \text{and} \tag{A.14}$$

$$I_i = CN(E_1^2 + E_2^2) + 2CE_1E_2K. \tag{A.15}$$

For the ratio $I_i/(I_1 + I_2)$ one obtains

$$\frac{I_i}{I_1 + I_2} = \frac{E_1^2 + E_2^2 + 2E_1E_2K}{E_1^2 + E_2^2} = 1 + K, \tag{A.16}$$

where it is assumed that E_1 approximately equals E_2. By evaluating the intensity ratio Eq. A.16, the correlation K between particle distribution and interference pattern can be calculated from the measured total intensities. For 100 nm diameter beads immersed in a mixture

of 50% glycerin an 50% water, a correlation $K = 0.15$ was found. To validate the method, a sample of beads fixed to the cover slip was prepared; here the particle distribution is certainly independent of the interference pattern. As expected, the measured value for K was near to zero (0.02). Furthermore, a correlation of 0.15 for mobile particles, corresponding to a slightly increased probability of presence in the bright zones, is in agreement with the estimated potential well depth of approx. $3kT$.[5]

Fortunately, the setup is constructed to function with the common 1064 nm wavelength of *Nd*-YAG lasers as well. By using a 5 W laser of this type which is available in the laboratory, the potential well depth would be increased by a factor of $\frac{5\text{ W}}{100\text{ mw}}\frac{1}{2} = 25$.[6] Therefore, the potential well depth would be of the order of 80 kT which is expected to be sufficient for complete trapping.

[5]The estimation of $3kT$ is based on infinitesimal small particles and lossless optical paths. Therefore, the value should be interpreted carefully as "of the order of kT".

[6]The factor $\frac{1}{2}$ is a result of the fact that the gradients in an interference field are inversely proportional to the wavelength of the employed light.

Bibliography

[1] D. A. Agard, Y. Hiraoka, and J. W. Sedat. Three-dimensional microscopy: image processing for high resolution subcellular imaging. *Proceedings of the SPIE*, 1161:24–30, 1989.

[2] D. A. Agard, Y. Hiraoka, P. Shaw, and J. W. Sedat. Fluorescence microscopy in three dimensions. In D. L. Taylor, editor, *Fluorescence Microscopy of Living Cells in Culture Part B. Quantitative Fluorescence Microscopy—Imaging and Spectroscopy*, volume 30 of *Methods in Cell Biology*. Academic Press, 1989.

[3] B. Alberts, D. Bray, J. Lewis, M. Raff, K. Roberts, and J. D. Watson. *Molecular Biology of the Cell*. Garland Publishing, third edition, 1994.

[4] A. Ashkin, J. M. Dziedzic, J. E. Bjorkholm, and S. Chu. Observation of single-beam gradient force optical trap for dielectric particles. *Optics Letters*, 11(5):288–290, 1994.

[5] D. Axelrod and E. H. Hellen. Emission of fluorescence at an interface. In D. L. Taylor, editor, *Fluorescence Microscopy of Living Cells in Culture Part B. Quantitative Fluorescence Microscopy—Imaging and Spectroscopy*, volume 30 of *Methods in Cell Biology*. Academic Press, 1989.

[6] B. Bailey, D. L. Farkas, D. L. Taylor, and F. Lanni. Enhancement of axial resolution in fluorescence microscopy by standing-wave excitation. *Nature*, 366:44–48, 1993.

[7] P. L. Becker. Quantitative fluorescence measurements. In X. F. Wang and B. Herman, editors, *Fluorescence Imaging Spectroscopy and Microscopy*, volume 137 of *Chemical Analysis*. Wiley, 1996.

[8] M. Bertero and P. Boccaci. Linear inverse problems in confocal light microscopy. In C. Bourrely, P. Chiapetta, and B. Torresani, editors, *Electromagnetic and Acoustic Scattering: Detection and Inverse Problems*. World Scientific, 1988.

[9] G. Binnig and C. F. Quate. Atomic force microscope. *Physical Review Letters*, 56(9):930–933, 1986.

[10] G. Binnig, H. Rohrer, C. Gerber, and E. Weibel. Surface studies by scanning tunneling microscopy. *Physical Review Letters*, 49(1):57–61, 1982.

[11] S. M. Block. Making light work with optical tweezers. *Nature*, 360:493–495, 1992.

[12] M. Born and E. Wolf. *Principles of Optics*. Pergamon Press, sixth edition, 1980.

[13] G. J. Brakenhoff, P. Blom, and P. Barends. Confocal scanning light microscopy with high aperture immersion lenses. *Journal of Microscopy*, 117(2):219–232, 1979.

[14] G. J. Brakenhoff, E. A. van Spronsen, H. T. M. van der Voort, and N. Nanninga. Three-dimensional confocal fluorescence microscopy. In D. L. Taylor, editor, *Fluorescence Microscopy of Living Cells in Culture Part B. Quantitative Fluorescence Microscopy—Imaging and Spectroscopy*, volume 30 of *Methods in Cell Biology*. Academic Press, 1989.

[15] M. M. Burns, J.-M. Fournier, and J. A. Golovchenko. Optical matter: Crystallization and binding in intense optical fields. *Science*, 249:749–754, 1990.

[16] M. Chalfie, Y. Tu, G. Euskirchen, and W. W. Ward. Green fluorescent protein as a marker for gene expression. *Science*, 263(5148):802–805, 1994.

[17] A. E. Chiou, W. Wang, G. J. Sonek, J. Hong, and M. W. Berns. Interferometric optical tweezers. *Optics Communications*, 133:7–10, 1997.

[18] J.-A. Conchello. Superresolution and point spread function sensitivity analysis of the expectation-maximization algorithm for computational optical sectioning microscopy. *Proceedings of the SPIE*, 2302:369–378, 1994.

[19] J.-A. Conchello. Superresolution and convergence properties of the expectation-maximization algorithm for maximum-likelihood deconvolution of incoherent images. *Journal of the Optical Society of America A*, 15:2609–2618, 1998.

[20] G. E. Cragg and P. T. C. So. Lateral resolution enhancement with standing evanescent waves. *Optics Letters*, 25(1):46–48, 2000.

[21] G. Danuser and E. Mazza. Observing deformations of 20 nanometer with a low numerical aperture microscope. *Proceedings of the SPIE*, 2782:180–191, 1996.

[22] W. Denk, J. H. Strickler, and W. W. Webb. Two-photon laser scanning fluorescence microscope. *Science*, 248(4951):73–76, 1990.

[23] V. Drazic. Three-dimensional transfer function analysis of a confocal fluorescence microscope with a finite-sized source and detector. *Journal of Modern Optics*, 40(5):879–887, 1993.

[24] A. Erhardt, G. Zinser, D. Komitowski, and J. Bille. Reconstructing 3-D light-microscopic images by digital image processing. *Applied Optics*, 24(2):194–200, 1985.

[25] Y.-S. Fan, L. M. Davis, and T. B. Shows. Mapping small DNA sequences by fluorescence in situ hybridization directly on banded metaphase chromosomes. *Proceedings of the National Academy of Sciences USA*, 87:6223–6227, 1990.

[26] T. Fliessbach. *Elektrodynamik*. Spektrum Akademischer Verlag, second edition, 1997.

[27] J.-M. R. Fournier, M. M. Burns, and J. A. Golovchenko. Writing diffractive structures by optical trapping. *Proceedings of the SPIE*, 2406:101–111, 1995.

[28] R. Freimann, S. Pentz, and H. Hörler. Development of a standing-wave fluorescence microscope with high nodal plane flatness. *Journal of Microscopy*, 187(3):193–200, 1997.

[29] B. R. Frieden. Optical transfer of the three-dimensional object. *Journal of the Optical Society of America*, 57(1):56–66, 1967.

[30] J. T. Frohn, H. F. Knapp, and A. Stemmer. True optical resolution beyond the Rayleigh limit achieved by standing wave illumination. *Proceedings of the National Academy of Sciences USA*, 97(13):7232–7236, 2000.

[31] J. T. Frohn and A. Stemmer. Resolution enhancement for fluorescence microscopy by standing-wave illumination. *EOS Topical Meetings Digest Series*, 25:58–59, 2000.

[32] F. Füglistaler. Optical matter. Semesterarbeit, Eidgenössische Technische Hochschule, Zürich, 1999.

[33] J. W. Goodman. *Introduction to Fourier Optics*. McGraw-Hill, second edition, 1996.

[34] K. O. Greulich. *Micromanipulation by Light in Biology and Medicine.* Birkhäuser Verlag, Basel, 1999.

[35] M. G. L. Gustafsson. Surpassing the lateral resolution limit by a factor of two using structured illumination microscopy. *Journal of Microscopy*, 198(2):82–87, 2000.

[36] M. G. L. Gustafsson, D. A. Agard, and J. W. Sedat. Sevenfold improvement of axial resolution in 3D widefield microscopy using two objective lenses. *Proceedings of the SPIE*, 2412:147–156, 1995.

[37] M. G. L. Gustafsson, D. A. Agard, and J. W. Sedat. 3D widefield microscopy with with two objective lenses: experimental verification of enhanced axial resolution. *Proceedings of the SPIE*, 2655:62–66, 1996.

[38] M. G. L. Gustafsson, D. A. Agard, and J. W. Sedat. I^5M: 3D widefield light microscopy with better than 100 nm axial resolution. *Journal of Microscopy*, 195(1):10–16, 1999.

[39] S. Hell and E. H. K. Stelzer. Properties of a 4π confocal fluorescence microscope. *Journal of the Optical Society of America A*, 9:2159–2166, 1992.

[40] S. W. Hell, M. Schrader, and H. T. M. van der Voort. Far-field fluorescence microscopy with three-dimensional resolution in the 100 nm range. *Journal of Microscopy*, 187(2):1–7, 1997.

[41] P. D. Higdon, P. Török, and T. Wilson. Imaging properties of high aperture multiphoton fluorescence scanning optical microscopes. *Journal of Microscopy*, 193(2):127–141, 1999.

[42] Y. Hiraoka, J. W. Sedat, and D. A. Agard. Determination of three-dimensional imaging properties of a light microscope system: Partial confocal behavior in epifluorescence microscopy. *Biophysical Journal*, 57:325–333, 1990.

[43] S. Inoué. Imaging of unresolved objects, superresolution, and precision of distance measurement with video microscopy. In D. L. Taylor, editor, *Fluorescence Microscopy of Living Cells in Culture Part B. Quantitative Fluorescence Microscopy—Imaging and Spectroscopy*, volume 30 of *Methods in Cell Biology*. Academic Press, 1989.

[44] S. Inoué and K. R. Spring. *Video Microscopy: The Fundamentals*. Plenum Press, 1997.

[45] J. D. Jackson. *Classical Electrodynamics*. Wiley, second edition, 1975.

[46] H. O. Jacobs, H. F. Knapp, S. Müller, and A. Stemmer. Surface potential mapping: A qualitative material contrast in SPM. *Ultramicroscopy*, 69:39–49, 1997.

[47] R. Juškaitis, T. Wilson, M. A. A. Neil, and M. Kozubek. Efficient real-time confocal microscopy with white light soureces. *Nature*, 383:804–806, 1996.

[48] S. Kawata and T. Sugiura. Movement of micrometer-sized particles in the evanescent field of a laser beam. *Optics Letters*, 17(11):772–774, 1992.

[49] S. Kimura and C. Munakata. Dependence of 3-D optical transfer functions on the pinhole radius in fluorescent confocal optical microscope. *Applied Optics*, 29(20):3007–3011, 1990.

[50] T. A. Klar and S. W. Hell. Subdiffraction resolution in far-field fluorescence microscopy. *Optics Letters*, 24(14):954–956, 1999.

[51] N. S. Kontoyannis and F. Lanni. Measured and computed point spread functions for an indirect water immersion objective in three-dimensional fluorescence microscopy. *Proceedings of the SPIE*, 2655:34–42, 1996.

[52] V. Krishnamurthi, B. Bailey, and F. Lanni. Image processing in 3-D standing-wave fluorescence microscopy. *Proceedings of the SPIE*, 2655:18–25, 1996.

[53] V. Krishnamurthi, Y.-H. Liu, T. J. Holmes, B. Roysam, and J. N. Turner. Blind deconvolution of 2D and 3D fluorescent micrographs. *Proceedings of the SPIE*, 1660:95–102, 1992.

[54] F. Lanni, B. Bailey, D. L. Farkas, and D. L. Taylor. Excitation field synthesis as a means for obtaining enhanced axial resolution in fluorescence microscopes. *Bioimaging*, 1:187–196, 1993.

[55] F. Lanni and G. J. Baxter. Sampling theorem for square-pixel image data. *Proceedings of the SPIE*, 1660:140–147, 1992.

[56] W. Lukosz. Optical systems with resolving powers exceeding the classical limit. *Journal of the Optical Society of America*, 56(11):1463–1472, 1966.

[57] W. Lukosz and M. Marchand. Optische Abbildung unter Überschreitung der beugungsbedingten Auflösungsgrenze. *Optica Acta*, 10:241–255, 1963.

[58] K. W. McIntyre, J. F. Bukowski, and R. M. Welsh. Exquisite specifity of adoptive immunization in arenavirus-infected mice. *Antiviral Research*, 5(5):299–305, 1985.

[59] G. Meyer and N. M. Amer. Simultaneous measurement of lateral and normal forces with an optical-beam-deflection atomic force microscope. *Applied Physics Letters*, 57(20):2089–2091, 1990.

[60] M. Minsky. Memoir on inventing the confocal scanning microscope. *Scanning*, 10:128–138, 1988.

[61] C. Mio, T. Gong, A. Terray, and D. W. M. Marr. Design of a scanning laser optical trap for multiparticle manipulation. *Review of Scientific Instruments*, 71(5):2196–2200, 2000.

[62] M. Münchinger. Transportieren mit dem Lichtförderband. Semesterarbeit, Eidgenössische Technische Hochschule, Zürich, 2000.

[63] H. Naumann and G. Schröder. *Bauelemente der Optik.* Carl Hauser Verlag, München, sixth edition, 1992.

[64] M. A. A. Neil, R. Juškaitis, and T. Wilson. Method of obtaining optical sectioning by using structured light in a conventional microscope. *Optics Letters*, 22(24):1905–1907, 1997.

[65] M. A. A. Neil, R. Juškaitis, and T. Wilson. Real time 3D fluorescence microscopy by two beam interference illumination. *Optics Communications*, 153:1–4, 1998.

[66] D. W. Pohl, W. Denk, and M. Lanz. Optical stethoscopy: Image recording with $\lambda/20$. *Applied Physics Letters*, 44(7):651–653, 1984.

[67] M. Reicherter, T. Haist, E. U. Wagemann, and H. J. Tiziani. Optical particle trapping with computer-generated holograms written on liquid-crystal display. *Optics Letters*, 24(9):608–610, 1999.

[68] B. E. A. Saleh and M. C. Teich. *Fundamentals of Photonics.* Wiley, 1991.

[69] D. R. Sandison, D. W. Piston, R. M. Williams, and W. W. Webb. Quantitative comparison of background rejection, signal-to-noise ratio, and resolution in confocal and full-field laser scanning microscopes. *Applied Optics*, 34(19):3576–3588, 1985.

[70] D. R. Sandison, R. M. Williams, K. S. Wells, J. Strickler, and W. W. Webb. Quantitative fluorescence confocal laser scanning microscopy (CSLM). In J. B. Pawley, editor, *Handbook of Biological Confocal Microscopy.* Plenum Press, second edition, 1995.

[71] S. G. Schulman. *Fluorescence and Phosphorescence Spectroscopy: Physicochemical Principles and Practice*, volume 59 of *Analytical Chemistry*. Pergamon Press, 1977.

[72] L. Seveus, M. Väisälä, S. Syrjänen, M. Sandberg, A. Kuusisto, R. Harju, J. Salo, I. Hemmilä, H. Kojola, and E. Soini. Time-resolved fluorescence imaging of europium chelate label in immunohistochemistry and in situ hybridization. *Cytometry*, 13(4):329–338, 1992.

[73] A. Sharma and S. G. Schulman. *Introduction to Fluorescence Spectroscopy*. Wiley, 1999.

[74] Z. Shen and H. H. Lipowski. Image enhancement of the in vivo leukocyte-endothelium contact zone using optical sectioning microscopy. *Annals of Biomedical Engineering*, 25:521–535, 1997.

[75] C. J. R. Sheppard and A. Choudhury. Image formation in the scanning microscope. *Optica Acta*, 24(10):1051–1073, 1977.

[76] R. Sonnenfeld and P. K. Hansma. Atomic resolution microscopy in water. *Science*, 232(4747):211–213, 1986.

[77] J. J. Stamnes. *Waves in Focal Regions*. Adam Hilger, 1986.

[78] E. H. K. Stelzer. Contrast, resolution, pixelation, dynamic range and signal-to-noise ratio: Fundamental limits to resolution in fluorescence microscopy. *Journal of Microscopy*, 189:15–24, 1997.

[79] A. Stemmer. A hybrid scanning force and light microscope for surface imaging and three-dimensional optical sectioning in differential interference contrast. *Journal of Microscopy*, 178(1):28–36, 1995.

[80] A. Stemmer, R. Reichelt, R. Wyss, and A. Engel. Biological structures imaged in a hybrid scanning transmission electron microscope and scanning tunneling microscope. *Ultramicroscopy*, 35:255–264, 1991.

[81] K. Svoboda and S. M. Block. Optical trapping of metallic Rayleigh particles. *Optics Letters*, 19(13):930–932, 1994.

[82] D. L. Taylor, M. Nederlof, F. Lanni, and A. S. Waggoner. The new vision of light microscopy. *American Scientist*, 80:322–335, 1992.

[83] L. R. van den Doel, A. D. Klein, S. L. Ellenberger, H. Netten, F. R. Boddeke, L. J. van Vliet, and I. T. Young. Quantitative evaluation of light microscopes based on image processing techniques. *Bioimaging*, 6:138–149, 1998.

[84] K. Visscher and G. J. Brakenhoff. Theoretical study of optically induced forces on spherical particles in a single beam trap I: Rayleigh scatterers. *Optik*, 89(4):174–180, 1992.

[85] T. Wilson. The role of the pinhole in confocal imaging systems. In J. B. Pawley, editor, *Handbook of Biological Confocal Microscopy*. Plenum Press, second edition, 1995.

[86] T. Wilson, R. Juškaitis, M. A. A. Neil, and M. Kozubek. Confocal microscopy by aperture correlation. *Optics Letters*, 21(23):1879–1881, 1996.

[87] R. Windecker and H. J. Tiziani. Semispatial, robust, and accurate phase evaluation algorithm. *Applied Optics*, 34(31):7321–7326, 1995.

[88] R. Windecker and H. J. Tiziani. Topometry of technical and biological objects by fringe projection. *Applied Optics*, 34(19):3644–3650, 1995.

Curriculum Vitae

Personal data:

Name:	Jan Tillman Frohn
Date of birth:	28nd of February, 1971
Place of origin:	Bonn, Germany
Nationality:	German

Education:

1977-1981	Primary school, Bonn, Germany
1981-1990	Secondary school (Gymnasium), Bonn, Germany Degree: Abitur
1990-1992	University of Bonn, Germany Degree: Intermediate diploma in physics
1992-1996	University of Freiburg, Germany Diploma thesis on selective emitters for thermophotovoltaic energy conversion Degree: Diploma in physics
1997-2000	Nanotechnology Group, Institute of Robotics, Swiss Federal Institute of Technology (ETH) Ph.D. research and supervision of student projects in the field of nano science Thesis advisors: Prof. A. Stemmer (ETH Zurich) and Prof. H. J. Tiziani (University of Stuttgart)

Collateral engagement:

1989-1992	Development of power and analog electronics for telescopic camera cranes
1992-1997	Development of electronics and software for second generation telescopic camera cranes